Developments in the Method of Finite Spheres: Efficiency and Coupling to the Traditional Finite Element Method

by

Jung-Wuk Hong

B.S., Civil Engineering (1994)
Yonsei University

S.M., Civil Engineering (1996)
Korea Advanced Institute of Science and Technology

Submitted to the Department of Civil and Environmental Engineering
in partial fulfillment of the requirements for the degree of
Doctor of Philosophy
at the
MASSACHUSETTS INSTITUTE OF TECHNOLOGY
February 2004

Author .....
Department of Civil and Environmental Engineering
September 15, 2003

Certified by ..
Klaus-Jürgen Bathe
Professor of Mechanical Engineering
Thesis Supervisor

Certified by .....
Franz-Josef Ulm
Associate Professor of Civil and Environmental Engineering
Chairman, Thesis Committee

Accepted by .....
Heidi Nepf
Chairman, Department Committee on Graduate Studies

Developments in the Method of Finite Spheres: Efficiency and Coupling to the Traditional Finite Element Method

by

Jung-Wuk Hong

Submitted to the Department of Civil and Environmental Engineering
on September 15, 2003, in partial fulfillment of the
requirements for the degree of
Doctor of Philosophy in Structures and Materials

Abstract

In this thesis we develop some advances in the method of finite spheres which is a truly meshless numerical technique for the solution of boundary value problems on geometrically complex domains. We present the development of a preprocessor for the autogeneration of finite spheres on two-dimensional computational domains. The techniques enable to determine the radii of the spheres as well as to detect the boundary of the analysis domain. The numerical integration for the calculation of stiffness matrices is expensive. However, by utilizing the compact support characteristic it is possible to transform the integral equations into more efficient expressions. The improved equations reduce the effort of integration because for most terms, only line integrations are used. We also propose a new coupling scheme to couple finite element discretizations with finite spheres. The idea is that we can use finite elements and finite spheres simultaneously to utilize their mutual advantages. Hence, we can employ finite spheres only in areas where their use is efficient. In addition, we propose an enriching scheme which makes it possible to superpose spheres on conventional finite element topologies to reach a higher order of convergence in the numerical solution of problems.

Thesis Supervisor: Klaus-Jürgen Bathe
Title: Professor of Mechanical Engineering

Acknowledgments

First, I truly appreciate the sincere guidance and encouragement of Professor Bathe. Without his effort and passion, I would not have been able to pursue my studies at MIT. His inspiring suggestions and ideas have been always very helpful and essential whenever I met some difficulties in my research.

I would like to thank the members of my thesis committee, Professor Franz-Josef Ulm and Professor Kevin Amaratunga for their sincere comments and encouragements throughout my studies. I am very glad to have the opportunity to discuss and interact with them. Also I would like to express my heartful thanks to Professor Jerome Connor and Professor Shi-Chang Wooh for their help.

I also wish to thank my lab members at the Finite Element Research Group, Dr. Uwe Ruppel, Dr. Francisco Montáns, Dr. Thomas Graetsch, Muhammed Baig, Bahareh Banijamali, Philseung Lee, Jacques Olivier, and Omri Pedatzur for their help. Especially I would like to appreciate Dr. Suvranu De at RPI for his help and collaboration on the meshless techniques.

I am deeply grateful to my lovely family, my parents, my wife, Chihyun, my son, Seung-Hyun, my sister, Sung-Hee, brother-in-law, Joon-Young and brother, Sang-Wuk, his wife, Jung-Min, and my lovely nephews and nieces. The cherishing encouragement from them was always the source of the energy for my study and life all the time.

I thank to all the Korean seniors and friends who helped and supported me. Their sincere advice and suggestion worked greatly in my life at MIT.

List of Symbols

A	Interior of a set A.
∂A	Boundary of a set A.
$a(\cdot,\cdot)$	Bilinear operator.
$l(\cdot)$	Linear operator.
Ω	Open bounded domain, $d = 1, 2, 3$.
Γ	Boundary of Ω.
$\mathbf{n}$	Outward normal vector.
$B(\mathbf{x}_I, r_I)$	$\{\mathbf{x} \in \mathbf{X} : \|\|\mathbf{x} - \mathbf{x}\|\| < r_I\}$ Open sphere of radius r.
$S(\mathbf{x}_I, r_I)$	$\{\mathbf{x} \in \mathbf{X} : \|\|\mathbf{x} - \mathbf{x}\|\| = r_I\}$ Surface of the d-dimensional sphere of radius r centered at $\mathbf{x}_I$.
W_I	Weighting function.
$h_{Im}(\mathbf{x})$	The m^{th} shape function at node I.
h	A global measure of the support radii.
$f^{(k)}$	kth derivative of f.
$x \mapsto y$	x is mapped onto y.
$\prod$	Variational potential.
$\|\|\cdot\|\|_{L^1}$	L^1 or sum norm.
$\|\|\cdot\|\|_{L^2}$	L^2 or Euclidean norm.
$\|\|\cdot\|\|_{L^\infty}$	L^∞ or supremum.
δ_{mn}	Kronecker delta.
ε	Error requirement.

C_N	Unit cube in $N-$dimensional space.
$C(\Omega)$	Continuous function on Ω.
$C^k(\Omega)$	k-times differentiable functions on Ω.
$C_0^k(\Omega)$	Functions in C^k vanishing on $\partial\Omega$.
$C(\Omega)$	Continuous function on Ω.
$Q(\cdot)$	Numerical integration operator.
g	Approximation function.
$\mathcal{M}$	Space of model (approximation) functions.
$\mathcal{M}_{\mathbb{P}}$	Space of polynomial model functions.
$\mathbb{N}$	Set of all natural numbers (positive integers).
$\mathbb{P}^N$	Space of all polynomials in N variables.
$\mathbb{P}_d$	Space of all polynomials of maximum degree d.
$\mathbb{R}$	Set of all real numbers.
K_{tg}, K_{tn}	Stress concentration factors.
k_1	Stress intensity factor.
$\mathcal{K}$	Kolosov constant.
G	Shear modulus.

Contents

1 Introduction **23**

1.1 Overview 23

1.2 Thesis outline 30

2 The Theory of the MFS Summarized **33**

2.1 Approximation space 34

2.1.1 The Shepard function 36

2.1.2 Reproducing property 37

2.2 Galerkin weak form for N-dimensional spaces 37

2.3 The Galerkin-based Method of Finite Spheres 40

2.3.1 Approximation functions 40

2.3.2 Displacement-based formulation 45

2.4 Formulation for boundary conditions 50

3 Numerical Integration Theory **53**

3.1 One dimensional numerical integration 54

3.1.1 Construction of quadrature rule by approximation 57

3.1.2 Approximation with polynomials 59
3.1.3 Orthogonal polynomials 61
3.1.4 Gauss formulas 62
3.1.5 Compound quadrature rule 66
3.2 Multi-dimensional numerical integration 68
3.2.1 Construction of formula by approximation 69
3.2.2 Construction of formula by transformation 71
3.2.3 Generalized Cartesian Product Rules 73
3.2.4 Multivariate polynomial approximations 74
3.2.5 Polynomial Interpolation 76
3.2.6 Interpolatory formulas 77

4 Numerical Integration and Auto Sphere Generation for MFS 81

4.1 Improvement of analytical equations for numerical integration for inner sphere 82
4.2 Improvement of analytical equations for numerical integration for lens shape 89
4.3 Numerical integration for method of finite spheres 91
4.3.1 Midpoint integration method for the inner sphere 95
4.3.2 Integration on the lens domain 95
4.4 New integration scheme for the inner spheres and boundary spheres 98
4.5 Automatic generation of spheres in MFS 102
4.6 A numerical result 110

5 Coupling of Finite Elements and Finite Spheres 111

5.1 Introduction 111

5.2 Coupling finite element discretizations with finite sphere discretizations . . 113

5.2.1 Construction of shape function on coupled domain 116

5.2.2 Displacement-based method 119

5.2.3 Formulation in the "pure" finite element domain Ω_{FE} 119

5.2.4 Formulation in "pure" finite sphere domain Ω_{FS} 121

5.2.5 Formulation in the coupled domain 122

5.2.6 Assemblage of stiffness matrix and force vector 127

5.3 Imposing the Dirichlet boundary condition 128

5.3.1 When the restraint is applied in both normal and tangential directions 129

5.3.2 When the restraint is applied only in the normal direction or the tangential direction 132

5.4 Enriching the finite element functions 135

6 Examples of Coupling Methods **139**

6.1 Tension and bending test of coupled elements. 139

6.1.1 Test geometry and loading conditions 139

6.1.2 Tension and bending test result of a simple plate 142

6.2 Specialized examples 142

6.2.1 Plate with a hole 145

6.2.2 Plate with a crack 154

7 Conclusions and Remarks **163**

A Fundamentals of Functional Analysis **167**

A.1 Vector spaces 167

A.2 Hilbert space 168

A.3 Lebesgue spaces, $L^p(\Omega)$ 170

A.4 Sobolev spaces 171

A.5 $C^m(\Omega)$ spaces 171

A.6 Dual spaces 173

B Cubature rules **175**

B.1 Midpoint rule 175

B.2 Gauss integration on a segment 176

List of Figures

1-1 Isoparametric finite elements: (a) Due to small angle θ, this element becomes "sliver" element. (b) There is an angle bigger that 180°, so the one-to-one mapping is not satisfied. 28

1-2 Fluid structure interaction 2-D model. In the channel, there is a slender plate which interacts with the fluid flow. In the FEM modelling, this example may require extensive remeshing to simulate the behavior of the plate. . 28

2-1 A schematic of method of finite spheres 35

2-2 A set of four subfigures. 41

2-2 Weighting function and derivatives (Cont'd): (c) Second derivative of W_I. (d) Third derivative of W_I 42

2-3 A set of four subfigures. 44

2-4 Node distribution for the imposition of Dirichlet boundary condition. Nodes are arranged along the boundary to circumvent to have complicated integration domain. 51

3-1 Riemann integration: right-side point rule is applied to integrate a function $f(x)$ from a to b. 56

3-2 Lagrangian polynomials. 63

3-3 Legendre polynomials [1]. 65

4-1 Pressure load is applied on cantilever plate. 83

4-2 Finite sphere node arrangement. The nodes are uniformly distributed. . . . 83

4-3 Integrand distributions in Equation (4.1). 84

4-4 Numerical integration scheme with newly derived equations from (4.20) to (4.23). 89

4-5 Figures of (a) inner sphere, (b) contact sphere, (c) boundary sphere on Neumann boundary Γ_f, (d) boundary sphere on Dirichlet boundary Γ_u 92

4-6 Inner sphere integration scheme. Midpoint rule is applied, and the sampling points are determined by Equations (4.36) and (4.37). 93

4-7 Lens integration scheme, where A_j is the area of a strip, w_i^x is the width of the small piece. 94

4-8 A integration scheme for lens domain. Overlapped region is decomposed into pieces and the variables are calculated. 94

4-9 New integration scheme for the inner sphere. (a) The sphere J is divided into four domains based on the angle and determine neighboring spheres which are located in each region of angle. (b) Boundary sphere. 101

4-10 Automatic radius calculation scheme. 102

4-11 Edge table generation scheme. Each row of the edge table contains information about the nodes that are on an element edge. The format is (N1,N2,flipping flag), where N1 and N2 are the nodes connected be the edge and the flipping flag takes on a value of zero if the order is N2 $<$ N1 in the original connectivity and a value of 1 if the original order is reversed. 103

4-12 Inner sphere: The radius is determined by average value of node-distance of neighboring nodes. 104

4-13 Contact sphere: Node (I) has at least two neighborhood nodes which require special attention. The normal distance from node I to adjacent edges are computed and the minimum distance is adopted as radius 105

4-14 Boundary sphere: The boundary nodes are obtained from the boundary table. The radius of the sphere at a boundary node is selected as the minimum of the two nearest neighbor distances. The included angles θ_1 and θ_2 are used in the numerical integration 106

4-15 Example of auto sphere generation: The plate has two holes and sphere generation is implemented automatically. 175 spheres are distributed to cover the whole domain. 107

4-16 Example of auto sphere generation: For the annular section sphere generation is implemented automatically. 37 spheres are distributed to cover the whole domain. 108

4-17 Example of auto sphere generation: For the quarter of a plate which has a hole sphere generation is implemented automatically. 168 spheres are distributed to cover the whole domain. 109

4-18 Convergence comparison of finite element method and method of finite spheres. 110

5-1 Coupling finite element discretized domains with finite spheres discretized domains: (a) Coupling scheme and (b) computational domain decomposition. We call Ω_{FE} the domain which does not have any overlapping with finite spheres, Ω_{FE-FS} the union of finite elements which have non-zero overlap with spheres, and Ω_{FS} the region which consists of spheres. 114

5-2 Enriching a finite element discretization with finite spheres: We call Ω_{FE} the domain which is not enriched with finite spheres, and Ω_{FE-FS}, the domain of finite elements enriched with spheres. It should be noted that there is no pure finite sphere domain. 115

5-3 Shape functions $h_1^{FE-FS}(x)$, $h_2^{FE-FS}(x)$, $\rho_1^{FE-FS}(x)$, $\rho_2^{FE-FS}(x)$, $h_{11}^{FE-FS}(x)$, and $h_{21}^{FE-FS}(x)$ calculated by Equation (5.3) in a 1-dimensional case when the spheres are located at the both ends, where $R_1, R_2 = 1$. 117

5-4 Various kinds of Dirichlet boundary conditions: (a) u^n and u^t are fixed, (b) u^n is fixed and u^t is free, and (c) u^n is freed and u^t is fixed. 129

5-5 Stresses on the inclined surface. n is normal vector to the inclined surface and t is tangential direction vector. 134

5-6 Shape functions $h_1^{FE-FS}(x)$, $h_2^{FE-FS}(x)$, $\rho_1^{FE-FS}(x)$, $\rho_2^{FE-FS}(x)$, $h_{11}^{FE-FS}(x)$, and $h_{21}^{FE-FS}(x)$ in a 1-dimensional case when the spheres are located at the both ends, where $R_1, R_2 = 0.5$. 137

6-1 Loading conditions for patch test of the coupling scheme. (a) unit tensile stress and (b) linear pressure distribution resulting in unit moment load are applied on the right end of the plate. For the material properties, $E = 100$ and $\nu = 0.3$. Element is under the plane strain condition 140

6-2 Sphere arrangements on a 4-node element. (a) Two spheres are located on the right side of 4-node element and (b) four spheres are placed on each node of4-node element. The coupled node means that it contains finite element node and finite sphere node simultaneously. 140

6-3 Element refinements. (a) 1 element, (b) 2 elements, (c) 4 elements, (d) 8 elements, and (e) 16 elements are employed. L is the original length of the plate. W is the width of the plate with refinements. 141

6-4 Convergence curves with different sphere allocations shown in Figure 6-2. . 144

6-5 Geometry of a plate with a hole in the middle of the plate. a is the radius of the hole, b is the half of the width (L_1) of the plate L_2 is the length of the plate and $d = 2a$ is the diameter of the hole. The plate is subjected to lateral tensile pressure P under the plane stress condition. 146

6-6 Stress concentration factors K_{tg} and K_{tn} for the tension of a finite-width thin plate with a circular hole (Rowland 1929-30). 148

6-7 ADINA result: 4096 9-node elements are used. Stress (σ_{xx}) concentration at the vicinity of the hole can be observed. The plate has the geometry, boundary condition and loading condition in Figure 6-5. The Young's modulus is 100 and Poisson ratio is 0.3. in the plane strain condition. The maximum stress in horizontal direction is 3.008. 149

6-8 Stress (σ_{xx}) concentration at the vicinity of the hole. The plate has the geometry, boundary condition and loading condition in Figure 6-5. The Young's modulus is 100 and Poisson ratio is 0.3 under the plane stress condition. 16 elements (4-nodes) are used. 150

6-9 Stress (σ_{xx}) concentration at the vicinity of the hole. The plate has the geometry, boundary condition and loading condition in Figure 6-5. The Young's modulus is 100 and Poisson ratio is 0.3 under the plane stress condition. 64 elements (4-nodes) are used. 150

6-10 Stress (σ_{xx}) concentration at the vicinity of the hole. The plate has the geometry, boundary condition and loading condition in Figure 6-5. The Young's modulus is 100 and Poisson ratio is 0.3 under the plane stress condition. 256 elements (4-nodes) are used. 151

6-11 Stress (σ_{xx}) concentration at the vicinity of the hole. The plate has the geometry, boundary condition and loading condition in Figure 6-5. The Young's modulus is 100 and Poisson ratio is 0.3 under the plane stress condition. 16 elements (4−nodes) are used and the radius of each sphere added on the finite elements is 0.4. 152

6-12 Stress (σ_{xx}) concentration at the vicinity of the hole. The Young's modulus is 100 and Poisson ratio is 0.3 under the plane stress condition. 64 elements (4−nodes) are used and the radius of each sphere added on the finite elements is 0.2. 152

6-13 Stress (σ_{xx}) concentration at the vicinity of the hole. The Young's modulus is 100 and Poisson ratio is 0.3 under the plane stress condition. 256 elements (4−nodes) are used and the radius of each sphere added on the finite elements is 0.1. 153

6-14 (a) geometry of a plate which has a sharp crack in the middle. The Young's modulus is 100 and the poisson ratio is 0.3. The plate is under the plane strain condition. (b) local coordinate system. 155

6-15 Enriching scheme: Stress (σ_{xx}) distribution along the vertical direction from the crack tip. 158

6-16 Stress (σ_{xx}) concentration at the crack tip. The plate has the geometry, boundary condition and loading condition in Figure 6-14. The Young's modulus is 100 and Poisson ratio is 0.3 under the plane strain condition. 16 elements (4-nodes) are used. 159

6-17 Stress (σ_{xx}) concentration at the crack tip. The plate has the geometry, boundary condition and loading condition in Figure 6-14. The Young's modulus is 100 and Poisson ratio is 0.3 under the plane strain condition. 64 elements (4-nodes) are used. 159

6-18 Stress (σ_{xx}) concentration at the crack tip. The plate has the geometry, boundary condition and loading condition in Figure 6-14. The Young's modulus is 100 and Poisson ratio is 0.3 under the plane strain condition. 256 elements (4-nodes) are used. 160

6-19 Enriching scheme: Stress (σ_{xx}) concentration at the crack tip. The plate has the geometry, boundary condition and loading condition in Figure 6-14. The Young's modulus is 100 and Poisson ratio is 0.3 under the plane strain condition. 16 elements (4-nodes) are used and the radius of each sphere added on the finite elements is 0.5. 161

6-20 Enriching scheme: Stress (σ_{xx}) concentration at the crack tip. The plate has the geometry, boundary condition and loading condition in Figure 6-14. The Young's modulus is 100 and Poisson ratio is 0.3 under the plane strain condition. 64 elements (4-nodes) are used and the radius of each sphere added on the finite elements is 0.25. 161

6-21 Enriching scheme: Stress (σ_{xx}) concentration at the crack tip. The plate has the geometry, boundary condition and loading condition in Figure 6-14. The Young's modulus is 100 and Poisson ratio is 0.3 under the plane strain condition. 256 elements (4-nodes) are used and the radius of each sphere added on the finite elements is 0.125. 162

B-1 Midpoint rule integration. 176

B-2 Gauss integration on a segment. 177

List of Tables

1.1 Various meshless methods which have been developed and the formulation principles are listed. MLS means that moving least square method. 24

3.1 Quadrature abscissas and corresponding Gauss formula. 66

4.1 Establishment of subsections for sphere integration. 99

6.1 Strain energy of coupled elements in tension and moment. Scheme (a) represents two sphere allocation on the right side and scheme (b) means four sphere allocation on each node of 4-node element as shown in Figure 6-2. $\mathbf{T}$ means tension and $\mathbf{M}$ means moment. We consider the plane strain condition, $E = 100$ and $\nu = 0.3$. The equivalent strain energy is calculated by multiplying number of elements. The exact strain energy for tensional loading is 0.00455 and for bending is 0.0546. 143

6.2 Comparison of maximum stress value (σ_{xx}) in the plate with a hole shown in Figure 6-5. The exact value is assumed as 3.008. 151

6.3 Comparison of maximum value of stress σ_{xx} on the crack tip. 157

Chapter 1

Introduction

1.1 Overview

Frequently we need to analyze models subjected to continuous changes in the geometry such as large deformations in fluid structure interaction and crack propagation problem. To avoid large element distortions and collapse of elements and obtain accurate results, we need to remesh the model many times, and this calculation is cumbersome and expensive. Meshless techniques have advantages since sophisticated adaptive mesh generations are not needed.

Over the past eight years a variety of meshless techniques [2] have been developed such as the smoothed particle hydrodynamics method [3], the diffuse element method [4], the element free Galerkin (EFG) method [5], the reproducing kernel particle method [6], the partition of unity finite element method (PUFEM) [7], the *hp*-clouds method [8, 9], the finite point method, the local boundary integral equation method [10], the meshless local Petrov-Galerkin (MLPG) method [11], and the particle partition of unity method [12]. The

Method	System Equation	Approximation
Method of finite spheres [13]	Weak form	Partition of unity
Diffuse element method [4]	Weak form	MLS approximation
Element Free Galerkin Method [5]	Weak form	MLS approximation
Meshless local Petrov-Galerkin method [11]	Weak form	MLS approximation
Finite point method [14]	Strong form	Finite difference
Smoothed particle hydrodynamics [3]	Strong form	Integral representation
Reproducing kernel particle method [6]	Strong form	Integral representation
hp-clouds method [8, 9]	Weak form	MLS approximation
Partition of unity FEM [7]	Weak form	Partition of unity
Particle partition of unity [12]	Weak form	Partition of unity

Table 1.1: Various meshless methods which have been developed and the formulation principles are listed. MLS means that moving least square method.

names of meshless techniques and each basic principle used for the formulation are listed in Table 1.1.

On the other hand, we can also classify these techniques considering how to construct the shape functions into three major categories:

1. Finite integral representation methods:

   (a) Smoothed particle hydrodynamic (SPH) method

   (b) Reproducing kernel particle method (RKPM)

2. Finite series representation methods:

   (a) Partition of unity method (PU)

   (b) Moving least squares methods (MLS)

3. Finite differential representation methods:

   (a) Finite difference method

   (b) Finite point method

In the finite integral representation method, the unknown function is represented in a local domain via an integral form as

$$f(x) = \int_{x_1}^{x_2} f(\xi) W(x - \xi) d\xi, \tag{1.1}$$

where $W(\xi)$ is a kernel or smoothing function. Finite series representation methods are well developed in FEM, and also applicable to meshless techniques. The function is defined as

$$f(x) = a_0 + a_1 p_1(x) + a_2 p_2(x) + a_3 p_3(x) + \cdots, \tag{1.2}$$

where $p_i(x)$ are basis functions. Finite difference methods use Taylor series expansions to represent a function as

$$f(x) = f(x_0) + f'(x_0)(x - a) + \frac{1}{2!} f^2(x_0)(x - a)^2 + \cdots, \tag{1.3}$$

The weighting functions play an important roles in meshless techniques and many kinds of shape functions have been suggested,

1. Cubic spline function:

$$W(s) = \begin{cases} 2/3 - 4s^2 + 4s^3 & \text{for } s \leq \frac{1}{2}, \\ 4/3 - 4s + 4s^2 - 4/3s^3 & \text{for } 1/2 \leq s \leq 1, \\ 0 & \text{for } s \geq 1. \end{cases} \tag{1.4}$$

2. Quartic spline function:

$$W(s) = \begin{cases} 1 - 6s^2 + 8s^3 - 3s^4 & \text{for } s \leq 1, \\ 0 & \text{for } s \geq 1. \end{cases} \tag{1.5}$$

3. Exponential weight function:

$$W(s) = \begin{cases} \exp^{-(s/\alpha)^2} & \text{for } s \leq 1, \\ 0 & \text{for } s \geq 1. \end{cases} \tag{1.6}$$

where α is a constant coefficient and we often use $\alpha = 0.3$. The variable s is the normalized distance from the node as

$$s = \frac{|\mathbf{x} - \mathbf{x}_I|}{R_I}. \tag{1.7}$$

In the method of finite sphere we use the quartic spline function since it has a simple form of one single piece.

Although there have been some achievements in the formulations and theoretical proofs, the efficiency of meshless techniques is still a most important and difficult task. The method of finite spheres was developed by S. De. and K. J. Bathe [13]. In this technique, the domain is discretized by spheres. Each sphere has a node at its center and the overlapping of

the spheres is allowed. The only one requirement is that the union of spheres mush cover whole domain without any emptiness.

From the mathematical view point, the finite element method is a weighted residual scheme, and the solution is considered to reside in the considered vector space. Furthermore, the error is orthogonal to a set of test functions. A great advantage of the finite element method is that Hilbert solution spaces are used via a weak formulation. In the finite element method, the domain is the subdivided into subregions, called "elements", and this is the most important concept in the finite element formulation since the governing equation is integrated over the elements in the weak form. However, to have a good quality of mesh, certain conditions should be satisfied.

In the isoparametric formulation, the Jacobian matrix is utilized to transform the coordinate system from local coordinates of (x, y) to natural coordinates of (r, s). The Jacobian matrix is non-singular when the one-to-one mapping condition is satisfied. It means that a point in the x-y plane should correspond to only one point in the r-s plane, and conversely [2].

To be able to invert the Jacobian matrix, the element should not be distorted too much or folded. This restriction makes the mesh generation a enormous task in FEM analysis. Since this task requires more time than the actual numerical calculations in the analysis, avoiding the mesh generation is the main motivation of meshless techniques.

The creation of a mesh for the entire domain is the unavoidable prerequisite in solution based on finite element methods. Much time in the analysis is spent on mesh generation and checking the quality of the mesh. Especially, for large deformation problems, as for example shown in Figure 1-2, the quality of meshes affects the accuracy tremendously.

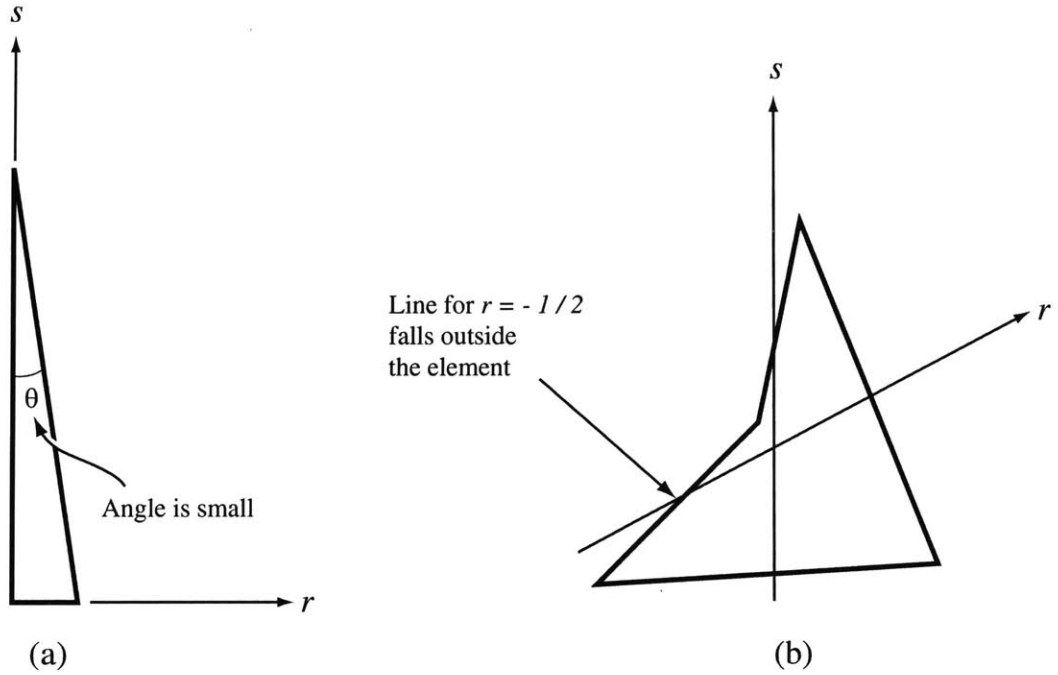

Figure 1-1: Isoparametric finite elements: (a) Due to small angle θ, this element becomes "sliver" element. (b) There is an angle bigger that 180°, so the one-to-one mapping is not satisfied.

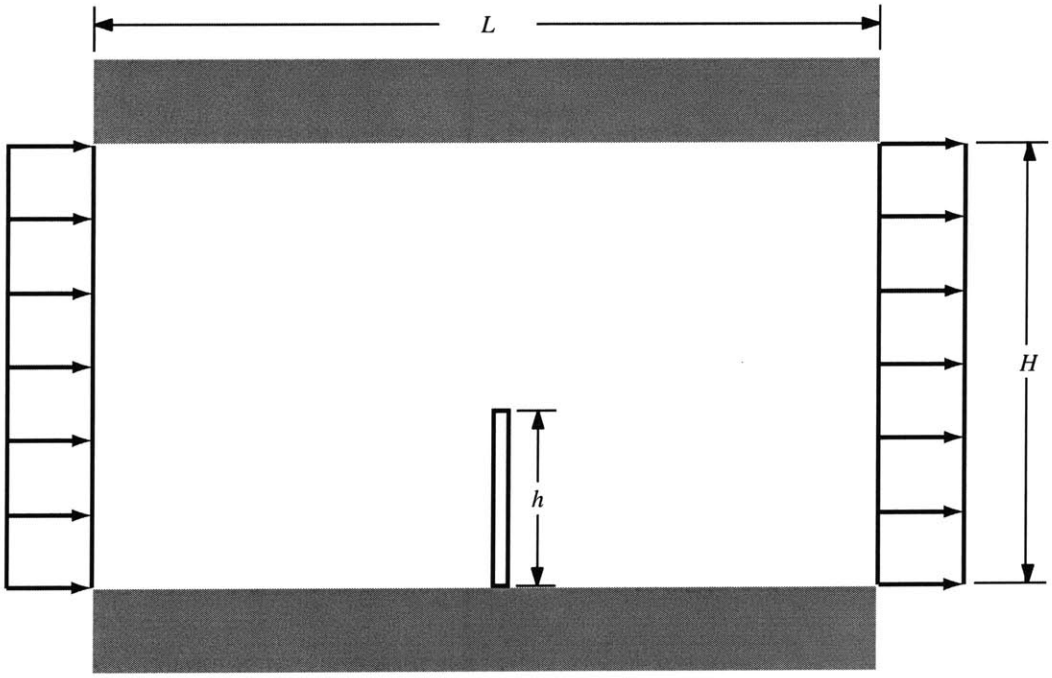

Figure 1-2: Fluid structure interaction 2-D model. In the channel, there is a slender plate which interacts with the fluid flow. In the FEM modelling, this example may require extensive remeshing to simulate the behavior of the plate.

Another restriction for the analysis is that the deformation cannot exceed the element size, Hence, adaptive procedures must be implemented at each time step of calculation in the FEM methods.

A variety of meshless techniques have been developed, but the currently available techniques are still much more expensive than finite element methods. The main reason is that the shape functions are determined as non-polynomials although the functions are smooth ($\in C^{\infty}$). Therefore, for the numerical integration more cost is needed than in the finite element method. Indeed, computational efficiency and reliablility are the most important issues for the development of the meshless techniques.

The method of finite spheres is a truly meshless technique, and the discretization is achieved by constructing Partition of Unity functions in the domain. The advantage of choosing the spherical local support is that the relative location can be described simply with their center coordinates and radii and the compact supportness ensures the narrow bandedness of the stiffness matrices.

In the traditional finite element method, the interpolation functions are polynomials which have the Kronecker delta property, and this ensures that the Dirichlet boundary conditions are satisfied in the weak sense. In addition, the basis functions make the numerical integration relatively convenient by the Gauss-Legendre quadrature rule. When the degree of the polynomial is known, the Gauss-Legendre rule can integration up to $(2 \times N - 1)$ degree exactly. However, in the method of finite spheres the interpolation functions are not polynomials and they are *rational functions*. Hence more efficient numerical integration schemes should be developed to have required accuracy.

We also propose a coupling scheme and an enriching scheme. These can be considered

to generalize the numerical solution method, since we use conventional finite elements and finite spheres simultaneously. This provides several advantages because we can employ finite spheres only in those regions where they are effective. For example, in a crack propagation problem, we can add spheres easily to the tip of the crack to capture stress and strain concentrations. The finite element refinement around the crack tip can thus be largely dispensed with. In addition, the total cost of numerical integration is not that large since we use finite spheres on just certain local regions, not on the entire domain.

1.2 Thesis outline

A brief description of this thesis is as follows:

In Chapter 2, we summarize the basic formulations of the method of finite spheres based on the displacement approach. The construction of the approximation functions by the partition of unity is described.

In Chapter 3, the fundamental theory of numerical integration is summarized. We start from the one-dimensional problem and extend to multi-dimensional concepts. Basic principles of Gauss formula, compound formula, orthogonal polynomials and the approximation theory are briefly described.

In Chapter 4, we derive the improved equations of the integrand functions by transforming the original equations into much simpler equations. This improvement reduces the dimension of numerical integrations in many terms. We address the automatic sphere generation to cover the entire domain imported from a FEM package data file. The geometries and boundaries are detected and optimal radii of spheres are determined.

In Chapter 5, we present two new techniques to couple finite elements and finite spheres. The first scheme couples finite elements and finite spheres simultaneously and the second scheme is an enriching scheme. Different from existing schemes, the new techniques guarantee the consistency in the coupled domain in the displacement field.

In Chapter 6, we give resuts regarding a simple tension and bending test with the coupling scheme and verify the convergence of strain energy. Then with the enriching scheme, a stress concentration phenomena are analyzed by solving a plate with a hole and a plate with a crack. The comparisons with analytical solutions are performed.

Chapter 2

The Theory of the MFS Summarized

The first step in the Galerkin procedure is to construct finite dimensional subspaces in a Sobolev space, where the unique solution is assumed to exist. The creation of shape functions is the most important part in the meshless technique, and the challenging issue is how to establish good shape functions with only nodes and radius. The requirements for the "good" shape functions are [15]:

1. Arbitrary nodal distribution.

2. The shape function should satisfy a certain order of completeness.

3. Compact support of the shape functions.

4. The algorithm should be computationally efficient.

5. The shape function should have the Kronecker delta property

6. The field approximation should be compatible within the entire domain.

It should be noted that the terms completeness and compatibility are used distinctively since the completeness/consistency means the capability of the field function approximation method to reproduce the fields of lowest orders of complete polynomials at any point in the domain. The compatibility is the continuity of the approximation on the boundaries between the sub-domains.

In the method of finite spheres we choose partition of unity functions for constructing the trial function spaces. This choice allows the rigid body motion and zero strain condition. We discuss the partition of unity and the approximation properties of the trial function. The consistency, local approximation, continuity, and compact support are our desirable characteristic for the method of finite sphere. The *consistency* means polynomial reproducing property to ensure rigid body motion and constant strain states. This condition depends on the form of the partial differential equation. The compact support is that the function is non zero only on the concerned domain. This characteristic is essential to have a sparse matrix not fully coupled.

2.1 Approximation space

We adopted the partition of unity function to construct the approximation space and sphere domain for the compactness as shown in Figure 2-1.

The total analysis domain consists of the open compact domain Ω and the closure Γ. A set of spheres which have open domain $B(\mathbf{x}_I, r_I)$ and closure $S(\mathbf{x}_I, r_I)$ covers the whole domain Ω, in which $\mathbf{x}_I$ and r_I are the center and radius of the I^{th} sphere respectively. The spheres can be entirely in the domain, contact the boundary, or have non-zero intersection

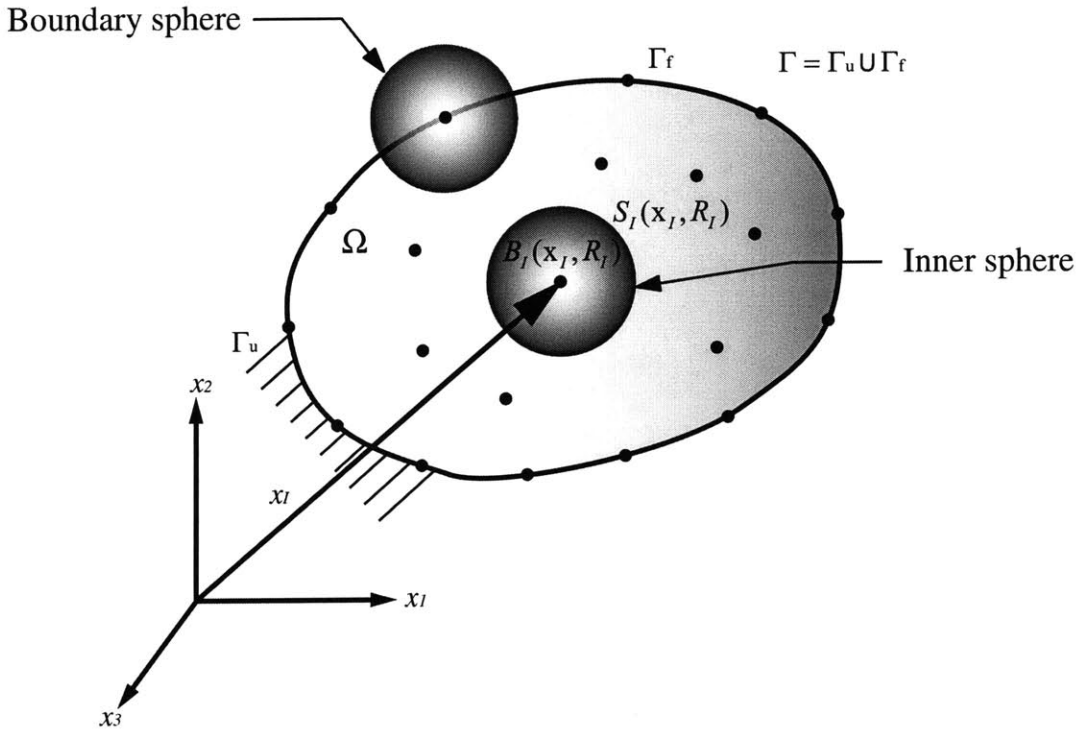

Figure 2-1: A schematic of method of finite spheres

with the boundary (boundary sphere).

2.1.1 The Shepard function

We can start from the proposition [16] of

Proposition 2.1.1 *Let G be an open set of R^n. Let a family $\{U\}$ of open subsets U of G constitute an* open base *of G: any open subset of G is representable as the union of open sets belonging to the family U. Then there exists a countable system of open sets of the family U with the properties: the union of open sets of this system equals G, any compact subsets of G meets only a finite number of open sets of this system.*

Theorem 2.1.2 (The partition of unity) *Let G be an open set of R^n. Let a family of open subsets $\{G_i; i \in I\}$ cover G, i.e., $G = \bigcup_{i \in I} G_i$. Then there exists a system of functions $\{\rho_j(x); j \in J\}$ of $C_0^\infty(R^n)$ such that*

$$\text{for each } j \in J,\ \operatorname{supp}(\rho_j) \text{ is contained in some } G_i, \tag{2.1}$$

$$\text{for every } j \in J,\ 0 \leq \rho_j(x) \leq 1, \tag{2.2}$$

$$\sum_{j \in J} \rho_j(x) = 1 \text{ for } x \in G. \tag{2.3}$$

The partition of unity function has these characteristics

$$\begin{aligned} &1.\quad \sum_{I=1}^{N} \rho_I = 1 \quad \forall \mathbf{x} \in \Omega. \\ &2.\quad \operatorname{supp}\{\rho_I(x)\} \subset B(\mathbf{x}_I, r_I). \\ &3.\quad \rho_I \in C_0^m,\ m \geq 0. \end{aligned} \tag{2.4}$$

2.1.2 Reproducing property

Reproducing property is one of requirements for a good approximation space. The statement is that if any function $p_k(\mathbf{x})$ is included in the local basis of each sphere, it is possible to exactly reproduce it on the entire domain (Ω).

Proof: We may write

$$v_h(\mathbf{x}) = \sum_{I=1}^{N} \sum_{m \in \Im} \rho_I(\mathbf{x}) p_m(\mathbf{x}) \alpha_{Im}, \tag{2.5}$$

and if we set $\alpha_{Im} = \delta_{mk}\ \forall I$, where δ_{mk} is the Kronecker delta, then this δ_{mk} is unity when there exists the corresponding polynomial. Using the partition of unity,

$$v_h(\mathbf{x}) = \sum_{I=1}^{N} \rho_I(\mathbf{x}) \sum_{m \in \Im} p_m(\mathbf{x}) \alpha_{Im} = p_k. \tag{2.6}$$

2.2 Galerkin weak form for N-dimensional spaces

We consider open bounded domain $\Omega \in R^d (d = 1, 2, \ldots, n)$, and its close Γ. In the term of partial differential operator,

$$\mathcal{A}u = f \qquad \text{in } \Omega, \tag{2.7}$$

in which linear differential operator $\mathcal{A}$ can be defined as

$$\{\mathcal{A} : \forall v \ \in H^2(\Omega) \longrightarrow L^2\}. \tag{2.8}$$

For the elasticity problem in n-dimensions, the operator [17] is

$$\mathcal{A} = \sum_{i,j=1}^{d} a_{ij}(\mathbf{x}) \frac{\partial^2}{\partial x_i \partial x_j} + c(\mathbf{x}), \tag{2.9}$$

and a_{ij} and c are bounded. We have Dirichlet and Neumann boundary conditions, and these are described in mathematical forms as

$$\sum_{i,j=1}^{d} a_{ij}(\mathbf{x}) \frac{\partial u}{\partial x_i} n_i = f^s \qquad \text{on } \Gamma_f \tag{2.10}$$

$$u = u^s \qquad \text{on } \Gamma_u \tag{2.11}$$

where n_i is the outward unit normal component along the boundary, $\Gamma = \Gamma_u \bigcup \Gamma_f$, and $\Gamma_u \bigcap \Gamma_f = 0$. The solution of this equation can be found by setting the difference between exact solution u and u_h orthogonal to the space of $v_h(x)$ space. Therefore, we can establish equations for each node as

$$\Big(\mathcal{A}(u_h) - f, h_{Im}\Big) = 0, \qquad \forall\, m \in \Im \tag{2.12}$$

For generating approximation spaces with higher order consistency, the local approximation space $V_I^h = \underset{m \in \Im}{\text{span}}\{p_m(x)\}$ is defined at each node I, where p_m is a polynomial function and $\Im$ is an index set. The h is the superscript which represents the radius of the sphere.

The global approximation spaces V_h are generated by multiplying the PU function with

the local basis polynomial functions, so we have

$$V_h = \sum_{J=1}^{N} \rho_J V_J^h. \tag{2.13}$$

Therefore, any function $v_h \in V_h$ can be expressed as follows:

$$v_h = \sum_{J=1}^{N} \sum_{n \in \Im} h_{Jn}(\mathbf{x}) \alpha_{Jn} \tag{2.14}$$

where $h_{Jn}(\mathbf{x}) = \rho_J(\mathbf{x}) p_n(\mathbf{x})$, and we call h_{Jn} a shape function associated with n^{th} degree of freedom of node J. By Equation (2.14) and Green's theorem, we obtain the equation for the m^{th} degree of freedom of I^{th} node as

$$\sum_{I=1}^{N} \sum_{m \in \Im} K_{ImJn} \alpha_{Jn} = f_{Im} + \hat{f}_{Im}, \tag{2.15}$$

where

$$\begin{aligned} K_{ImJn} &= a(h_{Im}, h_{Jn}) \\ &= \int_{\Omega_I} c(\mathbf{x}) h_{Im} h_{Jn} d\Omega + \sum_{i,j=1}^{n} a_{ij}(\mathbf{x}) \frac{\partial h_{Im}}{\partial x_i} \frac{\partial h_{Jn}}{\partial x_j} d\Omega. \end{aligned} \tag{2.16}$$

It should be noted that $a(\cdot, \cdot)$ is bilinear operator, and

$$f_{Im} = \int_{\Omega_I} f(\mathbf{x}) h_{Im} d\Omega, \tag{2.17}$$

$$\hat{f}_{Im} = \sum_{i,j=1}^{n} \int_{B(\mathbf{x}_I, \mathbf{r}_I) \bigcap \Gamma} h_{Im} n_i a_{ij}(\mathbf{x}) \frac{\partial u_h}{\partial x_j} d\Gamma, \tag{2.18}$$

where $\Omega_I = B(\mathbf{x}_I, \mathbf{r}_I) \bigcap \Omega$.

2.3 The Galerkin-based Method of Finite Spheres

We briefly review in this section the basic formulation of the method of finite spheres.

2.3.1 Approximation functions

Based on the partition of unity requirement, we construct the basis functions. The domain $\Omega \in R^d$ is an open bounded domain with Γ its boundary as shown in Figure 2-1.

Each sphere consists of an open sphere $B_I(\mathbf{x}_I, R_I)$ and its closure $S_I(R_I)$, where $\mathbf{x}_I$ is the center of the sphere and R_I is its radius. The set of spheres must cover the entire domain, i.e., $\Omega \subset \bigcup_{I=1}^{N} B_I(\mathbf{x}_I, R_I)$, and some of them will have non-zero intersections with the boundary; hence those spheres are considered to be *boundary spheres.*

We define a weighting function $W_I(s_I)$, where $s_I = \dfrac{\|\mathbf{x} - \mathbf{x}_I\|}{R_I}$, which means that the weighting function is normalized by the radius of the sphere. This weighting function has compact support, and we have chosen a quartic spline weighting function of the following form as illustrated in Figure 2-2 (a).

$$W(s_I) = 1 - 6{s_I}^2 + 8{s_I}^3 - 3{s_I}^4; \qquad 0 \leq s_I \leq 1. \tag{2.19}$$

There are several well-known weighting functions for meshless techniques such as exponential, cubic spline, quartic, and SPH spline which all vanish at the boundary of support. Also, the first derivative vanishes at $s_I = 0$ and $s_I = 1$. The first derivative of the weighting

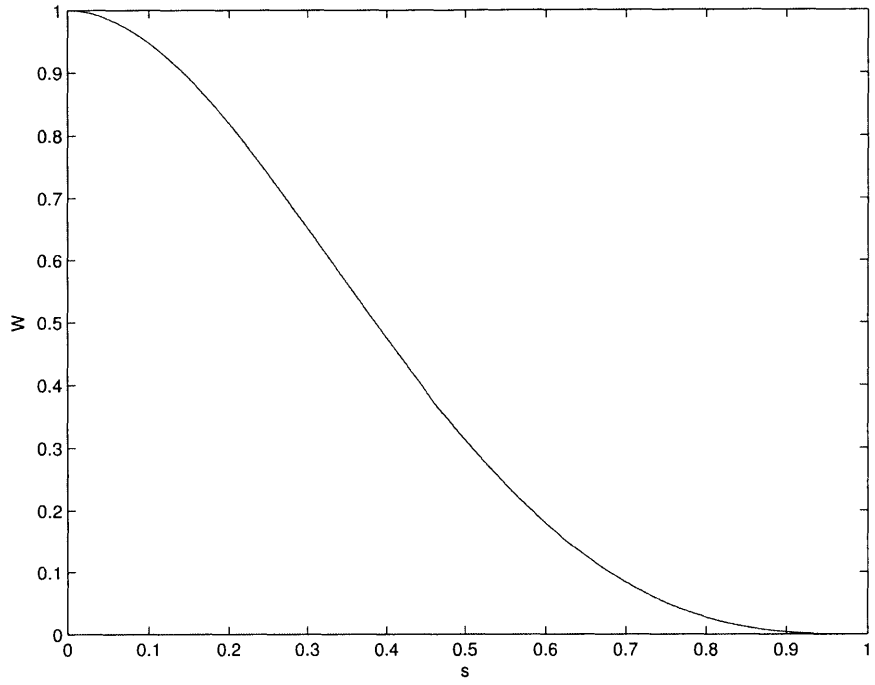

(a)

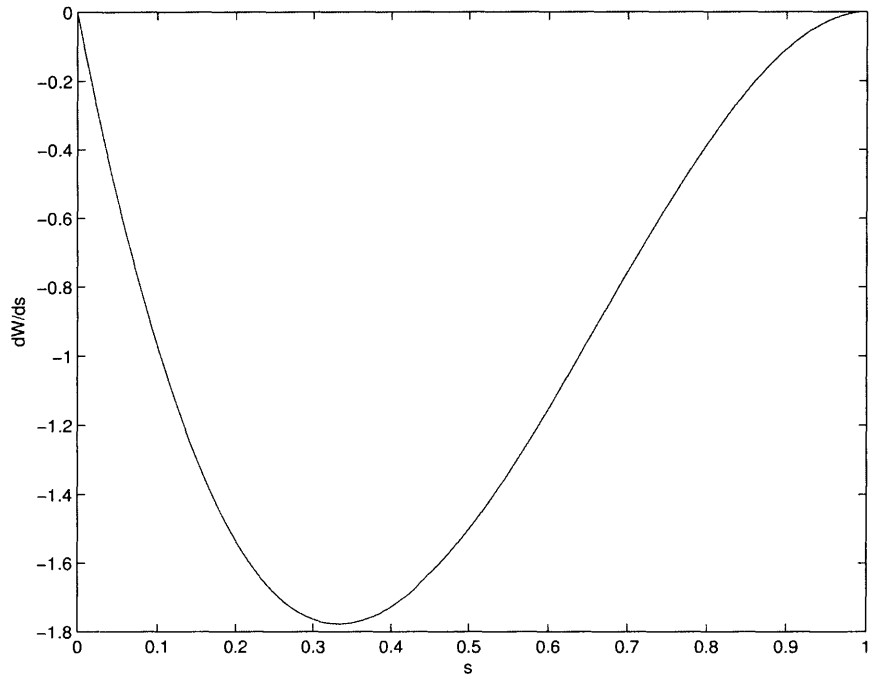

(b)

Figure 2-2: Weighting function and derivatives: (a) Weighting function $W_I(x)$ when $x_I = 0$ and $R = 1.0$ in one dimensional case. (b) First derivative of W_I with x. The derivatives vanishes at $x = 0$ and $x = 1$.

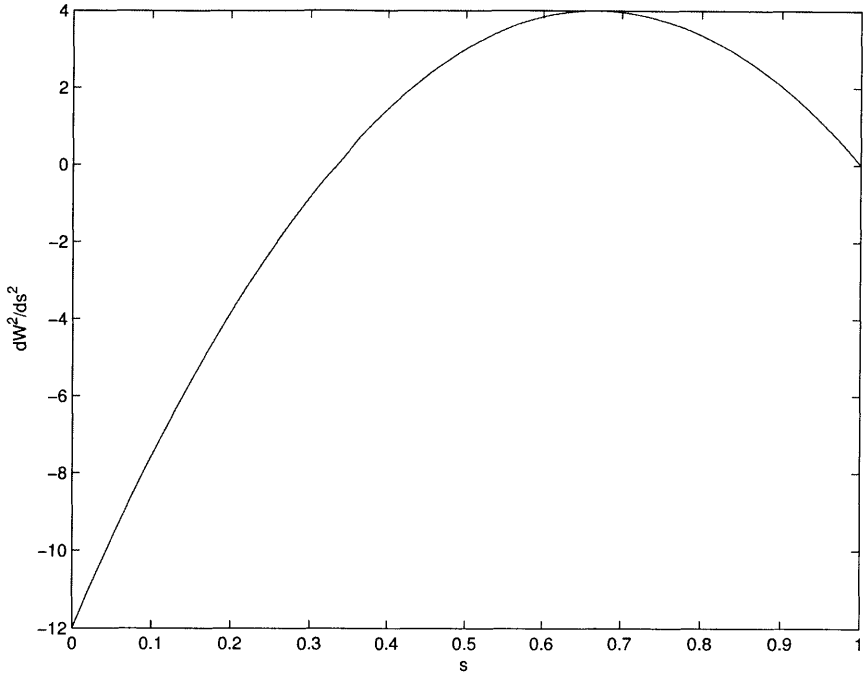

(c)

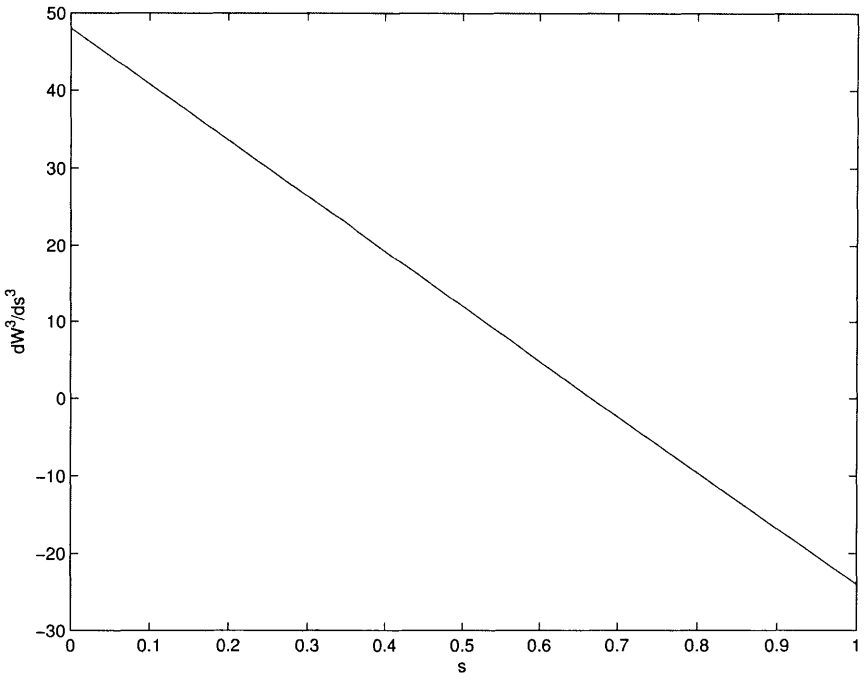

(d)

Figure 2-2: Weighting function and derivatives (Cont'd): (c) Second derivative of W_I. (d) Third derivative of W_I

function is

$$\frac{dW(s_I)}{ds_I} = -12s_I + 24s_I^2 - 12s_I^3, \tag{2.20}$$

To calculate the first derivative of W_I, we use the chain rule

$$\frac{\partial W_I}{\partial x} = \frac{\partial W_I}{\partial s_I}\frac{\partial s_I}{\partial x}, \tag{2.21}$$

and we have

$$\frac{\partial s}{\partial x} = \frac{(x - x_I)}{R_I^2}\frac{1}{s_I}. \tag{2.22}$$

finally, we have the simple form of the derivative as

$$\frac{\partial W_I}{\partial x} = -12(1 - {s_I}^2)\frac{(x - x_I)}{R_I^2}. \tag{2.23}$$

In the similar manner,

$$\frac{\partial W_I}{\partial y} = -12(1 - {s_I}^2)\frac{(y - y_I)}{R_I^2}. \tag{2.24}$$

As an example, in two-dimensional the weighting function $W_I(\mathbf{x})$, $\partial W_I(\mathbf{x})/\partial x$, and $\partial W_I(\mathbf{x})/\partial y$ are illustrated in Figure 2-3. With the weighting functions we can define the Shepard partition of unity functions

$$\rho_I(\mathbf{x}) = \frac{W_I(\mathbf{x})}{\sum_{J=1}^{N} W_J(\mathbf{x})}, \qquad I = 1, 2, \ldots, N. \tag{2.25}$$

For generating approximation spaces with higher order consistency, local approximation spaces $V_I^h = \underset{m \in \Im}{\text{span}}\{p_m(\mathbf{x})\}$ are defined at the nodes, where p_m is a polynomial function

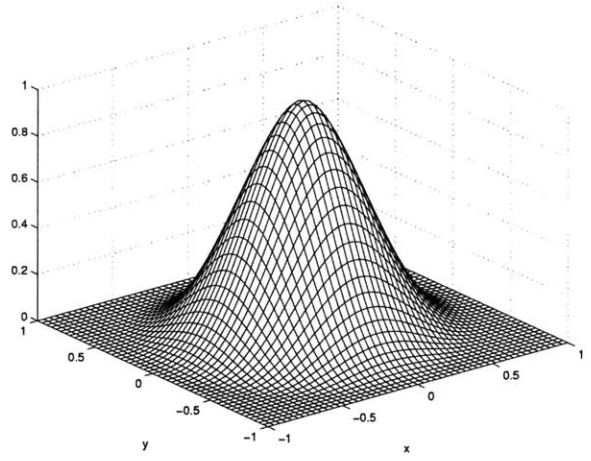

(a)

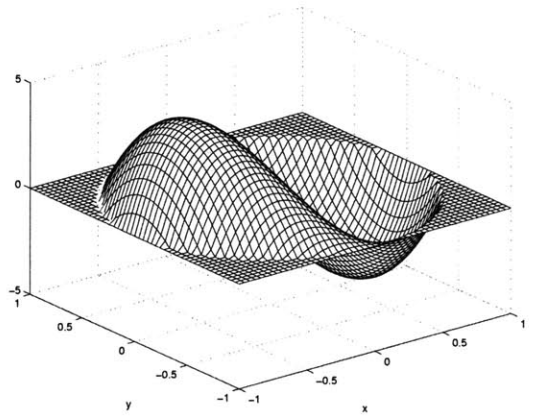

(b)

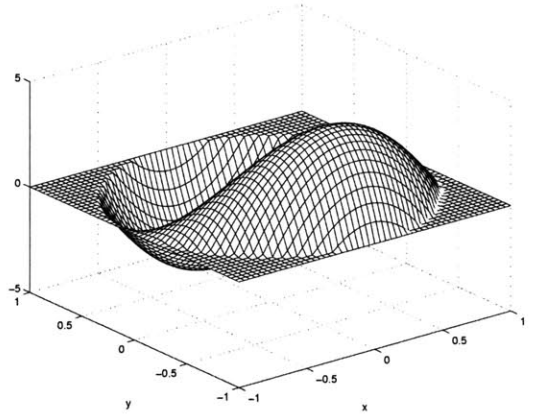

(c)

Figure 2-3: Weighting function and derivatives in two-dimensional domain: (a) Weighting function $W_I(\mathbf{x})$, (b) $\frac{\partial W_I(\mathbf{x})}{\partial x}$, (c) $\frac{\partial W_I(\mathbf{x})}{\partial y}$.

and $\Im$ is an index set. Here h represents the radius of the sphere. We consider the case $\underset{m=0,1,2}{\text{span}} \{p_m(\mathbf{x})\} = \{1, x, y\}$ for two-dimensional problems.

The global approximation spaces V_h are generated by multiplying the partition of unity function with the local basis polynomial functions,

$$V_h(\mathbf{x}) = \sum_{I=1}^{N} \rho_I V_I^h. \tag{2.26}$$

Therefore, any function $v_h \in V_h$ can be expressed as follows:

$$v_h = \sum_{I=1}^{N} \sum_{m \in \Im} h_{Im}(\mathbf{x}) \alpha_{Im}, \tag{2.27}$$

where $h_{Im}(\mathbf{x}) = \rho_I(\mathbf{x}) p_m(\mathbf{x})$, and we call $h_{Im}(\mathbf{x})$ the shape function associated with the m^{th} degree of freedom of node I, and α_{Im} its coefficient.

2.3.2 Displacement-based formulation

We consider the following variational form [2].

$$\Pi = \frac{1}{2} \int_\Omega \boldsymbol{\epsilon}^T(\mathbf{u}) \boldsymbol{\tau}(\mathbf{u}) d\Omega - \Re = \frac{1}{2} \int_\Omega \boldsymbol{\epsilon}^T(\mathbf{u}) \mathbf{C} \boldsymbol{\epsilon}(\mathbf{u}) d\Omega - \Re \tag{2.28}$$

The term $\Re$ is for the externally applied body forces, surface traction and prescribed displacements,

$$\Re = \int_\Omega \mathbf{u}^T \mathbf{f}^B d\Omega + \int_{\Gamma_f} \mathbf{u}^T \mathbf{f}^s d\Gamma + \int_{\Gamma_u} \mathbf{f}^{uT} (\mathbf{u} - \mathbf{u}^s) d\Gamma, \tag{2.29}$$

where strain vector $\boldsymbol{\epsilon}^T = [\epsilon_{xx} \ \epsilon_{yy} \ \gamma_{xy}]$ and stress vector $\boldsymbol{\tau}^T = [\tau_{xx} \ \tau_{yy} \ \tau_{xy}]$, $\mathbf{u}$ is the displacement field, $\mathbf{f}^s$ is the prescribed surface traction vector on the boundary Γ_f, $\mathbf{u}^s$ is the prescribed displacement vector on the boundary Γ_u, and $\mathbf{f}^B$ is the body force vector. The strain-displacement relation is

$$\boldsymbol{\epsilon} = \partial_\epsilon \mathbf{u} \qquad \text{in } \Omega, \tag{2.30}$$

where

$$\partial_\epsilon = \begin{bmatrix} \partial/\partial x & 0 \\ 0 & \partial/\partial y \\ \partial/\partial y & \partial/\partial x \end{bmatrix}. \tag{2.31}$$

By the linear elastic constitutive law,

$$\boldsymbol{\tau} = \mathbf{C}\boldsymbol{\epsilon}(\mathbf{u}) \quad \text{in } \Omega \tag{2.32}$$

In Equation (2.29) $\mathbf{f}^u$ is the traction vector on the Dirichlet boundary, and $\mathbf{f}^s$ is the prescribed traction vector on the Neumann boundary Γ_f,

$$\mathbf{u}^{sT} = [u^s(x,y) \ v^s(x,y)], \tag{2.33}$$

$$\mathbf{f}^u = \mathbf{N}\mathbf{C}\boldsymbol{\epsilon}(\mathbf{u}) \quad \text{on } \Gamma_u, \tag{2.34}$$

$$\mathbf{f}^{sT} = [\mathbf{N}\,\boldsymbol{\tau}]^T = [f_x^s(x,y) \ f_y^s(x,y)] \quad \text{on } \Gamma_f. \tag{2.35}$$

The matrix $\mathbf{N}$ has the direction cosine components of a unit normal outward vector as

$$\mathbf{N} = \begin{bmatrix} n_x & 0 & n_y \\ 0 & n_y & n_x \end{bmatrix}, \tag{2.36}$$

and the elasticity matrix is

$$\mathbf{C} = \begin{bmatrix} c_{11} & c_{12} & 0 \\ c_{12} & c_{11} & 0 \\ 0 & 0 & c_{33}, \end{bmatrix}. \tag{2.37}$$

where for the plane stress condition the components of elasticity matrix are

$$c_{11} = \frac{E}{1-\nu^2}, \quad c_{12} = \frac{E\nu}{1-\nu^2}, \quad c_{33} = \frac{E}{2(1+\nu)}, \tag{2.38}$$

and for plane strain conditions,

$$c_{11} = \frac{E(1-\nu)}{(1+\nu)(1-2\nu)}, \quad c_{12} = \frac{E\nu}{(1+\nu)(1-2\nu)}, \quad c_{33} = \frac{E}{2(1+\nu)}, \tag{2.39}$$

where E and ν are the Young's modulus and Poisson's ratio of the elastic material respectively.

By invoking the stationary of Π in Equation (2.28) we obtain

$$\begin{aligned} &\int_\Omega \boldsymbol{\epsilon}^T(\mathbf{v})\mathbf{C}\boldsymbol{\epsilon}(\mathbf{u})d\Omega - \int_{\Gamma_u} \left[\boldsymbol{\epsilon}^T(\mathbf{v})\mathbf{C}\mathbf{N}^T\mathbf{u} + \mathbf{v}^T\mathbf{N}\mathbf{C}\boldsymbol{\epsilon}(\mathbf{u})\right] d\Gamma \\ &= \int_\Omega \mathbf{v}^T\mathbf{f}^B d\Omega + \int_{\Gamma_f} \mathbf{v}^T\mathbf{f}^s d\Gamma - \int_{\Gamma_u} \boldsymbol{\epsilon}^T(\mathbf{v})\mathbf{C}\mathbf{N}^T\mathbf{u}^s d\Gamma \qquad \forall \mathbf{v} \in H^1(\Omega), \end{aligned} \tag{2.40}$$

where $H^1(\Omega)$ is the first order Hilbert space. The approximation for the displacement field can be written as

$$u(x,y) = \sum_{J=1}^{N} \sum_{n \in \Im} \mathbf{H}_{Jn}(x,y)\boldsymbol{\alpha}_{Jn} = \mathbf{H}(x,y)\mathbf{U}, \tag{2.41}$$

where $\mathbf{U} = [\boldsymbol{\alpha}_{10} \quad \boldsymbol{\alpha}_{11} \quad \boldsymbol{\alpha}_{12} \quad \ldots]^T$ and $\boldsymbol{\alpha}_{Jn} = [u^{Jn} \quad v^{Jn}]$. The displacement interpolation matrix and strain-displacement matrix are respectively:

$$\mathbf{H}_{Jn}(x,y) = \begin{bmatrix} h_{Jn}(x,y) & 0 \\ 0 & h_{Jn}(x,y) \end{bmatrix}, \; \mathbf{B}_{Jn}(x,y) = \begin{bmatrix} h_{Jn_{,x}}(x,y) & 0 \\ 0 & h_{Jn_{,y}}(x,y) \\ h_{Jn_{,y}}(x,y) & h_{Jn_{,x}}(x,y) \end{bmatrix}. \tag{2.42}$$

where $h_{Jn}(\mathbf{x}) = \rho_J(\mathbf{x})p_n$ and derivatives in $x-$ and $y-$ coordinates are

$$h_{Jn_{,x}}(\mathbf{x}) = \rho_{J_{,x}}(\mathbf{x})p_n + \rho_J(\mathbf{x})p_{n_{,x}}, \tag{2.43}$$

$$h_{Jn_{,y}}(\mathbf{x}) = \rho_{J_{,y}}(\mathbf{x})p_n + \rho_J(\mathbf{x})p_{n_{,y}}. \tag{2.44}$$

Finally, the discretized equation for node I, degree of freedom m, is

$$\sum_{J=1}^{N} \sum_{n \in \Im} \mathbf{K}_{ImJn}\boldsymbol{\alpha}_{Jn} = \mathbf{f}_{Im} + \hat{\mathbf{f}}_{Im}, \tag{2.45}$$

where

$$\mathbf{K}_{ImJn} = \int_{\Omega_I} \mathbf{B}_{Im}^T \mathbf{C} \mathbf{B}_{Jn} d\Omega, \tag{2.46}$$

$$\mathbf{f}_{Im} = \int_{\Omega_I} \mathbf{H}_{Im} \mathbf{f}^B d\Omega \tag{2.47}$$

and $\hat{\mathbf{f}}_{Im}$ imposes the displacement/force boundary conditions [18]; for example, for a sphere intersecting Γ_f, we use

$$\hat{\mathbf{f}}_{Im} = \int_{\Gamma_f \bigcap B_I} \mathbf{H}_{Im} \mathbf{f}^s d\Gamma. \tag{2.48}$$

In equations (2.46) and (2.47), Ω_I is the intersection of Ω and $B_I(\mathbf{x}_I, R_I)$. On the other hand, if the sphere corresponding to node I has nonzero intersection on the Dirichlet boundary, then we have

$$\hat{\mathbf{f}}_{Im} = \sum_{J=1}^{N} \sum_{n \in \Im} \mathbf{KU}_{ImJn} \boldsymbol{\alpha}_{Jn} - \mathbf{fU}_{Im}, \tag{2.49}$$

where

$$\mathbf{KU}_{ImJn} = \int_{\Gamma_u \bigcap B_I} \mathbf{H}_{Im} \mathbf{N} \mathbf{C} \mathbf{B}_{Jn} d\Gamma + \int_{\Gamma_u \bigcap B_I} \mathbf{B}_{Im}^T \mathbf{C} \mathbf{N}^T \mathbf{H}_{Jn} d\Gamma \tag{2.50}$$

and

$$\mathbf{fU}_{Im} = \int_{\Gamma_u \bigcap B_I} \mathbf{B}_{Im}^T \mathbf{C} \mathbf{N}^T \mathbf{u}^s d\Gamma. \tag{2.51}$$

It should be noted that the matrix $\mathbf{KU}$ is symmetric.

2.4 Formulation for boundary conditions

In meshless techniques, the imposition of the Dirichlet boundary condition and Neumann boundary condition incurs more complicated schemes than in the finite element method. However, still it is possible to handle this problems efficiently with a simplified scheme. In this section we discuss how to impose the boundary conditions derived in Equation (2.10) and (2.11) in the method of finite spheres considering the efficiency.

In the finite element method, because of the Kronecker delta property of the shape functions, only the nodes which correspond to the Neumann boundary condition are considered for the calculation of the consistent load, but in the method of finite sphere the shape functions do not have the Kronecker delta property, so we need to consider all the nodes which have non-zero intersection with the Neumann boundary. For example, let $B_I \bigcap \Gamma_f$ be the intersection of the sphere I and the boundary Γ_f, then the union of $B_I \bigcap \Gamma_f$ and $B_I \bigcap \Gamma_u$ becomes Γ. By substituting Equation (2.18) into Equation (2.10), we obtain

$$\hat{f}_{Im} = \int_{B_I \bigcap \Gamma_f} h_{Im}(\mathbf{x}) f^s(\mathbf{x}) dS. \tag{2.52}$$

Similarly, for the Dirichlet boundary condition in the finite element method only the nodes located on the Dirichlet boundary are considered to impose the Dirichlet boundary condition. Hence homogeneous boundary conditions can be exactly simulated.

In the method of finite spheres, the shape functions do not have the Kronecker delta characteristic, so we introduce a technique to handle the Dirichlet boundary condition as in the finite element method [13]. The nodes on the boundary are distributed to have the same

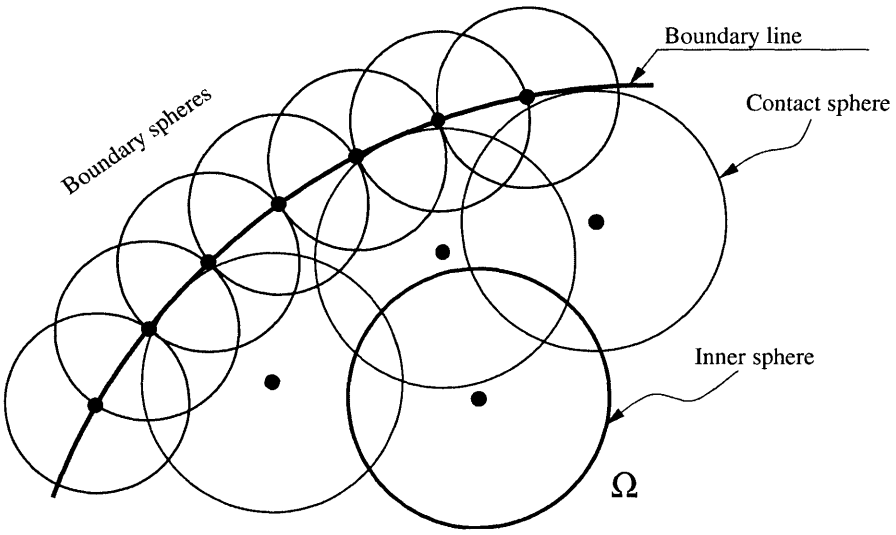

Figure 2-4: Node distribution for the imposition of Dirichlet boundary condition. Nodes are arranged along the boundary to circumvent to have complicated integration domain.

radii, and the inner spheres near the boundary do not have non-zero intersections with the boundary as shown in the Figure 3-1.

This ensures that the shape functions along the boundary have the Kronecker delta characteristic. Recalling the definition of $\rho_I(\mathbf{x})$ in Equation (2.25),

$$\rho_I(\mathbf{x}) = \frac{W_I(\mathbf{x})}{\sum_{J=1}^{N} W_J(\mathbf{x})} = \frac{W_I(\mathbf{x})}{W_I(\mathbf{x})} = 1 \quad \text{at node } I. \tag{2.53}$$

To implement this technique, for the homogeneous boundary condition, we can eliminate the rows and columns corresponding to the nodes which have non-zero intersection with the Dirichlet boundary.

Chapter 3

Numerical Integration Theory

The calculation of integrals is an essential task in the finite element method. Also, in meshless techniques, this task is most important. Tremendous amount of textbooks and articles are available [19–23]. However, the new concept of method of finite spheres demands some innovative ideas specific for our scheme. The term *quadrature* is frequently used for one-dimensional integration and term *cubature* is common for multi-dimensional integrations. This chapter gives a comprehensive and concise summary of numerical integrations including some fundamental theorems.

In the one-, two-dimensional cases, the required matrix integrations in the finite element and finite sphere calculations have been written as [2]

$$\int f(x)dx = \sum_i c_i f(x_i) + R_n \tag{3.1}$$

$$\int f(x,y)dxdy = \sum_{i,j} c_{ij} f(x_i, y_i) + R_n \tag{3.2}$$

where the summation extends over all i and j, the c_i, c_{ij} are weighting factors, the $f(x)$,

$f(x,y)$ are integrand functions in the matrices, and R_n are error remainders which are not evaluated in practice. Hence we use

$$\int f(x)dx = \sum_i c_i f(x_i) \tag{3.3}$$

$$\int f(x,y)dxdy = \sum_{i,j} c_{ij} f(x_i, y_i) \tag{3.4}$$

3.1 One dimensional numerical integration

Numerical methods for discretizing and approximating integrals are based on the use of appropriate integration formulas [24]. For the one dimensional integration problem, we have the integration rule

$$Q(f) = Q_n(f) \approx \sum_{i=1}^{n} c_i f(x_i), \tag{3.5}$$

where c_i is the integration weight, Q is a numerical integration operator, and x_i is the integration abscissa. Most quadrature formulas are obtained by approximating the integrand function f in the given integration interval by a polynomial. In this case, we have a set of polynomials and each describes the integrand in a section. In another way, the quadrature formulae can be constructed by approximating the function f using a piecewise polynomial.

In many cases, quadrature formulas have symmetries as

$$x_i = a + \left\{b - x_{n-(i-1)}\right\}, \qquad c_i = c_{n-(i-1)}, \quad i = 1, 2, \ldots, (n+1)/2. \tag{3.6}$$

when the abscissas $x_1, \ldots, x_n$ of all practical quadrature formulas Q_n are located in the interval of integration $[a, b]$. The construction of the quadrature rules includes two main tasks. One is that the abscissas and weights should be chosen to satisfy the accuracy requirement. The second is that the integration values should converge to the exact integration values as more integration points are used. The midpoint rule commonly called *Riemann's integration* is

$$R_n(f) \approx \int_a^b f(x)dx \approx \sum_{i=1}^{n}(x_{i+1} - x_i)f(\xi), \tag{3.7}$$

where $R(\cdot)$ is the Riemann sum operator, $\xi \in [x_i, x_{i+1}]$ for $i = 1, 2, \ldots, n$. It is possible to approximate any Riemann integrable function with any arbitrary accuracy requirement ε. The simplest way to obtain a converging sequence of the Riemann integration is to divide the interval $[a, b]$ into n subdivisions of equal length as:

$$x_i = a + ih, \quad i = 0, 1, \ldots, n; \quad h = \frac{b-a}{n}. \tag{3.8}$$

The choice for ξ_i can be either left-side end point or right-side end point of the subdivisions. We use notations R_n^{left} for left-side end point rule and R_n^{right} for right-side end point rule. When we set the exact analytical integration value of the function f as $I(f)$, the discretization error $\{R_n(f) - I(f)\}$ can be estimated in terms of modulus of the continuity.

Theorem 3.1.1 *If $f \in C[a, b]$ and the integration domain is divided into n equal segments having $(n + 1)$ abscissas from x_0 to x_n, then*

$$|R_n^{right}(f) - I(f)| \leq (b - a)\, \chi\left(f; \frac{b-a}{n}\right) \tag{3.9}$$

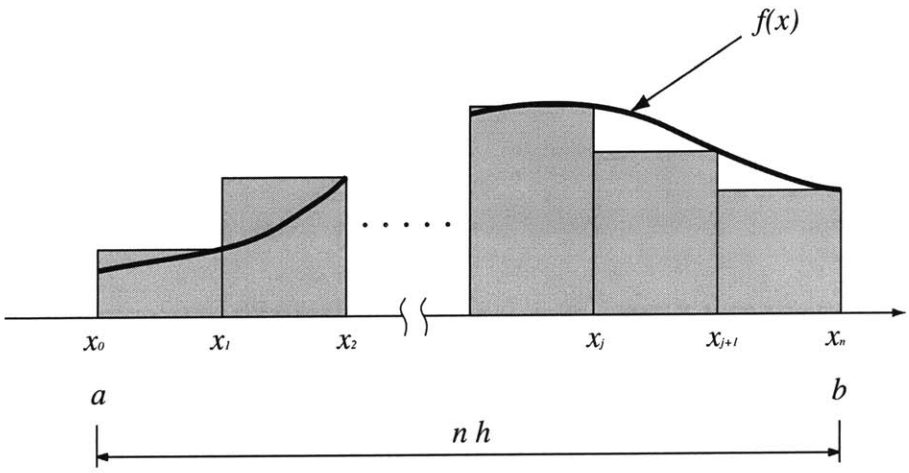

Figure 3-1: Riemann integration: right-side point rule is applied to integrate a function $f(x)$ from a to b.

Proof When we apply right-side end point rule of Riemann integration for a given function f as shown in Figure, the error of the integration is

$$|R_n^{right}(f) - I(f)| = \left| h \sum_{i=1}^{n} f(x_i) - \int_a^b f(x)dx \right|$$

Since $hf(x_i) = \int_{x_{i-1}}^{x_i} f(x_i)dx$ for the right-side point rule, we have

$$\begin{aligned}
\left| h \sum_{i=1}^{n} f(x_i) - \int_a^b f(x)dx \right| &= \left| \sum_{i=1}^{n} \int_{x_{i-1}}^{x_i} [f(x_i) - f(x)]dx \right| \\
&\leq \sum_{i=1}^{n} \int_{x_{i-1}}^{x_i} |f(x_i) - f(x)|dx \\
&\leq \sum_{i=1}^{n} \int_{x_{i-1}}^{x_i} \chi(f;h)dx \\
&\leq nh\,\chi(f;h) \\
&= (b-a)\,\chi(f;\frac{b-a}{n}). \qquad \square
\end{aligned}$$

where

$$\chi(f;\delta) = \sup\{|f(x_1) - f(x_2)| : x_1, x_2 \in [a,b],\ |x_1 - x_2| \leq \delta\} \tag{3.10}$$

is weight or density function and $h\left(=\frac{b-a}{n}\right)$ is length of each segment. This is rough error estimation, and if differentiability and continuity are provided, then this error can be measured more precisely.

3.1.1 Construction of quadrature rule by approximation

More effective quadrature rules can be obtained by approximating the function f by a model function $g \in \mathcal{M}$ where $\mathcal{M}$ is *space of approximation functions* and we consider the approximation value $I(g)$ as the integration value for the exact integration of $I(f)$. This assumption is valid only when the model function can be described as a simple function, so the polynomial functions are most promising model functions. If the model function g satisfies

$$||g - f||_{L^\infty} \leq \frac{\epsilon}{b-a} \tag{3.11}$$

where ε is error requirement, then the error bound becomes

$$\begin{aligned} |I(g) - I(f)| &= \left| \int_a^b g(x)dx - \int_a^b f(x)dx \right| \\ &\leq \int_a^b |g(x) - f(x)|dx \\ &\leq (b-a)||g - f||_{L^\infty} \\ &\leq \varepsilon. \end{aligned} \tag{3.12}$$

Hence, the approximation function which is close enough to the function f with respect to the L_∞ norm can be considered as the model function for the integration.

In many practical integration, it is quite often required to integrate some functions which are the product of $w(x)$ and $f(x)$, where $w(x)$ is a weighting function which is known in analytical forms. Now we denote this kind of integration as *product integration*, and the notation is

$$I_w(g) = I(wg). \tag{3.13}$$

By this scheme, the resulting rule is called *product rule*. This integration is valid only when the weighting functions can be expressed analytically, regardless of the space of model functions. The condition estimate for the validity of product integration can be derived as:

$$\begin{aligned} |I_w(g) - I_w(f)| &= \left| \int w(x)g(x)dx - \int w(x)f(x)dx \right| \\ &\leq \int |w(x)|\,|g(x) - f(x)|dx \\ &\leq ||w||_{L^1}||g - f||_{L^\infty} = \varepsilon. \end{aligned} \tag{3.14}$$

where $||\cdot||_{L_1}$ is L_1 norm. When the weighting function is absolutely integrable in the range of $[a, b]$, then the error is proportional to the $||g(x) - f(x)||_{L^\infty}$. Product rule is good for various weighting functions.

3.1.2 Approximation with polynomials

The polynomial for approximation of a function which has abscissas $x_1, x_2, \ldots, x_n$ can be determined uniquely in terms of *Lagrange polynomials* as:

$$P_{n-1}(x) = \sum_{i=1}^{n} f(x_i)\phi_{n-1,i}(x), \quad P_{n-1} \in \mathbb{P}_{n-1} \tag{3.15}$$

$$\phi_{n-1,i}(x) = \prod_{\substack{j=1 \\ j \neq i}}^{n} \frac{x - x_j}{x_i - x_j}, \qquad i = 1, 2, \ldots, n. \tag{3.16}$$

By use of Equation (3.15), the integration of the product of $w(x)$ and P_{n-1} is

$$I_w(P_{n-1}) = \int_a^b w(x)P_{n-1}(x)dx = \sum_{i=1}^{n} f(x_i) \left\{ \int_a^b w(x)\phi_{n-1,i}(x)dx \right\}, \tag{3.17}$$

so the weighting coefficients can be derived as

$$c_i = \int_a^b w(x)\phi_{n-1,x}(x)dx. \tag{3.18}$$

Theorem 3.1.2 *For $f \in C^n[a,b]$ the approximation error $\varepsilon_{n-1}(f)$ satisfies*

$$\varepsilon_{n-1}(f) \leq \frac{||f^{(n)}||_{L^\infty}}{n!} ||w_n||_{L^\infty} \tag{3.19}$$

where the polynomial w_n is

$$w_n(x) = (x - x_1)(x - x_2)(x - x_3) \cdots (x - x_n). \tag{3.20}$$

In another way, this quadrature rule can be extended to a *compound rule*, which is obtained by approximating the function f by piecewise polynomial functions to each subdivision in the whole integration domain. The error in a simple quadrature can be reduced by increasing the order of polynomials, but the error of the compound rules is decreased by refining the subdivision of the integration domain with fixed order of polynomials.

Definition 3.1.1 *The* degree of accuracy *of a quadrature rule is D if*

$$\begin{aligned} &Q_n(x^k) = I_w(x^k), \quad k = 0, 1, \ldots, D, \\ &Q_n(x^{D+1}) \neq I_w(x^{D+1}), \end{aligned} \tag{3.21}$$

in other words, Q_n gives the exact value for the polynomial of order less or equal to D.

It is possible to make a relation between degree of accuracy and L_∞ norm in the approximation function. Therefore, we have the following theorem,

Theorem 3.1.3 *Any quadrature rule with a degree of accuracy $D \geq 0$ satisfies the inequality*

$$|Q_n(f) - I_w(f)| \leq \left(||w||_{L^1} + \sum_{i=1}^{n} |c_i| \right) \varepsilon_D(f), \tag{3.22}$$

where $\varepsilon_D \approx \inf\{||P_D - f||_{L^\infty}\}$, P_D is the best approximation function in $\mathbb{P}_D$, and if all weights of Q_n are greater or equal to zero, then

$$|Q_n(f) - I_w(f)| \leq [||w||_{L^1} + I(w)]\, \varepsilon_D(f). \tag{3.23}$$

If the coefficients of a sequence of the quadrature rule are all positive or zero, then the error bound means the integration value converges as the number of integration points

increases such that

$$Q_n(f) \longrightarrow I_w(f) \quad as \quad n \longrightarrow \infty \quad \forall f \in C[a,b], \tag{3.24}$$

provided the integration domain is compact.

Theorem 3.1.4 *Let Q_n denotes a sequence of the quadrature rules with respect to an admissible weight function w on the compact domain, and assume all coefficients of Q_n to be nonnegative, then the convergence of the quadrature rules for all $f \in C[a,b]$ means the convergence of Q_n for all Riemann integrable functions $f \in \mathcal{R}[a,b]$, where $\mathcal{R}$ denotes a set of Riemann integrable functions [21].*

3.1.3 Orthogonal polynomials

For the w which is admissible weight function, the inner product can be defined on the set of all polynomial $\mathbb{P}$ in one dimensional case with the inner product

$$(P,Q)_w \approx I_w(PQ) = \int_a^b w(x)P(x)Q(x)dx \quad \forall P,Q \in \mathbb{P}, \tag{3.25}$$

where $(\cdot,\cdot)$ means a inner product in the space of $\mathbb{P}$ and we can define

$$||P||_w = [(P,P)_w]^{1/2}. \tag{3.26}$$

These polynomials are orthogonal if

$$I_w(PQ) = \int_a^b w(x)P(x)Q(x)dx = 0, \tag{3.27}$$

when the P and Q are not same. The sets of the orthogonal polynomials can be obtained for any weight function by applying the *Gram-Schmidt orthogonalization* procedure to the set of monomials [20].

3.1.4 Gauss formulas

So far, we considered use of equally spaced sampling points. In the finite element methods, we use Gauss quadrature rule to improve the accuracy. The basic idea of Gauss quadrature is optimization of the positions of the sampling points [2]. The assumption is that

$$\int_a^b f(x)dx = \sum_{i=1}^{n} c_i f(x_i) + R_n \tag{3.28}$$

where c_i are weighting factors, x_i are sampling abscissas and R_n is the remainder. We use an interpolating polynomial $\psi(x)$ of the form

$$\psi(x) = \sum_{i=1}^{n} f_i l_i(x) \tag{3.29}$$

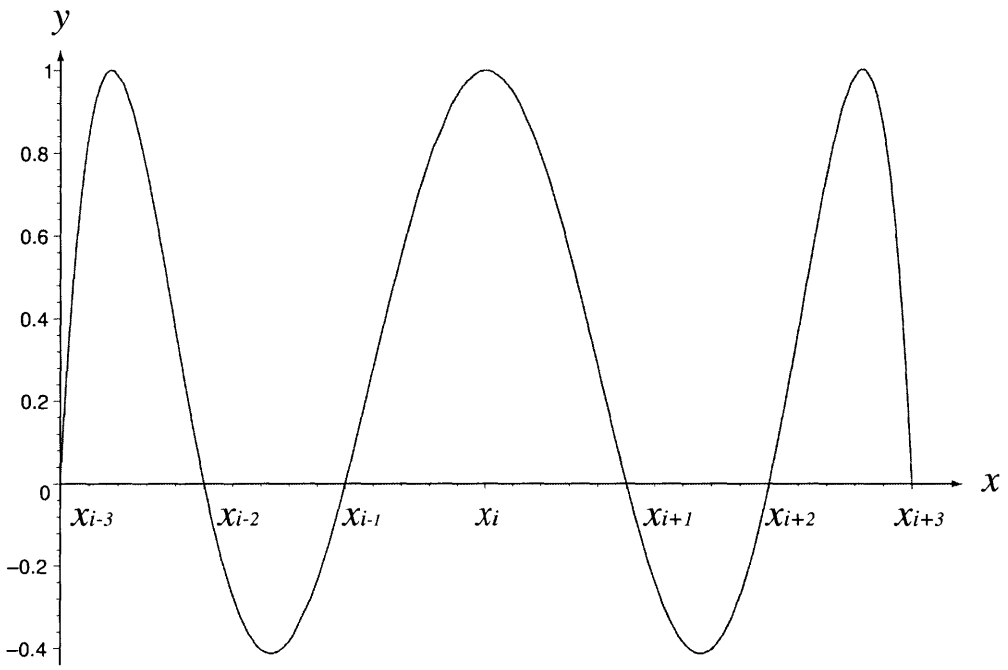

Figure 3-2: Lagrangian polynomials.

where n sampling points are still unknowns and fundamental polynomials of *Lagrangian interpolation* $l_i(x)$ can be expressed as

$$l_i(x) = \frac{(x-x_0)(x-x_1)\cdots(x-x_{i-1})(x-x_{i+1})\cdots(x-x_n)}{(x_i-x_0)(x_i-x_1)\cdots(x_i-x_{i-1})(x_i-x_{i+1})\cdots(x_i-x_n)}. \tag{3.30}$$

as shown in Figure 3-2, where

$$l_i(x_j) = \delta_{ij} \tag{3.31}$$

where δ_{ij} is the Kronecker delta; i.e., $\delta_{ij} = 1$ for $i = j$, and $\delta_{ij} = 0$ for $i \neq j$.

For the determination of the locations x_i, we define a function $P(x)$,

$$P(x) = (x-x_1)(x-x_2)(x-x_3)\cdots(x-x_n) \tag{3.32}$$

which is a polynomial $\in \mathbb{P}_n$. We note that $P(x_i) = 0$. Therefore, it can be written

$$f(x) = \psi(x) + P(x)(\beta_0 + \beta_1 x + \beta_2 x^2 + \beta_3 x^3 + \cdots) \tag{3.33}$$

By integrating $f(x)$, we obtain

$$\int_a^b f(x)dx = \sum_{j=1}^{n} f_j \left[\int_a^b l_j(x)dx\right] + \sum_{j=0}^{\infty} \beta_j \left[\int_a^b x^j P(x)dx\right] \tag{3.34}$$

where it should be noted that the first term on the right, functions of order $(n-1)$ and lower are integrated, and in the second integral the functions that are integrated are of order n and higher. The unknowns $x_j, j = 1, 2, \ldots, n$ can be determined by the conditions

$$\int_a^b P(x)x^j dx = 0, \qquad k = 1, 2, \ldots, n-1. \tag{3.35}$$

Since the polynomial $\psi(x)$ passes through n sampling points of $f(x)$, and $P(x)$ vanishes to zero at these points, the condition in Equation (3.35) mean that the required integration of $\int_a^b f(x)dx$ is approximated by integrating a polynomial of order $(2n-1)$ instead of $f(x)$. In summary Gauss quadrature requires n unequally spaced sampling points and integrate exactly a polynomial of order at most $(2n-1)$.

To determine the sampling points and the integration factor, we consider the *natural interval* from -1 to 1 and apply any isoparametric mapping for any interval. When x_i is a sampling point and c_i is the weighting factor, the corresponding sampling point and weight

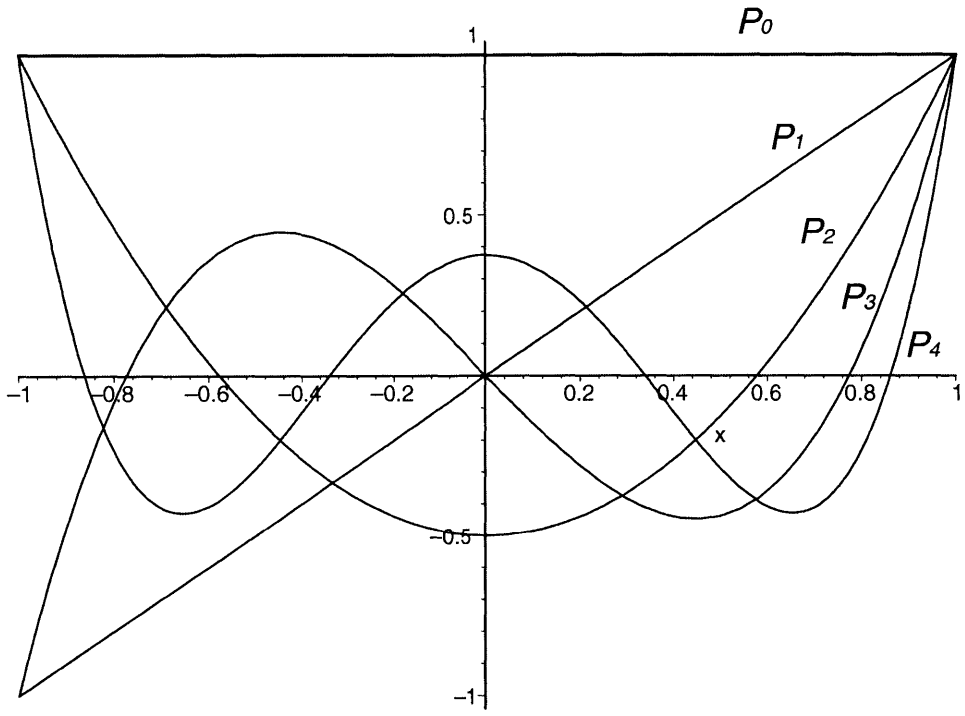

Figure 3-3: Legendre polynomials [1].

in the integration from a to b are

$$\frac{a+b}{2} + \frac{b-a}{2}x_i \quad \text{and} \quad \frac{b-a}{2}c_i \tag{3.36}$$

respectively. To calculate the integration factors, we substitute for $f(x)$ in Equation (3.28) the interpolating polynomial $\psi(x)$ of Equation (3.29) and perform the integration. It should be noted that the sampling points have been determined and the polynomial $\psi(x)$ is known, then

$$c_i = \int_{-1}^{1} l_j(x)dx; \qquad j = 1, 2, \ldots, n. \tag{3.37}$$

Abscissas	Gauss formulas
Legendre polynomials	Gauss-Legendre formula
Laguerre polynomials	Gauss-Laguerre formula
Jacobi polynomials	Gauss-Jacobi formula

Table 3.1: Quadrature abscissas and corresponding Gauss formula.

The Gauss-Legendre integration procedure is widely used for the numerical integrations, but also there are more schemes available for the numerical integrations.

3.1.5 Compound quadrature rule

The compound quadrature rule comes from integrating piecewise polynomials. This also can be derived by subdividing the interval into subintervals and by applying a simple interpolation formula to each subinterval. For the simplicity, it is assumed that the interval $[a, b]$ is divided into n sections which have $n + 1$ equally distributed nodes as:

$$a = x_0 < x_1 < x_2 \cdots < x_n = b, \quad x_i = a + i \left[\frac{b-a}{n} \right], \quad i = 0, 1, 2, \ldots, n. \tag{3.38}$$

A specific k- point quadrature rule (Q_k) is applied to each of the subintervals, and the quadrature formular is denoted by $n \times Q_k$. Setting the interval is from -1 to 1 by isoparametric transformation, the integration value is

$$Q_k(f) = \sum_{i=1}^{k} c_i f(\beta_i) \approx \int_{-1}^{1} f(x)dx, \quad \beta_i \in [-1, 1], \quad i = 1, 2, \ldots, k. \tag{3.39}$$

For a subinterval the integration is

$$\int_{x_{j-1}}^{x_j} f(x)dx = \frac{b-a}{2n}\sum_{i=1}^{k} c_i f(x_{ij}), \quad j = 1, 2, \ldots, n, \tag{3.40}$$

where

$$x_{ij} = x_{j-1} + \frac{b-a}{2n}(1+\beta_i), \quad i = 1, 2, \ldots, k, \quad j = 1, 2, \ldots, n. \tag{3.41}$$

Therefore, the compound rule for the interval $[a, b]$ can be written as:

$$(n \times Q_k)(f) = \sum_{j=1}^{n} \frac{b-a}{2n}\sum_{i=1}^{k} c_i f(x_{ij}). \tag{3.42}$$

The convergence of compound quadrature rules can be derived for all Riemann integrable functions.

Theorem 3.1.5 *Let Q_k be an k-point quadrature rule with degree of accuracy $D \geq 0$, then*

$$(n \times Q_k)(f) \longrightarrow I(f) \quad as \quad n \longrightarrow \infty. \tag{3.43}$$

Proof From the Equation (3.42), we have

$$(n \times Q_k)f = \sum_{j=1}^{n} c_i \frac{b-a}{2n}\sum_{i=1}^{k} f(x_{ij}), \tag{3.44}$$

where the term of $\frac{b-a}{n}\sum_{j=1}^{n} f(x_{ij})$ is a simple Riemann integration, so the Equation (3.44) converges to $I(f)$ as $n \to \infty$ $\square$.

Theorem 3.1.6 *Let Q_k be an k-point quadrature rule, then the error for the integrands*

$f \in C^P[a,b]$ *is*

$$Q_k(f) - \int_a^b f(x)dx = C(b-a)^{p+1} f^{(p)}(\xi), \quad \xi \in [a,b], \tag{3.45}$$

where C *is a constant value independent of* a, b, *and* f. *The error term* $E_{n\times Q_k}(f) = (n \times Q_k)f - \int_a^b f(x)dx$ *can be expressed as:*

$$\lim_{n\to\infty} n^p E_{n\times Q_k}(f) = C(b-a)^p \left[f^{(p-1)}(b) - f^{(p-1)}(a)\right]. \tag{3.46}$$

Hence, the convergence of $E_{k\times Q_n}$ *is at least of order* p.

Proof The error term $E_{n\times Q_k}(f)$ is the sum of the integration errors in Q_k on each subinterval. Therefore,

$$E_{n\times Q_k}(f) = \sum_{j=1}^{n} C\left(\frac{b-a}{n}\right)^{p+1} f^{(p)}(\xi_j), \qquad \xi_j \in [x_{j-1}, x_j] \tag{3.47}$$

$$= C\left(\frac{b-a}{n}\right)^p \left(\frac{b-a}{n}\right) \sum_{j=1}^{n} f^{(p)}(\xi_j) \tag{3.48}$$

$$= C\left(\frac{b-a}{n}\right)^p \int_a^b f^{(p)}(x)dx \tag{3.49}$$

$$= C\left(\frac{b-a}{n}\right)^p \left[f^{(p-1)}(b) - f^{(p-1)}(a)\right] \tag{3.50}$$

3.2 Multi-dimensional numerical integration

The construction of the quadrature rule for the multivariate and multi-dimensional domain is much more difficult than those in 1-D space. On the other hand, in the rectangular inte-

gration domain, we can apply the one dimensional integration formulas in each direction. In the same way of analytical integration, the integration can be achieved by keeping the variables corresponding to the other integrals constant. Hence, for the two-dimensional integration, we have [2]

$$\begin{aligned}\int_{-1}^{+1}\int_{-1}^{+1} f(r,s)drds &= \sum_i c_i \int_{-1}^{+1} f(r_i,s)ds \\ &= \sum_{i,j} c_i c_j f(r_i,s_j)\end{aligned} \tag{3.51}$$

where c_i and c_j are the integration weights for one-dimensional integration. This can be extended even for the three-dimensional integral.

3.2.1 Construction of formula by approximation

The approximation can be obtained by approximating the integrand using a model function $g \in \mathcal{M}$ and taking the definite integral $I_w(g)$ as an approximation of $I_w(f)$. By the equation of

$$|I_w(g) - I_w(f)| \leq ||w||_{L_1} ||g - f||_{L^\infty}, \tag{3.52}$$

which is independent of the dimension N, and if the approximation function g satisfies

$$||g - f||_{L^\infty} \leq \frac{\varepsilon}{||w||_{L_1}}, \tag{3.53}$$

then the error bound is

$$|I_w(g) - I_w(f)| \leq \varepsilon. \tag{3.54}$$

Hence, this approximation can be used even for constructing the cubature rules.

The approximation rule is practical only if the definite integral of the model function over the given integration domain can be described explicitly with a relatively simple function. Considering this fact polynomials are attractive since they are easily integrated.

The Taylor series expansion around *zero* for the multi-dimensional domain is as

$$\begin{aligned} f(\mathbf{x}) =& f(\mathbf{0}) + \sum_{i_1=1}^{N} \frac{\partial f}{\partial x_{i_1}}(\mathbf{0}) x_{i_1} + \sum_{i_1=1,i_2=1}^{N} \frac{1}{2!} \frac{\partial^2 f}{\partial x_{i_1} \partial x_{i_2}}(\mathbf{0}) x_{i_1} x_{i_2} + \cdots \\ & \cdots + \sum_{i_1,\ldots,i_d=1}^{N} \frac{1}{d!} \frac{\partial^d f}{\partial x_{i_1}, \ldots, \partial x_{i_d}}(\mathbf{0}) x_{i_1} x_{i_2} \cdots x_{i_d} + \cdots, \end{aligned} \tag{3.55}$$

and this Taylor series converges for all $\mathbf{x} \in C_N$. For the integration of the multivariate integration, the following approximation can be written

$$\begin{aligned} \int_{C_N} f(\mathbf{x}) dx = & \int_{C_N} f(\mathbf{0}) dx + \sum_{i_1=1}^{N} \frac{\partial f}{\partial x_{i_1}}(\mathbf{0}) \int_{C_N} x_{i_1} d\mathbf{x} \\ & + \sum_{i_1=1,i_2=1}^{N} \frac{1}{2!} \frac{\partial^2 f}{\partial x_{i_1} \partial x_{i_2}}(\mathbf{0}) \int_{C_N} x_{i_1} x_{i_2} d\mathbf{x} + \cdots \\ & \cdots + \frac{1}{d!} \sum_{i_1,\ldots,i_d=1}^{N} \frac{\partial^d f}{\partial x_{i_1}, \ldots, \partial x_{i_d}}(\mathbf{0}) \int_{C_N} x_{i_1} x_{i_2} \cdots x_{i_d} d\mathbf{x}. \end{aligned} \tag{3.56}$$

The monomials $x_{i_1} \cdots x_{i_l}$ can be integrated analytically over *unit cube* C_N. For the function f which has maximum order bigger than d, the remainder term for $\mathbf{x} \in C_N$ is given by higher order terms.

3.2.2 Construction of formula by transformation

Numerical computation of integrals can be facilitated by transforming the given integration equation using the isoparametric transformation. Many cubature rules are specified to particular integration regions. Let $\psi : \overline{B} \rightarrow B$ is defined as a continuously differentiable one-to-one mapping. When the Jacobian matrix J of Ψ is not singular on $\bar{B}$, i.e.,

$$\exists \quad \det J(\overline{\mathbf{x}}) \neq 0, \quad \forall \overline{\mathbf{x}} \in \bar{B}. \tag{3.57}$$

Then, the multidimensional transformation rule results in

$$\int_B w(\mathbf{x}) f(\mathbf{x}) d\mathbf{x} = \int_{\bar{B}} \overline{w}(\overline{\mathbf{x}}) |\det J(\overline{\mathbf{x}})| \overline{f}(\overline{\mathbf{x}}) d\overline{\mathbf{x}} \tag{3.58}$$

where

$$\overline{w}(\overline{\mathbf{x}}) = w(\psi(\mathbf{x})) \quad \text{and} \quad \overline{f}(\overline{\mathbf{x}}) = f(\psi(\mathbf{x})) \tag{3.59}$$

The transformation ψ converts the cubature formula

$$\int_{\bar{B}} \overline{w}(\overline{\mathbf{x}}) |\det J(\overline{\mathbf{x}})| \overline{f}(\overline{\mathbf{x}}) d\overline{\mathbf{x}} = \sum_{i=1}^{n} \overline{c}_i |\det J(\overline{\mathbf{x}}_i)| \overline{f}(\overline{\mathbf{x}}_i) + \overline{E}(|\det J| \overline{f}) \tag{3.60}$$

to the cubature formula

$$\int_B w(\mathbf{x}) f(\mathbf{x}) dx = \sum_{i=1}^{n} c_i f(\mathbf{x}_i) + E(f) \tag{3.61}$$

with abscissas and weights given by

$$\mathbf{x}_i = \psi(\overline{\mathbf{x}}_i), \quad \overline{c}_i = \overline{c}_i |\det J(\overline{\mathbf{x}}_i)|, \quad i = 1, 2, \ldots, n, \tag{3.62}$$

The iteration of integrals can also be used to facilitate the construction of multidimensional integration formulas. For affine transformation we have $\mathbf{x}_i = \mathbf{A}\overline{\mathbf{x}}_i + \mathbf{B}$, $c_i = |\det \mathbf{A}|\overline{c}_i$, and $E(f) = |\det \mathbf{A}| E(f)$

Definition 3.2.1 (Cartesian product rule) *Suppose the integration region of B is the Cartesian product $B = B_1 \times B_2$ of the regions B_1, B_2, and let*

$$Q_{n_1}^{(1)}(f_1) = \sum_{i_1=1}^{n_1} c_{i_1}^{(1)} f_1(\mathbf{x}_{i_1}^{(1)}) \quad \textit{and} \quad Q_{n_2}^{(2)} f_2 = \sum_{i_2=1}^{n_2} c_{i_2}^{(2)} f_2(\mathbf{x}_{i_2}^{(2)}) \tag{3.63}$$

denote integration formulas for the two integrals

$$I_1(f_1) = \int_{B_1} f_1(\mathbf{x}^{(1)}) d\mathbf{x}^{(1)} \quad \textit{and} \quad I_2(f_2) = \int_{B_2} f_2(\mathbf{x}^{(2)}) d\mathbf{x}^{(2)}, \tag{3.64}$$

respectively, Then, the Cartesian product rule for the integrand over B is defined by

$$(Q_{n_1}^{(1)} \times Q_{n_2}^{(2)}) f = \sum_{i_1=1}^{n_1} \sum_{i_2=1}^{n_2} c_{i_1}^{(1)} c_{i_2}^{(2)} f(\mathbf{x}_{i_1}^{(1)}, \mathbf{x}_{i_2}^{(2)}). \tag{3.65}$$

Theorem 3.2.1 *If $Q_{n_1}^{(1)}$ integrates f_1 exactly over B_1 and $Q_{n_2}^{(2)}$ integrates f_2 exactly over B_2, then the Cartesian product rule integrates the product exactly over the region $B = B_1 \times B_2$.*

The Cartesian product rule can be generalized as:

Definition 3.2.2 (K-Fold Cartesian Product Rules) *Suppose the integration region B is the Cartesian product of $K \geq 2$ region $B_1, B_2, \ldots, B_K$, i.e., $B = B_1 \times \cdots \times B_K$. Let*

$$Q_{n_k}^{(k)}(f_k) = \sum_{i_k=1}^{n_k} c_{i_k}^{(k)} f_k(\mathbf{x}_{i_k}^{(k)}), \quad k = 1, 2, \ldots, K, \tag{3.66}$$

denote integration formulas for the integrals

$$I_k(f_k) = \int_{B_k} f_k(\mathbf{x}^{(k)}) d\mathbf{x}^{(k)}, \quad k = 1, 2, \ldots, K, \tag{3.67}$$

respectively. Then the K-fold Cartesian product rule $Q_{n_1}^{(1)} \times \cdots \times Q_{n_K}^{(K)}$ for the integral over B is defined by

$$\left(Q_{n_1}^{(1)} \times \cdots \times Q_{n_k}^{(K)}\right) f = \sum_{i_1=1}^{n_1} \cdots \sum_{i_K=1}^{n_K} c_{i_1}^{(1)} \cdots c_{i_K}^{(K)} f(\mathbf{x}_{i_1}^{(1)}, \ldots, \mathbf{x}_{i_K}^{(K)}) \tag{3.68}$$

3.2.3 Generalized Cartesian Product Rules

Cartesian product rules can be generalized for integration regions which are not Cartesian products. Assume that the integral $I(f)$ can be iterated,

$$I(f) = \int_B f(\mathbf{x}) d\mathbf{x} = \int_{B_1} \int_{B_2(\mathbf{x}^{(1)})} f(\mathbf{x}^{(1)}, \mathbf{x}^{(2)}) d\mathbf{x}^{(2)} d\mathbf{x}^{(1)} = \int_{B_1} f_1(\mathbf{x}^{(1)}) d\mathbf{x}^{(1)}, \tag{3.69}$$

where

$$f_1(x^{(1)}) = \int_{B_2(\mathbf{x}^{(1)})} f(\mathbf{x}^{(1)}, \mathbf{x}^{(2)}) d\mathbf{x}^{(2)} \tag{3.70}$$

3.2.4 Multivariate polynomial approximations

Since polynomials can be integrated easily in closed form over most standard regions, polynomials appear to be suitable model functions for use in the approximation approach to cubature formula construction. Multivariate monomials $x_1^{d_1} x_2^{d_2} \cdots x_N^{d_N}$ where $d_1, d_2, \cdots d_N$ is the order of each variable in vector form:

$$\mathbf{x}^{\mathbf{d}}, \quad \mathbf{d}^T = [d_1, \ldots, d_N] \in \mathbb{N}_0, \tag{3.71}$$

where $\mathbb{N}_0$ is the union of set of all positive integer and 0. The set of all $N-$variate monomials $\{\mathbf{x}^{\mathbf{d}} : \mathbf{d} \in \mathbb{N}_0^N\}$ is a basis for $\mathbb{P}^N$ which is the set of all mutivariate polynomials of N variables; i.e., any polynomial $P \in \mathbb{P}^N$ can be uniquely represented as a linear combination of a finite number of monomials,

$$P = \sum_{j=1}^{J} c_j \mathbf{x}_j^{\mathbf{d}}, \quad c_j \neq 0, j = 1, 2, \ldots, J. \tag{3.72}$$

Definition 3.2.3 (Degree of Multivariate Polynomials) *The degree of a monomial* $\mathbf{x}^{\mathbf{d}}$ *is defined by*

$$deg(\mathbf{x}^{\mathbf{d}}) = ||\mathbf{d}||_{L^1} = d_1 + d_2 + d_3 + \cdots + d_N. \tag{3.73}$$

The degree of a general polynomial

$$P = \sum_{j=1}^{J} c_j \mathbf{x}^{\mathbf{d}_j} \tag{3.74}$$

is defined as

$$\deg(P) = max\{||\mathbf{d}_1||_{L_1}, ||\mathbf{d}_2||_{L_1}, ||\mathbf{d}_3||_{L_1}, \ldots, ||\mathbf{d}_J||_{L_1}\}. \tag{3.75}$$

The set of all $N-$variate polynomials of maximum degree d, denoted by

$$\mathbb{P}_N^d = \{P \in \mathbb{P}^N : degP \leq d\}, \tag{3.76}$$

is a linear subspace of $\mathbb{P}^N$.

Theorem 3.2.2 *The dimension of $\mathbb{P}_d^N$ is given by*

$$dim\,(d, N) = dim\mathbb{P}_d^N = \binom{N+d}{N} = \frac{(N+d)!}{d!\,N!}. \tag{3.77}$$

We need to consider the problem of choosing suitable *n-dimensional spaces of polynomial model functions* $\mathcal{M}_{\mathbb{P}}$ when given numbers $n \in \mathbb{N}$ is considered. Generally speaking, $\mathcal{M}_{\mathbb{P}}$ should be chosen such that all f in a relevant class of functions can be approximated by polynomials $P \in \mathcal{M}_{\mathbb{P}}$ with an accuracy as high as possible.

For dimension $N \geq 2$, the problem of choosing suitable n-dimensional spaces of polynomial model functions $\mathcal{M}_{\mathbb{P}}$ is more intricate. Taylor series expansion suggests that a high approximation accuracy can be attained even for small degree d, provided the integrand is sufficiently smooth. For both reasons, the choice of the polynomial spaces $\mathbb{P}_d^N, d = 0, 1, \ldots,$ as spaces of model functions appears to be highly reasonable for multiple dimensions too.

3.2.5 Polynomial Interpolation

Generally, the interpolation problem can be solved for arbitrarily prescribed function values, $f(\mathbf{x}_1), f(\mathbf{x}_2), \cdots, f(\mathbf{x}_n)$ if and only if the linear functionals

$$\{l_1, l_2, \ldots, l_n : \mathcal{M}_{\mathbb{P}} \to \mathbb{R}\} \tag{3.78}$$

can be defined as

$$l_i(P) = P(x_i), i = 1, 2, \ldots, n, \tag{3.79}$$

and those functionals are linearly independent over $\mathcal{M}_{\mathbb{P}}$. If this independence requirement is met, the interpolation polynomial is unique if and only if $\dim(\mathcal{M}_{\mathbb{P}}) = n$.

For example, in one dimensional case, the space of model functions $(\mathcal{M}_{\mathbb{P}}) = \mathbb{P}_{n-1}$ for any $n \in N$, where n is number of data points. The approximation function $P \in \mathbb{P}_{n-1}$ can be determined uniquely when

$$P(x_i) = f(x_i), \quad i = 1, 2, \ldots, n. \tag{3.80}$$

For the two-dimensional or higher dimensional problem, model function exists only when n is particular value such that

$$n \in \{\dim(d, N) : d \in \mathbb{N}_0\}. \tag{3.81}$$

Many researchers developed a method to construct $n-$dimensional polynomial spaces properly for $n-$data independent over $\mathcal{M}_{\mathbb{P}}(\mathbf{x}_1, \mathbf{x}_2, \mathbf{x}_n)$.

Definition 3.2.4 (Degree of Accuracy) *The degree of accuracy of an N-dimensional cubature formula Q_n is D if*

$$Q_n(\mathbf{x}^d) = I_w(\mathbf{x}^d) \quad \forall \mathbf{d} \in \mathbb{N}_0^N \quad \textit{with} \quad ||\mathbf{d}||_{L_1} \leq D, \tag{3.82}$$

$$Q_n(\mathbf{x}^d) \neq I_w(\mathbf{x}^d) \quad \textit{for at least one} \quad \mathbf{d} \in \mathbb{N}_0^N \quad \textit{with} \quad ||\mathbf{d}||_{L_1} = D + 1. \tag{3.83}$$

3.2.6 Interpolatory formulas

For n given distinct abscissas $\mathbf{x}_1, \ldots, \mathbf{x}_n$, the requirement that Q_n must integrate all polynomials of maximum degree $d = D$ exactly means that the weighs $c_1, \ldots, c_n$ of the cubature formula

$$Q_n(f) = \sum_{i=1}^{n} c_i f(\mathbf{x}_i) \tag{3.84}$$

to be constructed are chosen in such a way that

$$Q_n(P_d) = I_w(P_d) \quad \forall\, P_d \in \mathbb{P}_d^N. \tag{3.85}$$

Since $\mathbb{P}_d^N$ is a vector space of dimension $\dim(d, N)$ and both operators I_w and Q_n are linear functionals over $\mathbb{P}_d^N$, it is sufficient that the equality in Equation (3.85) hold for just one particular basis $\{b_1, \ldots, b_{\dim(d,N)}\}$ of $\mathbb{P}_d^N$:

$$Q_n(b_j) = I_w(b_j), j = 1, 2, \ldots, \dim(d, N). \tag{3.86}$$

The Equation (3.86) is called *moment equation.*

Definition 3.2.5 (Interpolatory Integration Formula) *An integration formula Q_n with the abscissas is said to be* interpolatory *if its weights are the unique solution of the equations:*

$$\sum_{i=1}^{N} c_i b_j(\mathbf{x}_i) = I_w(b_j), \quad j = 1, 2, \ldots, \dim(d, N). \tag{3.87}$$

The condition in Definition 3.2.5 that the weights $c_1, \ldots, c_n$ must be the unique solution of the moment equations can be explained as follows. By considering the linear functionals

$$l_1, l_2, \ldots, l_n : \mathbb{P}_d^N \to \mathbb{R} \tag{3.88}$$

we have

$$\sum_{i=1}^{n} c_i l_i(b_j) = I_w(b_j), \quad j = 1, 2, \ldots, \dim(d, N). \tag{3.89}$$

This equations can be solved if and only if the linear functional I_w over $\mathbb{P}_d^N$ is a linear combination of the linear functionals $l_1, l_2, \ldots, l_n$, Then the weights $c_1, c_2, \ldots, c_n$ of Q_n are chosen as the coefficients of a linear combination

$$I_w = \sum_{i=1}^{n} c_i l_i. \tag{3.90}$$

This means that the weights are uniquely determined by the abscissas if and only if the functionals are linearly independent. Therefore, all the cubature formulas derived from moment equations are interpolatory.

Theorem 3.2.3 *Any interpolatory cubature formula Q_n with degree of accuracy $D \geq 0$*

satisfies the inequality

$$|Q_n(f) - I_w(f)| \leq \left(||w||_1 + \sum_{i=1}^{n} |c_i| \right) \inf\{||P_D - f||_\infty : P_D \in \mathbb{P}_D^N\}. \tag{3.91}$$

If all weights are nonnegative, then

$$|Q_n(f) - I_w(f)| \leq (||w||_{L_1} + I(w)) \inf\{||P_D - f||_\infty : P_D \in \mathbb{P}_D^N\}. \tag{3.92}$$

This implies that the error in cubature formulas is expected to decrease as the degree of accuracy increases.

Chapter 4

Numerical Integration and Auto Sphere Generation for MFS

Most meshless techniques require heavy cost for the numerical integration to calculate the stiffness values. In the method of finite spheres, the shape functions are rational functions and the integration domains are spheres or spherical sectors. Furthermore, the spheres overlap with other spheres making "lens" shape regions. Therefore, we need to classify the integration rules for each case. Exact integration of the stiffness values is not achievable since the integration rules can, at most, guarantee polynomial accuracy. Hence, we focus on the development of more efficient integration schemes.

There are two kinds of possibilities for the improvements of numerical integration schemes. First, we can simplify and transform the integral equations into simpler shapes [25]. The integral equations have highly complicated forms since we have derivatives of rational functions and multiplications of those terms. We can transform some of the terms into lower dimensional integrations by the divergence theorem. Secondly, it is possible to

suggest more efficient sampling scheme for more efficiency. In this chapter, we present the improved analytical equations and suggest more efficient integration rules in the two-dimensional domains.

4.1 Improvement of analytical equations for numerical integration for inner sphere

The expressions to be integrated are rather complex and, clearly, transformations into simpler forms are most desirable. For example, we consider the simple plate model which has square shape and fixed displacement boundary at left side as shown in Figure 4-1, and the node arrangement is assumed to be uniformly distributed as illustrated in Figure 4-2. For the stiffness value we need to integrate the integrands and the integrands are highly complicated distributions as in Figure 4-3.

In equation (2.46) we explicitly have:

$$\mathbf{K}_{ImJn} = \int_{\Omega_I} \begin{bmatrix} K_{11} & K_{12} \\ K_{21} & K_{22} \end{bmatrix} d\Omega, \tag{4.1}$$

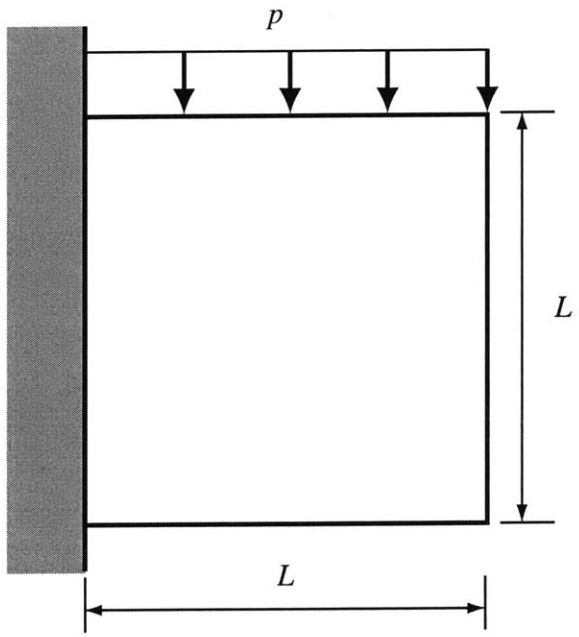

Figure 4-1: Pressure load is applied on cantilever plate.

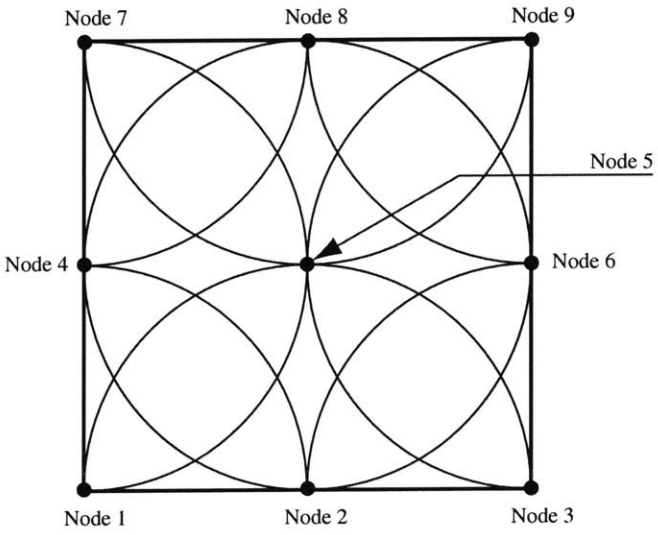

Figure 4-2: Finite sphere node arrangement. The nodes are uniformly distributed.

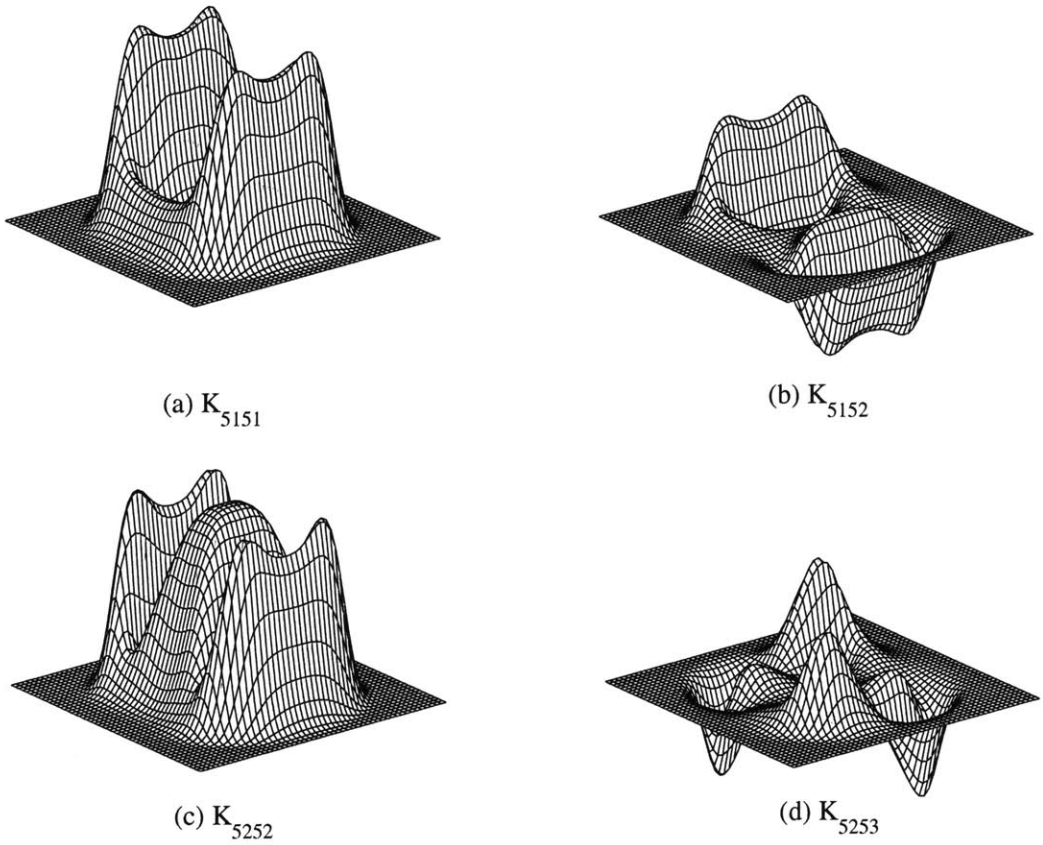

(a) K_{5151} (b) K_{5152}

(c) K_{5252} (d) K_{5253}

Figure 4-3: Integrand distributions in Equation (4.1).

where the elements of the stiffness matrix are

$$K_{11} = C_{11} h_{Im,x} h_{Jn,x} + C_{33} h_{Im,y} h_{Jn,y} \tag{4.2}$$

$$K_{12} = C_{12} h_{Im,x} h_{Jn,y} + C_{33} h_{Im,y} h_{Jn,x} \tag{4.3}$$

$$K_{21} = C_{12} h_{Im,y} h_{Jn,x} + C_{33} h_{Im,x} h_{Jn,y} \tag{4.4}$$

$$K_{22} = C_{11} h_{Im,y} h_{Jn,y} + C_{33} h_{Im,x} h_{Jn,x}. \tag{4.5}$$

Considering the case J equal to I, we have

$$K_{11} = C_{11} h_{Im,x} h_{In,x} + C_{33} h_{Im,y} h_{In,y} \tag{4.6}$$

$$K_{12} = C_{12} h_{Im,x} h_{In,y} + C_{33} h_{Im,y} h_{In,x} \tag{4.7}$$

$$K_{21} = C_{12} h_{Im,y} h_{In,x} + C_{33} h_{Im,x} h_{In,y} \tag{4.8}$$

$$K_{22} = C_{11} h_{Im,y} h_{In,y} + C_{33} h_{Im,x} h_{In,x}. \tag{4.9}$$

We can rewrite the equations of the stiffness terms into forms more effective for the numerical integration. The integration of the first term in Equation (4.6) is

$$\int_{\Omega_I} h_{Im,x} h_{In,x} d\Omega = \int_{\Omega_I} \rho_{I,x}^2 p_m p_n + \rho_I \rho_{I,x} (p_{m,x} p_n + p_m p_{n,x}) + \rho_I^2 p_{m,x} p_{n,x} d\Omega. \tag{4.10}$$

The term $\int_{\Omega_I} \rho_I \rho_{I,x} p_{m,x} p_n d\Omega$ can be rewritten to obtain

$$\int_{\Omega_I} \rho_I \rho_{I,x} p_{m,x} p_n d\Omega = \int_{\Omega_I} \{\rho_I^2 p_{m,x} p_n\}_{,x} d\Omega - \int_{\Omega_I} \rho_I \left(\rho_I p_{m,x} p_n\right)_{,x} d\Omega, \tag{4.11}$$

Then we can differentiate the second term in the right hand side,

$$\int_{\Omega_I} \rho_I \rho_{I,x} p_{m,x} p_n d\Omega = \int_{\Omega_I} \{\rho_I^2 p_{m,x} p_n\}_{,x} d\Omega - \int_{\Omega_I} \rho_I \rho_{I,x} p_{m,x} p_n d\Omega - \int_{\Omega_I} \rho_I^2 p_{m,x} p_{n,x} d\Omega, \tag{4.12}$$

It is possible to add $\int_{\Omega_I} \rho_I \rho_{I,x} p_{m,x} p_n d\Omega$ on both side to simplify and we have

$$2 \times \int_{\Omega_I} \rho_I \rho_{I,x} p_{m,x} p_n d\Omega = \int_{\Omega_I} \{\rho_I^2 p_{m,x} p_n\}_{,x} d\Omega - \int_{\Omega_I} \rho_I^2 p_{m,x} p_{n,x} d\Omega, \tag{4.13}$$

and by the divergence theorem,

$$\int_{\Omega_I} \rho_I \rho_{I,x} p_{m,x} p_n d\Omega = \frac{1}{2} \int_{\Gamma \cap B_I} \rho_I^2 p_{m,x} p_n n_x dS - \frac{1}{2} \int_{\Omega_I} \rho_I^2 p_{m,x} p_{n,x} d\Omega. \tag{4.14}$$

Similarly, the third term can be transformed

$$\int_{\Omega_I} \rho_I \rho_{I,x} p_m p_{n,x} d\Omega = \frac{1}{2} \int_{\Gamma \cap B_I} \rho_I^2 p_m p_{n,x} n_x dS - \frac{1}{2} \int_{\Omega_I} \rho_I^2 p_{m,x} p_{n,x} d\Omega. \tag{4.15}$$

By substituting Equations (4.14) and (4.15) into Equation (4.10), we obtain

$$\int_{\Omega_I} h_{Im,x} h_{In,x} d\Omega = \int_{\Omega_I} \rho_{I,x}^2 p_m p_n d\Omega + \frac{1}{2} \int_{\Gamma \cap B_I} \rho_I^2 p_{m,x} p_n n_x dS + \frac{1}{2} \int_{\Gamma \cap B_I} \rho_I^2 p_m p_{n,x} n_x dS. \tag{4.16}$$

It should be noted that the term of $\int_{\Omega_I} \rho_I^2 p_{m,x} p_{n,x} d\Omega$ in the Equation (4.12) is cancelled out by summing Equations (4.14) and (4.15).

For the other terms in Equations (4.6) to (4.9) we have

$$\begin{aligned}\int_{\Omega_I} h_{Im,x} h_{In,y} d\Omega = &\int_{\Omega_I} \rho_{I,x}\rho_{I,y} p_m p_n d\Omega + \frac{1}{2}\int_{\Gamma\cap B_I} \rho_I^2 p_m p_{n,y} n_x dS \\ &+ \frac{1}{2}\int_{\Gamma\cap B_I} \rho_I^2 p_{m,x} p_n n_y dS\end{aligned} \tag{4.17}$$

$$\begin{aligned}\int_{\Omega_I} h_{Im,y} h_{In,x} d\Omega = &\int_{\Omega_I} \rho_{I,x}\rho_{I,y} p_m p_n d\Omega + \frac{1}{2}\int_{\Gamma\cap B_I} \rho_I^2 p_m p_{n,x} n_y dS \\ &+ \frac{1}{2}\int_{\Gamma\cap B_I} \rho_I^2 p_{m,y} p_n n_x dS\end{aligned} \tag{4.18}$$

$$\begin{aligned}\int_{\Omega_I} h_{Im,y} h_{In,y} d\Omega = &\int_{\Omega_I} \rho_{I,y}^2 p_m p_n d\Omega + \frac{1}{2}\int_{\Gamma\cap B_I} \rho_I^2 p_{m,y} p_n n_y dS \\ &+ \frac{1}{2}\int_{\Gamma\cap B_I} \rho_I^2 p_m p_{n,y} n_y dS.\end{aligned} \tag{4.19}$$

We substitute the terms from Equations (4.16) to (4.19) into Equations (4.6) to (4.9), and obtain the integral equations for the stiffness terms

$$\begin{aligned}\int_{\Omega_I} K_{11} d\Omega = &C_{11}\left\{\int_{\Omega_I} \rho_{I,x}^2 p_m p_n d\Omega + \frac{1}{2}\int_{\Gamma\cap B_I} \rho_I^2 Q_1 dS + \frac{1}{2}\int_{\Gamma\cap B_I} \rho_I^2 Q_2 dS\right\} \\ &+ C_{33}\left\{\int_{\Omega_I} \rho_{I,y}^2 p_m p_n d\Omega + \frac{1}{2}\int_{\Gamma\cap B_I} \rho_I^2 Q_3 dS + \frac{1}{2}\int_{\Gamma\cap B_I} \rho_I^2 Q_4 dS\right\},\end{aligned} \tag{4.20}$$

$$\begin{aligned}\int_{\Omega_I} K_{12} d\Omega = &C_{12}\left\{\int_{\Omega_I} \rho_{I,x}\rho_{I,y} p_m p_n d\Omega + \frac{1}{2}\int_{\Gamma\cap B_I} \rho_I^2 Q_5 dS + \frac{1}{2}\int_{\Gamma\cap B_I} \rho_I^2 Q_6 dS\right\} \\ &+ C_{33}\left\{\int_{\Omega_I} \rho_{I,x}\rho_{I,y} p_m p_n d\Omega + \frac{1}{2}\int_{\Gamma\cap B_I} \rho_I^2 Q_7 dS + \frac{1}{2}\int_{\Gamma\cap B_I} \rho_I^2 Q_8 dS\right\},\end{aligned} \tag{4.21}$$

$$\int_{\Omega_I} K_{21} d\Omega = C_{12} \left\{ \int_{\Omega_I} \rho_{I,x} \rho_{I,y} p_m p_n d\Omega + \frac{1}{2} \int_{\Gamma \cap B_I} \rho_I^2 Q_7 dS + \frac{1}{2} \int_{\Gamma \cap B_I} \rho_I^2 Q_8 dS \right\}$$
$$+ C_{33} \left\{ \int_{\Omega_I} \rho_{I,x} \rho_{I,y} p_m p_n d\Omega + \frac{1}{2} \int_{\Gamma \cap B_I} \rho_I^2 Q_5 dS + \frac{1}{2} \int_{\Gamma \cap B_I} \rho_I^2 Q_6 dS \right\}, \tag{4.22}$$

$$\int_{\Omega_I} K_{22} d\Omega = C_{11} \left\{ \int_{\Omega_I} \rho_{I,y}^2 p_m p_n d\Omega + \frac{1}{2} \int_{\Gamma \cap B_I} \rho_I^2 Q_3 dS + \frac{1}{2} \int_{\Gamma \cap B_I} \rho_I^2 Q_4 dS \right\}$$
$$+ C_{33} \left\{ \int_{\Omega_I} \rho_{I,x}^2 p_m p_n d\Omega + \frac{1}{2} \int_{\Gamma \cap B_I} \rho_I^2 Q_1 dS + \frac{1}{2} \int_{\Gamma \cap B_I} \rho_I^2 Q_2 dS \right\}, \tag{4.23}$$

where

$$\begin{aligned} Q_1(x,y) &= p_{m,x} p_n n_x, & Q_2(x,y) &= p_m p_{n,x} n_x, \\ Q_3(x,y) &= p_{m,y} p_n n_y, & Q_4(x,y) &= p_m p_{n,y} n_y, \\ Q_5(x,y) &= p_m p_{n,y} n_x, & Q_6(x,y) &= p_{m,x} p_n n_y, \\ Q_7(x,y) &= p_m p_{n,x} n_y, & Q_8(x,y) &= p_{m,y} p_n n_x. \end{aligned} \tag{4.24}$$

When $\Gamma \bigcap B_I = 0$ the Equations (4.20) to (4.23) change into much simplified form since there is not line integration terms. For example, we consider the sphere I and sphere J in Figure 4-4. For the sphere J we do not need to calculate the line integrals. It is required to calculate the first terms of the equations from (4.20) to (4.23).Therefore, the use of the improved equations is clearly much more effective than the use of the original expressions for the numerical integrations.

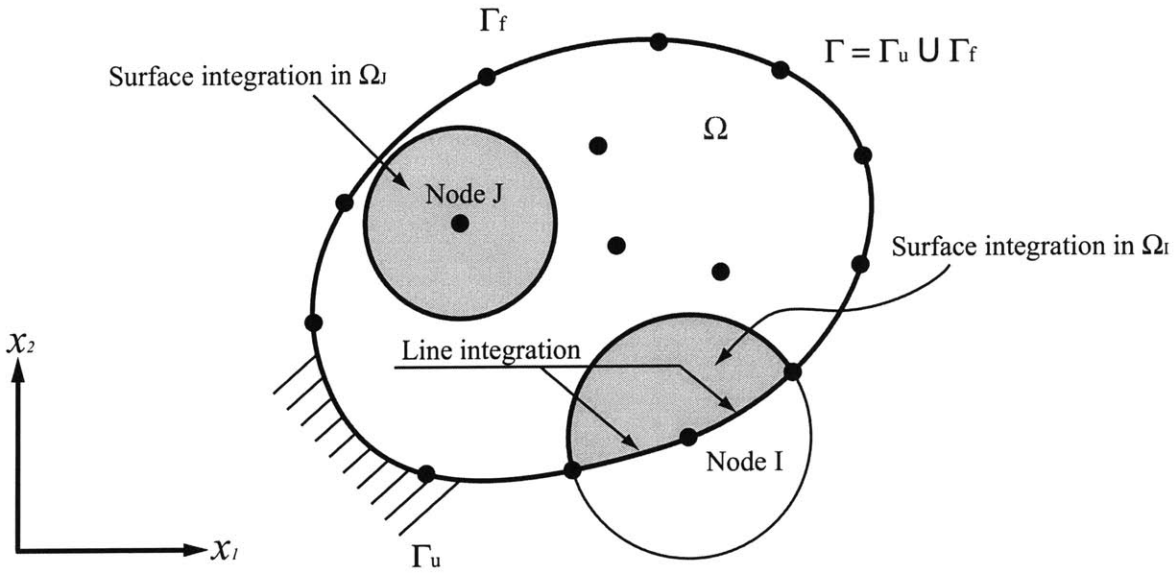

Figure 4-4: Numerical integration scheme with newly derived equations from (4.20) to (4.23).

4.2 Improvement of analytical equations for numerical integration for lens shape

In the lens integration, J is not same as I, and we have the integrands

$$\begin{aligned}\int_{\Omega_{IJ}} h_{Im_{,x}} h_{Jn_{,x}} d\Omega &= \int_{\Omega_{IJ}} \left(\rho_{I_{,x}} p_m + \rho_I p_{m_{,x}}\right)\left(\rho_{J_{,x}} p_n + \rho_J p_{n_{,x}}\right) d\Omega \\ &= \int_{\Omega_{IJ}} \rho_{I_{,x}}\rho_{J_{,x}} p_m p_n + \rho_{I_{,x}}\rho_J p_m p_{n_{,x}} + \rho_I \rho_{J_{,x}} p_{m_{,x}} p_n + \rho_I \rho_J p_{m_{,x}} p_{n_{,x}} d\Omega,\end{aligned} \tag{4.25}$$

where Ω_{IJ} is the intersection of Ω_I and Ω_J.

Similarly, we have

$$\begin{aligned}\int_{\Omega_{IJ}} h_{Im,y} h_{Jn,y} &= \int_{\Omega_{IJ}} \left(\rho_{I,y} p_m + \rho_I p_{m,y}\right)\left(\rho_{J,y} p_n + \rho_J p_{n,y}\right) d\Omega \\ &= \int_{\Omega_{IJ}} \rho_{I,y}\rho_{J,y} p_m p_n + \rho_{I,y}\rho_J p_m p_{n,y} + \rho_I \rho_{J,y} p_{m,y} p_n + \rho_I \rho_J p_{m,y} p_{n,y} d\Omega,\end{aligned} \tag{4.26}$$

$$\begin{aligned}\int_{\Omega_{IJ}} h_{Im,x} h_{Jn,y} &= \int_{\Omega_{IJ}} \left(\rho_{I,x} p_m + \rho_I p_{m,x}\right)\left(\rho_{J,y} p_n + \rho_J p_{n,y}\right) d\Omega \\ &= \int_{\Omega_{IJ}} \rho_{I,x}\rho_{J,y} p_m p_n + \rho_{I,x}\rho_J p_m p_{n,y} + \rho_I \rho_{J,y} p_{m,x} p_n + \rho_I \rho_J p_{m,x} p_{n,y} d\Omega,\end{aligned} \tag{4.27}$$

$$\begin{aligned}\int_{\Omega_{IJ}} h_{Im,y} h_{Jn,x} &= \int_{\Omega_{IJ}} \left(\rho_{I,y} p_m + \rho_I p_{m,y}\right)\left(\rho_{J,x} p_n + \rho_J p_{n,x}\right) d\Omega \\ &= \int_{\Omega_{IJ}} \rho_{I,y}\rho_{J,x} p_m p_n + \rho_{I,y}\rho_J p_m p_{n,x} + \rho_I \rho_{J,x} p_{m,y} p_n + \rho_I \rho_J p_{m,y} p_{n,x} d\Omega.\end{aligned} \tag{4.28}$$

The integration of the term $\rho_{I,x}\rho_J p_m p_{n,x}$ in the Equation (4.25) can be expressed as

$$\int_{\Omega_{IJ}} \rho_{I,x}\rho_J p_m p_{n,x} d\Omega = \int_{\Omega_{IJ}} \left\{\rho_I \left(\rho_J p_m p_{n,x}\right)\right\}_{,x} d\Omega - \int_{\Omega_{IJ}} \rho_I \left(\rho_J p_m p_{n,x}\right)_{,x} d\Omega. \tag{4.29}$$

By the divergence theorem, we have

$$\begin{aligned}\int_{\Omega_{IJ}} \rho_{I,x}\rho_J p_m p_{n,x} d\Omega = &\int_{\Gamma_{IJ}} \rho_I \rho_J p_m p_{n,x} n_x dS - \int_{\Omega_{IJ}} \rho_I \rho_{J,x} p_m p_{n,x} d\Omega \\ &- \int_{\Omega_{IJ}} \rho_I \rho_J p_{m,x} p_{n,x} d\Omega,\end{aligned} \tag{4.30}$$

where Γ_{IJ} is boundary of lens-shape integration domain.

Finally, we have the equation of

$$\begin{aligned}\int_{\Omega_{IJ}} \rho_{I,x}\rho_J p_m p_{n,x} d\Omega + \int_{\Omega_{IJ}} \rho_I \rho_{J,x} p_m p_{n,x} d\Omega = \\ \int_{\Gamma_{IJ}} \rho_I \rho_J p_m p_{n,x} n_x dS - \int_{\Omega_{IJ}} \rho_I \rho_J p_{m,x} p_{n,x} d\Omega.\end{aligned} \tag{4.31}$$

When p_m is same as p_n, we can substitute the Equation (4.31) into Equation (4.25), then the equation can be simplified as

$$\int_{\Omega_{IJ}} h_{Im,x} h_{In,x} d\Omega = \int_{\Omega_{IJ}} \rho_{I,x} \rho_{J,x} p_m p_n + \int_{\Gamma_{IJ}} \rho_I \rho_J p_m p_{n,x} n_x dS. \tag{4.32}$$

In the similar way, we can obtain the relation for Equation (4.26)

$$\begin{aligned} \int_{\Omega_{IJ}} \rho_{I,y} \rho_J p_m p_{n,y} d\Omega + \int_{\Omega_{IJ}} \rho_I \rho_{J,y} p_m p_{n,y} d\Omega = \\ \int_{\Gamma_{IJ}} \rho_I \rho_J p_m p_{n,y} n_y dS - \int_{\Omega_{IJ}} \rho_I \rho_J p_{m,y} p_{n,y} d\Omega. \end{aligned} \tag{4.33}$$

By substituting Equation (4.33) into Equation (4.26) we have

$$\int_{\Omega_{IJ}} h_{Im,y} h_{In,y} d\Omega = \int_{\Omega_{IJ}} \rho_{I,y} \rho_{J,y} p_m p_n d\Omega + \int_{\Gamma_{IJ}} \rho_I \rho_J p_m p_{n,y} n_y dS. \tag{4.34}$$

For the improvement of analytical integration on the lens domain, we transformed the original equation into more efficient forms. However, It should be noted that these equations are applicable only when the term p_m is identical with the term p_n.

4.3 Numerical integration for method of finite spheres

At this stage, it is needed to classify the kinds of spheres, so we call the sphere which does not have any intersection with the boundary an *inner sphere*, the sphere which contacts on boundary a *contact sphere*, the sphere which lies on the boundary a *boundary sphere*, as shown in Figure 4-5. The inner sphere is entirely in the domain and $\Omega_I \bigcap \Gamma = 0$. The in-

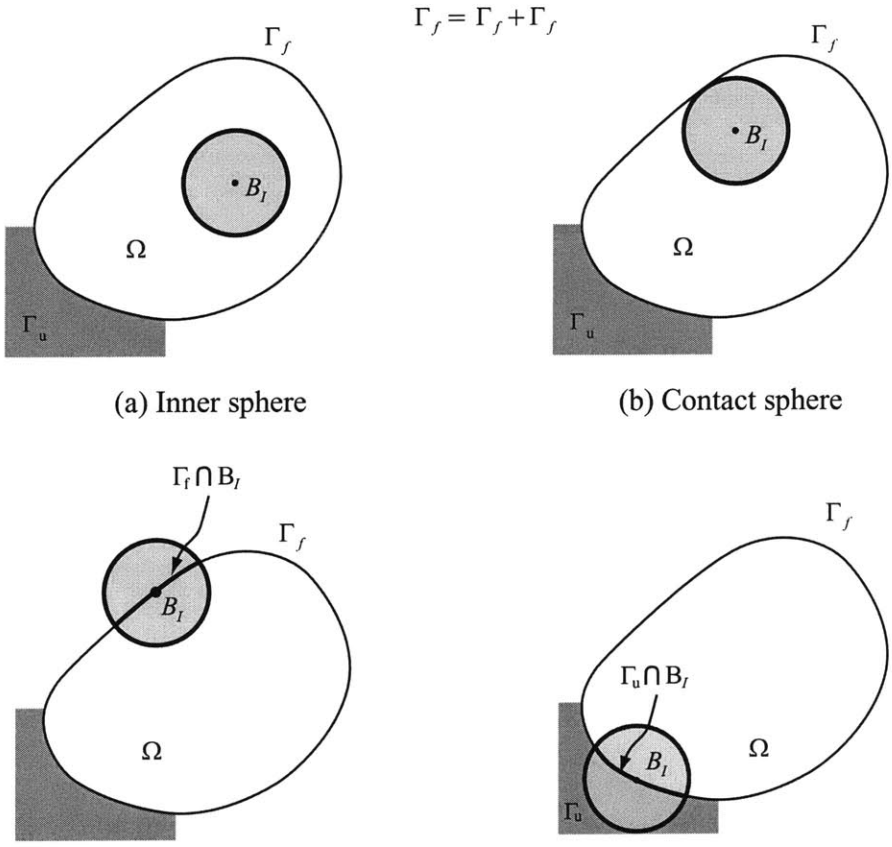

(a) Inner sphere (b) Contact sphere

(c) Boundary sphere on Neumann boundary (d) Boundary sphere on Dirichlet boundary

Figure 4-5: Figures of (a) inner sphere, (b) contact sphere, (c) boundary sphere on Neumann boundary Γ_f, (d) boundary sphere on Dirichlet boundary Γ_u

tersection of contact sphere and boundary is a point. The boundary sphere has intersection with either Dirichlet boundary or Neumann boundary.

Since the integrands in Equation (4.1) are not polynomials and are rational functions, the numerical integration is unavoidable. For the inner spheres which do not have any intersection with the boundary, we apply a piecewise midpoint rule to integrate the stiffness values as shown in Figure 4-6 [18].

For the lens shape integration, we also apply a piecewise rule as shown in Figure 4-7 [18].

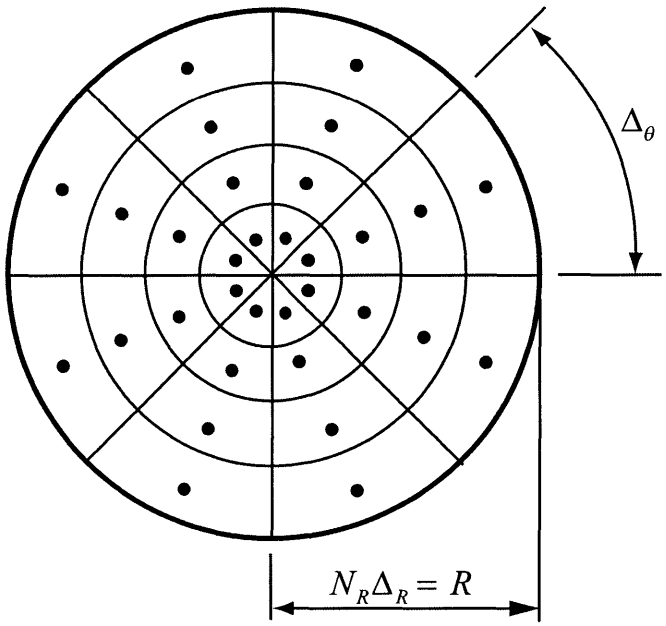

Figure 4-6: Inner sphere integration scheme. Midpoint rule is applied, and the sampling points are determined by Equations (4.36) and (4.37).

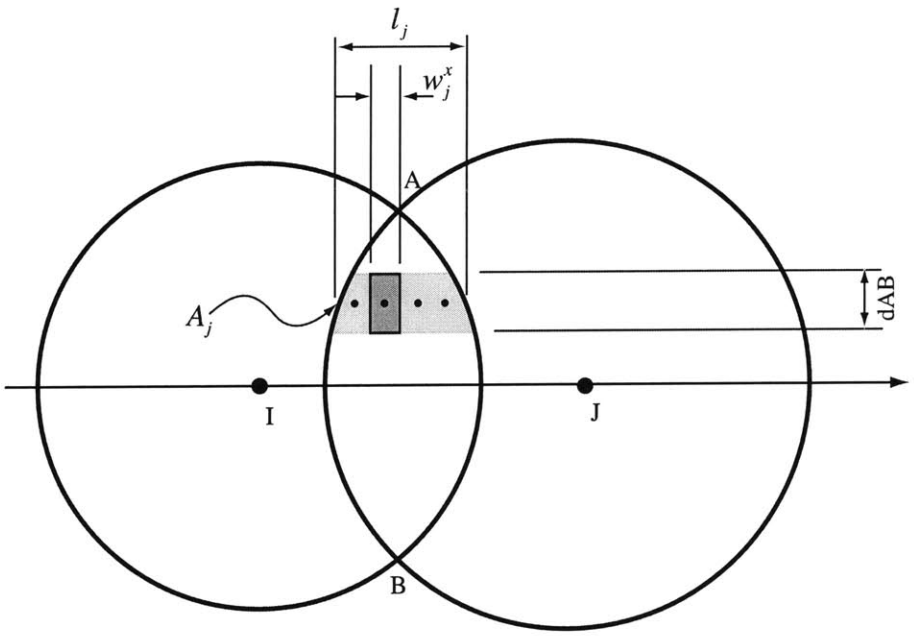

Figure 4-7: Lens integration scheme, where A_j is the area of a strip, w_i^x is the width of the small piece.

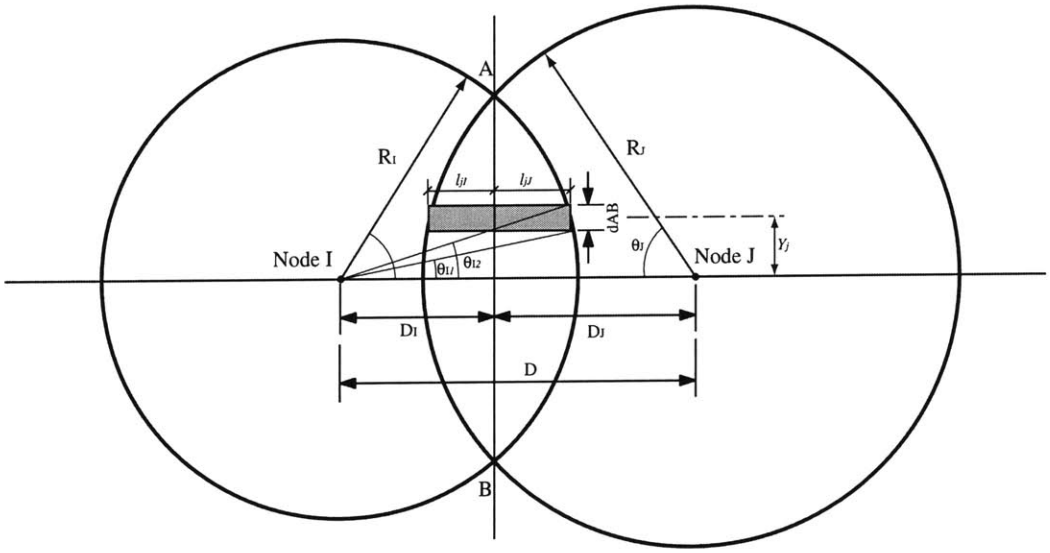

Figure 4-8: A integration scheme for lens domain. Overlapped region is decomposed into pieces and the variables are calculated.

4.3.1 Midpoint integration method for the inner sphere

The implementation of numerical integration is performed by subdividing the sphere into sections which have concentric circular and radial sides. We evaluate the integration value by using the area as a weighting factor for the numerical integration as:

$$\iint_{\Omega} f(x,y)dxdy \approx \sum_{i=1}^{N_\theta}\sum_{j=1}^{N_R} D_{ij} f(x_{ij}, y_{ij}), \tag{4.35}$$

in which N_θ is the number of the angular sectors and N_R is the number of the section in radial direction. Here x and y can be expressed in the cylindrical coordinate system as $r_j cos\theta_i$ and $r_j sin\theta_i$. The locations of integration points can be determined by

$$r_j = \frac{j^2 - j + 1/3}{j - 1/2}\Delta_R, \tag{4.36}$$

$$\theta_i = (i - 1/2)\Delta_\theta, \tag{4.37}$$

where $\Delta_R = R_I/N_R$, $\Delta_\theta = 2\pi/N_\theta$, and the weighting factor D_{ij} is $(j - 1/2)\Delta_\theta(\Delta_R)^2$.

4.3.2 Integration on the lens domain

To integrate on the lens shape region of intersections of two spheres, we need to have special rules. In this section, we explain the existing scheme for numerically evaluating $\int\int_{\Omega_{IJ}} f(x,y)dxdy$, where Ω_{IJ} is intersection of sphere I and sphere J.

For the lens shape domain integration as illustrated in Figure 4-7, the intersections of two spheres are defined as the point A and the point B, and the number of sections along this AB direction is chosen as N_y. We subdivide the lens into slivers which have the same

width, then for each sliver we find the integration points to have the same weighting factor. We draw a horizontal line l_j passing through the center line of each strip. Now we can set a set of points such that $l_j = \sum_{i=1}^{N_x} w_i^x$. This quadrature rule can be described as [26]

$$\iint_{\Omega_{IJ}} f(x,y)dxdy \approx \sum_{i=1}^{Nx}\sum_{j=1}^{Ny} D_{ij} f(x_i, y_j), \tag{4.38}$$

$$D_{ij} = \frac{A_j w_i^x}{l_j}, \tag{4.39}$$

where A_j is the area of the j^{th} strip, w_i^x is the width of the small rectangular piece, and D_{ij} is the integration weighting factor.

For the implementation of the lens integration rule, we need to calculate the factors A_j and l_j. We consider spheres overlapped as in Figure 4-8. For the sphere I setting the node I as the origin of coordinate system, we have the equations as

$$x^2 + y^2 = {R_I}^2, \tag{4.40}$$

$$x = \sqrt{{R_I}^2 - y^2}, \tag{4.41}$$

$$y = R_I \sin\theta. \tag{4.42}$$

Corresponding to the given height y, we can determine the angle θ,

$$\theta = \arcsin\frac{y}{R_I}. \tag{4.43}$$

Assuming that node I is located on the origin of the cartesian coordinate, the area can be

obtained by the equation

$$\int xdy = \int {R_I}^2 \cos^2\theta d\theta = \frac{{R_I}^2}{2}\left[\theta + \frac{\sin 2\theta}{2}\right]. \tag{4.44}$$

Then the area of the jth strip can be determined by

$$dA = \frac{{R_I}^2}{2}\left[\theta + \frac{\sin 2\theta}{2}\right]_{\theta_{I1}}^{\theta_{I2}} - D_I\ dAB, \tag{4.45}$$

where

$$\theta_{I2} = \arcsin\left[\frac{D_I - (j-1)dAB}{R_I}\right], \tag{4.46}$$

$$\theta_{I1} = \arcsin\left[\frac{D_I - (j)dAB}{R_I}\right]. \tag{4.47}$$

The height of center line for jth strip is

$$Y_j = AB/2 - (j - \frac{1}{2}\ dAB). \tag{4.48}$$

To calculate l_j, we need to separate it into left part and right part, and the equations are

$$l_{jI} = \sqrt{{R_I}^2 - {y_j}^2} - D_I, \tag{4.49}$$

$$l_{jJ} = \sqrt{{R_I}^2 - {y_j}^2} - (D - D_I), \tag{4.50}$$

$$l_j = l_{jI} + l_{jJ}. \tag{4.51}$$

4.4 New integration scheme for the inner spheres and boundary spheres

The integrands of the method of finite sphere are highly complicated. However, we have some good characteristic which we can utilize for the improvement of numerical integration. First, the shape function has compact support although the sphere overlaps with others. Therefore, we can divide the domains into several subdomains which can be described more neatly within the subdomains.

We recall the Shepard partition of unity functions

$$\rho_I(\mathbf{x}) = \frac{W_I(\mathbf{x})}{\sum_{J=1}^{N} W_J(\mathbf{x})}, \qquad I = 1, 2, \ldots, N. \tag{4.52}$$

The derivatives in $x-$ and $y-$directions can be obtained as

$$\rho_{I,x}(\mathbf{x}) = \left[W_{I,x} - \frac{W_I}{\sum_{J=1}^{N} W_J} \sum_{J=1}^{N} W_{J,x} \right] \frac{1}{\sum_{J=1}^{N} W_J}, \tag{4.53}$$

$$\rho_{I,y}(\mathbf{x}) = \left[W_{I,y} - \frac{W_I}{\sum_{J=1}^{N} W_J} \sum_{J=1}^{N} W_{J,y} \right] \frac{1}{\sum_{J=1}^{N} W_J}. \tag{4.54}$$

In the improved equations, we are asked to calculate the integrands of $\rho_{I,x}^2 p_m p_n$ and $\rho_{I,x}\rho_{I,y} p_m p_n$,

Subsection	θ^{start}	θ^{end}	R^1	R^1
I	θ_I^{start}	θ_I^{end}	R_I^1	R_I^2
II	$\theta_{II}^{\text{start}}$	θ_{II}^{end}	R_{II}^1	R_{II}^2
III	$\theta_{III}^{\text{start}}$	$\theta_{III}^{\text{end}}$	R_{III}^1	R_{III}^2
IV	$\theta_{IV}^{\text{start}}$	θ_{IV}^{end}	R_{IV}^1	R_{IV}^2

Table 4.1: Establishment of subsections for sphere integration.

$\rho_{I,x}^2 p_m p_n$. By substituting the Shepard functions into the terms, we have

$$\rho_{I,x}^2 p_m p_n = \left[W_{I,x} - \frac{W_I}{\sum_{J=1}^N W_J} \sum_{J=1}^N W_{J,x} \right]^2 \frac{p_m p_n}{\left[\sum_{J=1}^N W_J \right]^2}, \tag{4.55}$$

$$\rho_{I,y}^2 p_m p_n = \left[W_{I,y} - \frac{W_I}{\sum_{J=1}^N W_J} \sum_{J=1}^N W_{J,y} \right]^2 \frac{p_m p_n}{\left[\sum_{J=1}^N W_J \right]^2}, \tag{4.56}$$

$$\begin{aligned} \rho_{I,x}\rho_{I,y} p_m p_n = & \left[W_{I,x} - \frac{W_I}{\sum_{J=1}^N W_J} \sum_{J=1}^N W_{J,x} \right] \left[W_{I,y} - \frac{W_I}{\sum_{J=1}^N W_J} \sum_{J=1}^N W_{J,y} \right] \\ & \times \frac{p_m p_n}{\left[\sum_{J=1}^N W_J \right]^2}. \end{aligned} \tag{4.57}$$

We have a common factor $\left[\sum_{J=1}^N W_J \right]^2$ in above equations as a denominator and near the boundary of the weighting function, this value becomes very small when the overlapping ratio is small. In this case, the values of Equations (4.55) to (4.57) are scaled by the factor of $1/\left[\sum_{J=1}^N W_J \right]^2$. Therefore, on this overlapped region, the integrands in Equations (4.55) to (4.57) have relatively large values with intensive variations. Another important observation is that the terms of $\{p_m p_n\}$ are $\{1, x, y, xy, x^2, y^2\}$. Since the span of the local basis is $\{1, x, y\}$ which has the origin at the center of sphere, it is possible to divide the sections regarding $x-$ and $y-$ coordinates.

To calculate more accurately in those regions, we need to determine the numerical integration sections adaptively as shown in Figure 4-9. For the inner sphere as shown in Figure 4-9-(a), we divide the whole domain into four subdomains ($0 \leq \theta \leq 0.5\pi, 0.5\pi \leq \theta \leq \pi, pi \leq \theta \leq 1.5\pi, 1.5\pi \leq \theta \leq 2\pi$), namely section I, II, III, and IV, since the basis of the integrands contains x and y as a component.

For example, we introduce R_I^1 and R_I^2 for the section I. R_I^1 is the starting range of the integration in radial direction and is obtained calculating distance from the origin of J^{th} sphere to the boundary of other spheres. From 0 to R_I^1, the integrands are null since at integration points where it has only one weighting function. Hence $\rho_J(\mathbf{x})$ is unity and the derivatives are zeros ($\rho_{J,x}(\mathbf{x}) = 0, \rho_{J,y}(\mathbf{x}) = 0$). Therefore, we eliminate the unnecessary computations. The integration ends at R_I^2 and another integration start from R_I^2 to radius of the sphere J. R_I^2 is determined considering least overlap with neighbor spheres. Similarly, θ_I^1 is the starting range of the integration in the tangential direction and θ_I^2 is the end of integration angle. Therefore we have $(R_I^1, R_I^2, R_{II}^1, R_{II}^2, \cdots, R_{IV}^1, R_{IV}^2)$ for a sphere J. For the inner spheres, we have eight sectors and the integration is

$$\begin{aligned}\int f(r,\theta) r \, dr d\theta = &\int_{R_I^1}^{R_I^2} \int_{\theta_I^1}^{\theta_I^2} f(r,\theta) r \, dr d\theta + \int_{R_I^2}^{R(I)} \int_{\theta_I^1}^{\theta_I^2} f(r,\theta) r \, dr d\theta \\ &\cdots + \int_{R_{IV}^1}^{R_{IV}^2} \int_{\theta_{IV}^1}^{\theta_{IV}^2} f(r,\theta) r \, dr d\theta + \int_{R_{IV}^2}^{R(I)} \int_{\theta_{IV}^1}^{\theta_{IV}^2} f(r,\theta) r \, dr d\theta\end{aligned} \tag{4.58}$$

We apply the midpoint rule for each sector to integrate. For the boundary spheres, we need to divide sectors more carefully. Only sectors which exist in the domain are considered as shown in Figure 4-9-(b).

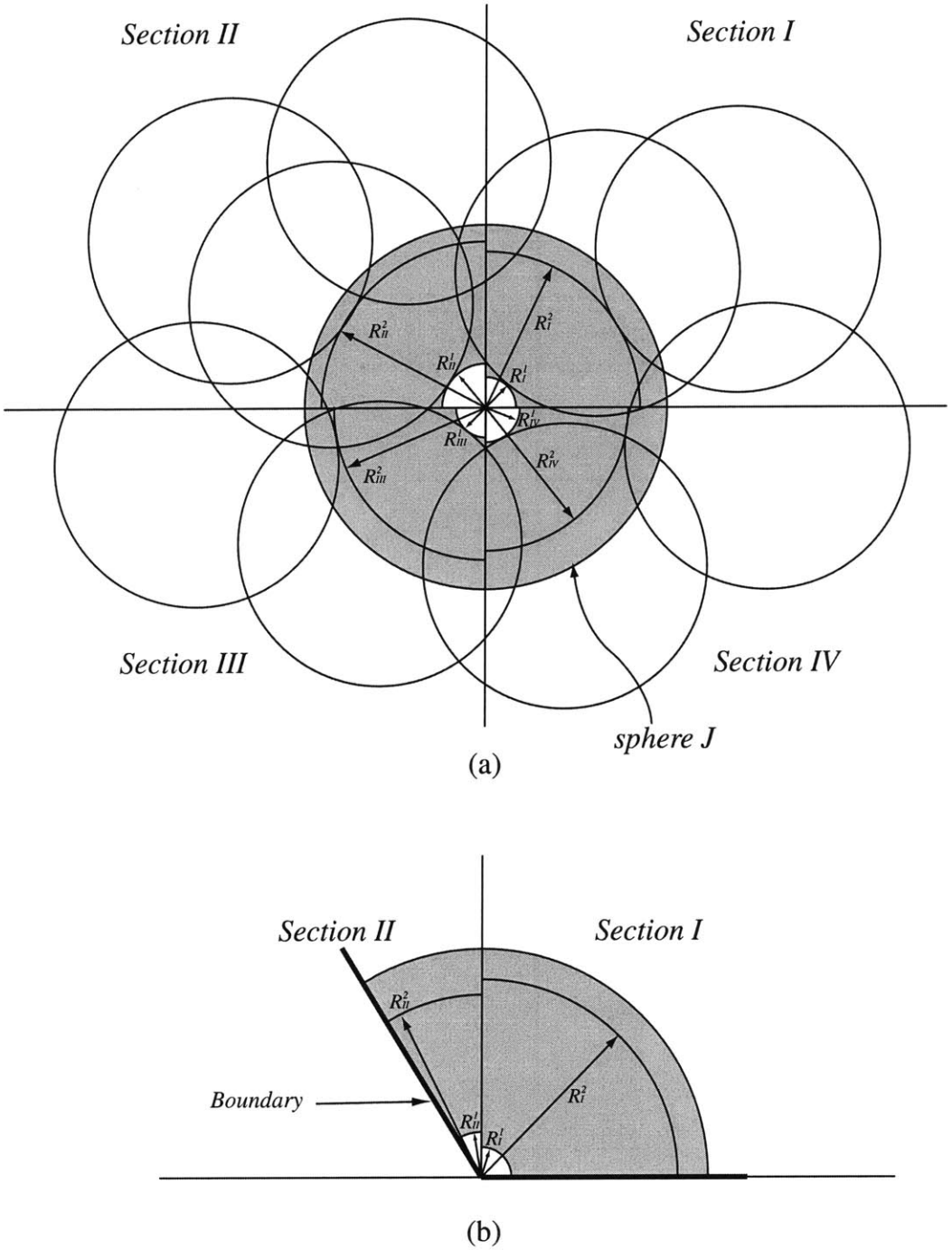

Figure 4-9: New integration scheme for the inner sphere. (a) The sphere J is divided into four domains based on the angle and determine neighboring spheres which are located in each region of angle. (b) Boundary sphere.

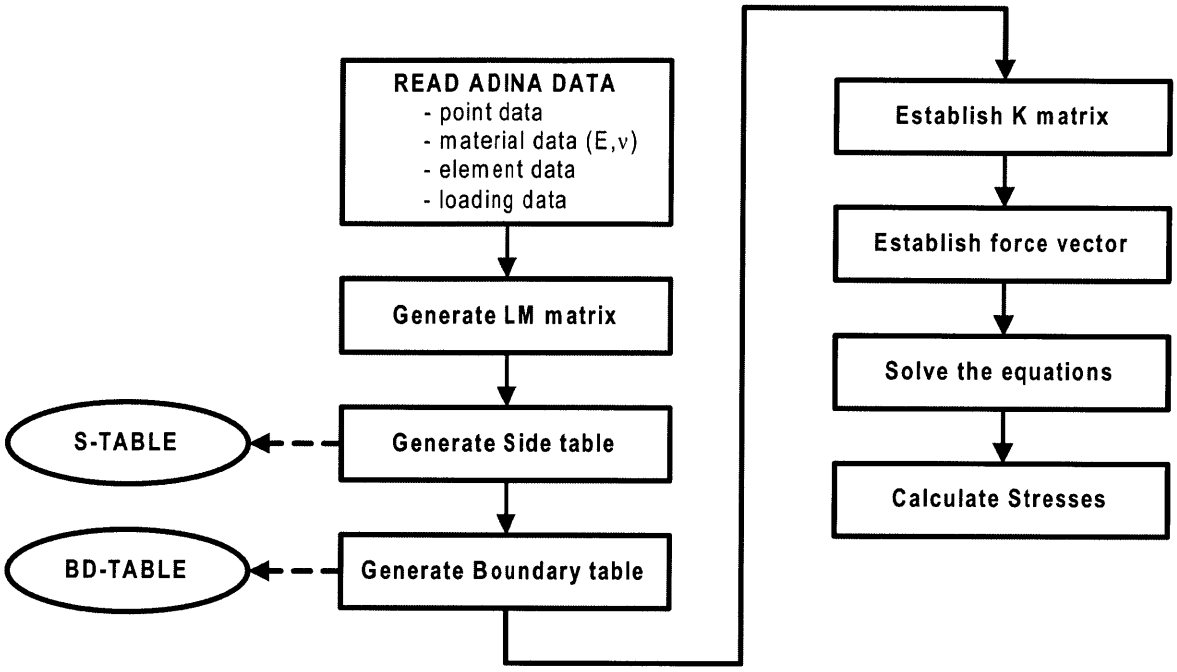

Figure 4-10: Automatic radius calculation scheme.

4.5 Automatic generation of spheres in MFS

In the MFS, one of the important tasks is automatic generation of spheres, which includes the detection of boundary and the determination of radii of all the spheres. There is only one restriction that the union of spheres must cover the whole domain without emptiness for generating these approximation functions.

We adopt an practical way to generate spheres by using ADINA input data. This choice gives us several advantages such as usage of the powerful node generating scheme of ADINA and convenient result comparison with the exact same node distribution in FEM solution. Figure 4-10 shows the procedure to obtain necessary information from ADINA data file and to calculate radii of spheres. The program STAP_MFS has been developed from STAP program to implement the MFS method. The first important stage consists of estab-

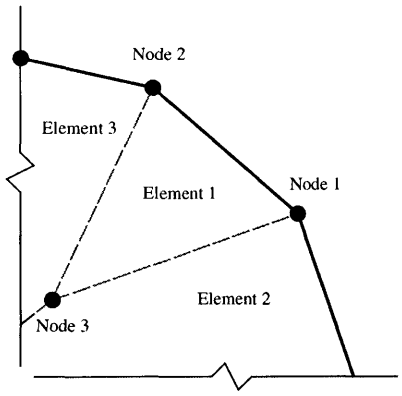

Side Table

N1	N2	Flag
1	2	0
2	3	0
1	3	1
.	.	.
1	3	0
2	3	1
1	3	1
.	.	.
.	.	.

Repeated

Figure 4-11: Edge table generation scheme. Each row of the edge table contains information about the nodes that are on an element edge. The format is (N1,N2,flipping flag), where N1 and N2 are the nodes connected be the edge and the flipping flag takes on a value of zero if the order is N2 $<$ N1 in the original connectivity and a value of 1 if the original order is reversed.

lishing a edge table and a boundary table. This information saved in these two tables is used to detect the intersection with spheres and domain boundaries.

The process of generating the "edge table" from the raw data is described in Figure 4-11. Each row has components of N1, N2, and flipping flag, in which N1 and N2 are nodes on a edge of a element. When the element connecting sequence is descending order, the flag is unity, otherwise, the value is null. This information designates the boundary line vector which is counter clockwise. The same $N1$ and $N2$ values appear when the edge is not on the boundary because the edge is common to two elements. By eliminating repeated values in the edge table, we can get the boundary table. The boundary table has the information about the boundary nodes and the sequences.

As a next stage, we categorize spheres into three kinds of spheres (inner sphere, contact sphere, boundary sphere.) The pure sphere does not contact with boundary and purely inside the domain, contact sphere contacts with boundary line, so the intersection is a point,

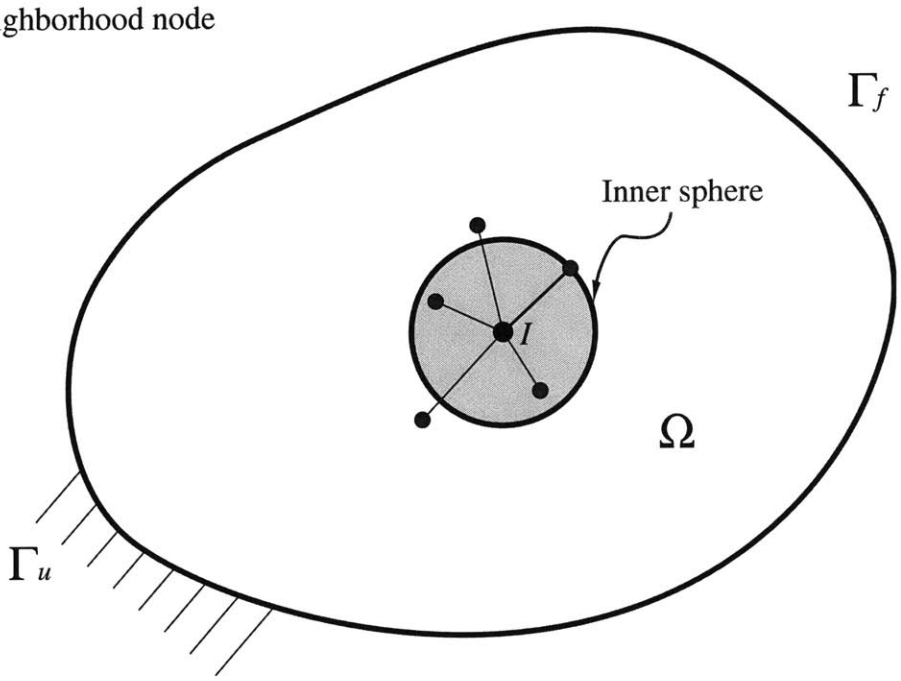

Figure 4-12: Inner sphere: The radius is determined by average value of node-distance of neighboring nodes.

and boundary sphere is located on boundary. For the inner sphere, the radius is determined by average value of node-distance of neighboring nodes as shown in Figure 4-12. The radius of contact sphere is the radius which imposes the contact condition with boundary the boundary as in Figure 4-13, and the boundary sphere has minimum length of distances to adjacent two nodes shown in Figure 4-14. We implemented our auto sphere generation scheme for various geometries frequently met in mechanical analysis as illustrated in Figure 4-15 to Figure 4-17. In the first example, there is a plate with two holes and 175 spheres cover entire domain properly. Contact spheres were generated to touch the boundary and centers of boundary spheres are aligned along the boundary properly. Second example in Figure 4-16 is annular section and 37 spheres cover the domain. In the third example a quarter of a plate with a hole is covered by 168 spheres.

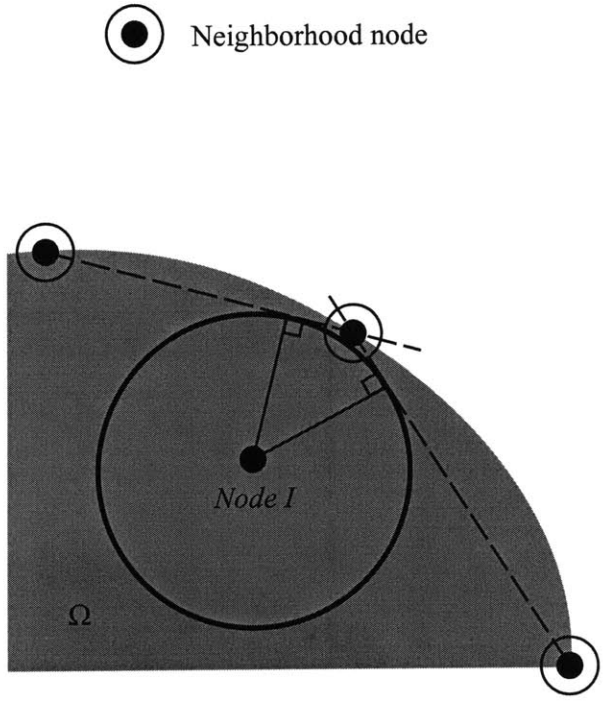

Figure 4-13: Contact sphere: Node (I) has at least two neighborhood nodes which require special attention. The normal distance from node I to adjacent edges are computed and the minimum distance is adopted as radius

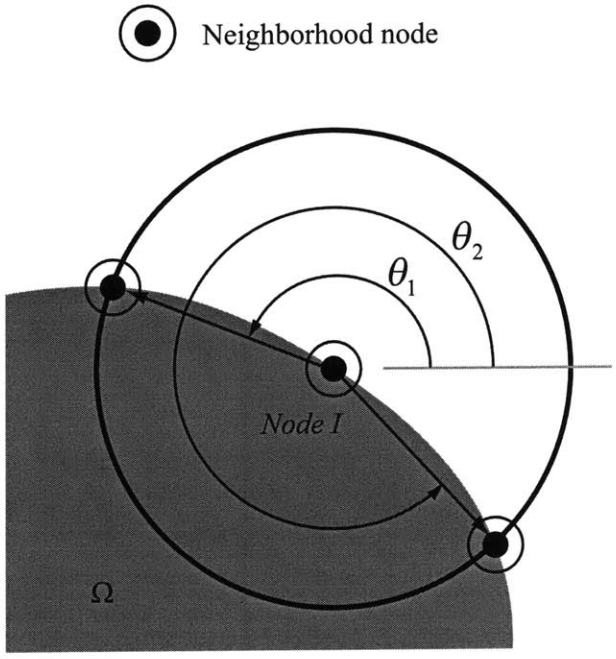

Figure 4-14: Boundary sphere: The boundary nodes are obtained from the boundary table. The radius of the sphere at a boundary node is selected as the minimum of the two nearest neighbor distances. The included angles θ_1 and θ_2 are used in the numerical integration

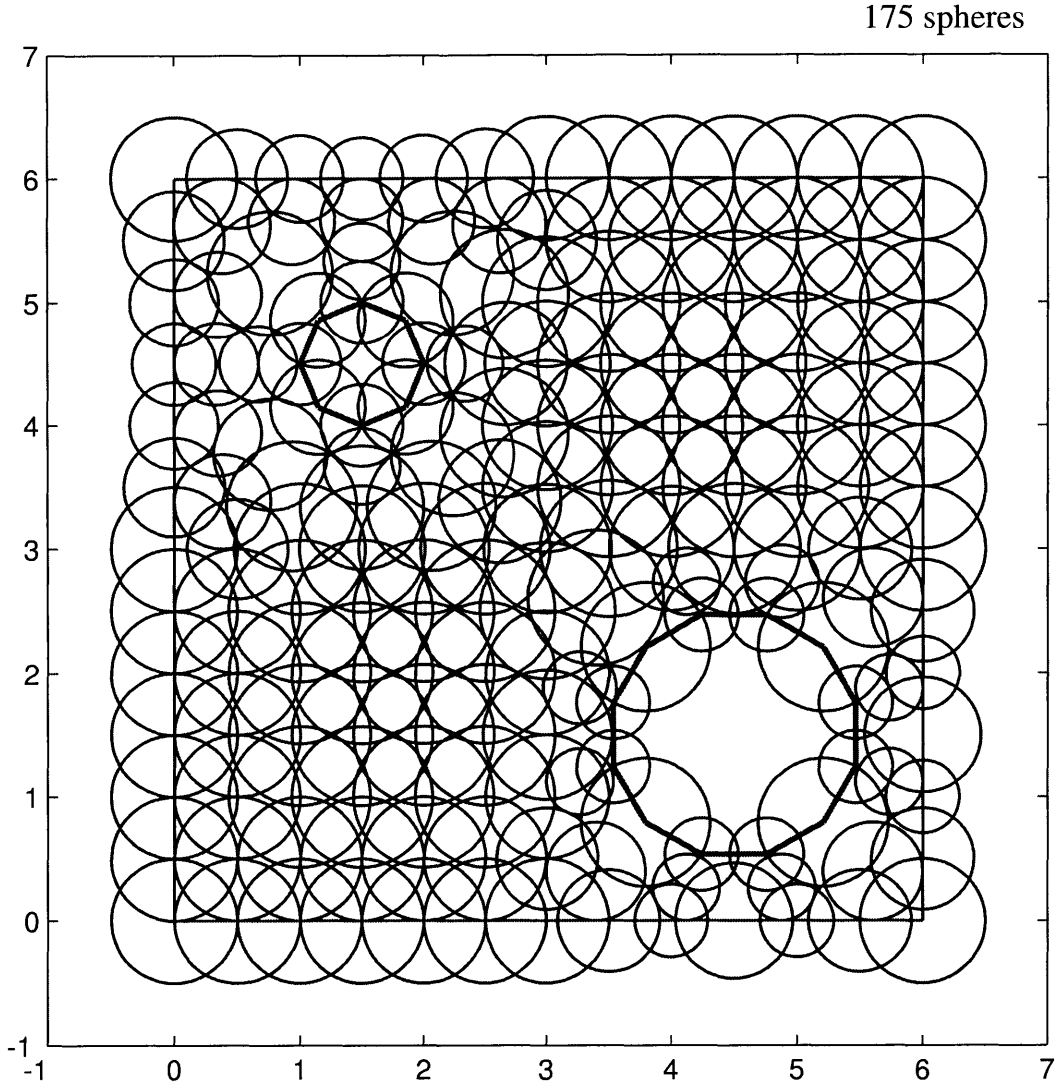

Figure 4-15: Example of auto sphere generation: The plate has two holes and sphere generation is implemented automatically. 175 spheres are distributed to cover the whole domain.

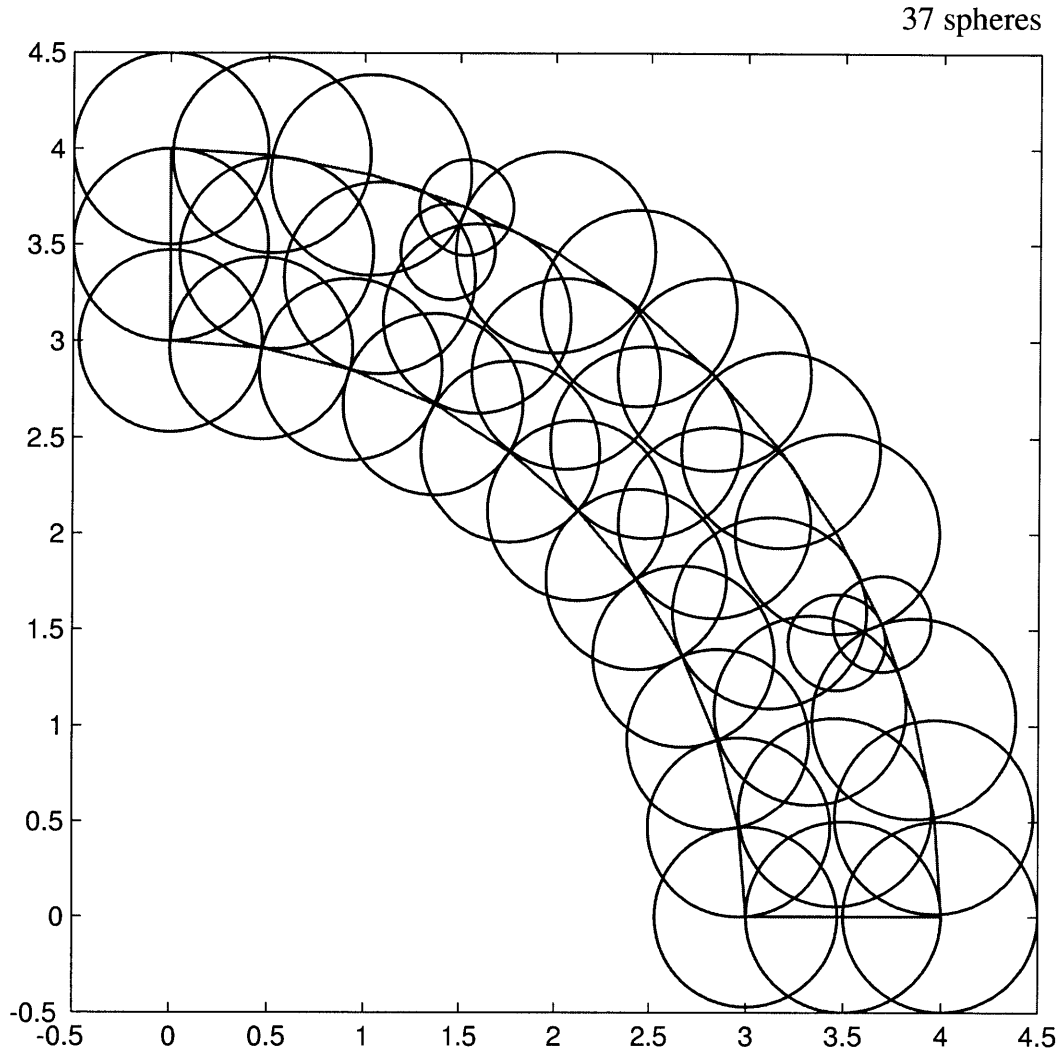

Figure 4-16: Example of auto sphere generation: For the annular section sphere generation is implemented automatically. 37 spheres are distributed to cover the whole domain.

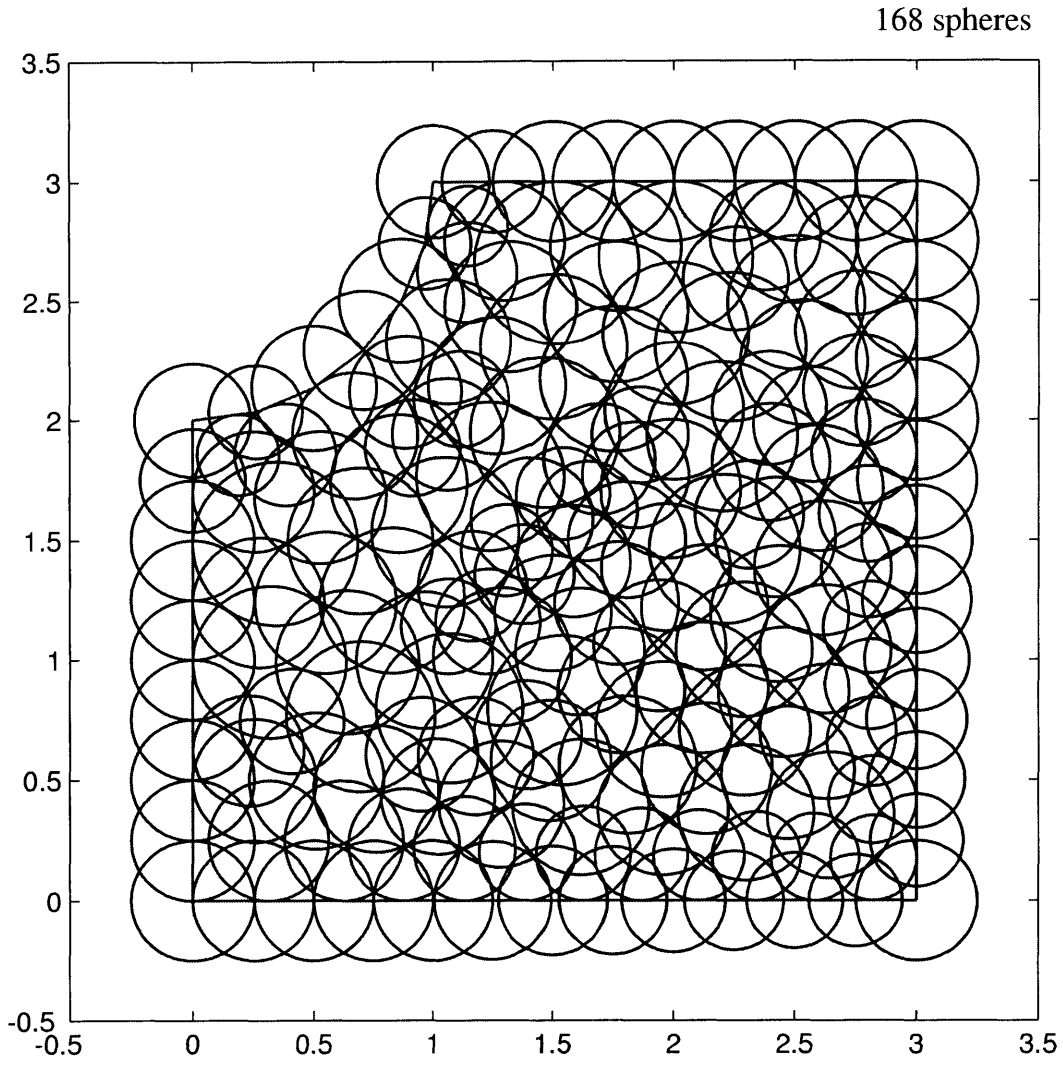

Figure 4-17: Example of auto sphere generation: For the quarter of a plate which has a hole sphere generation is implemented automatically. 168 spheres are distributed to cover the whole domain.

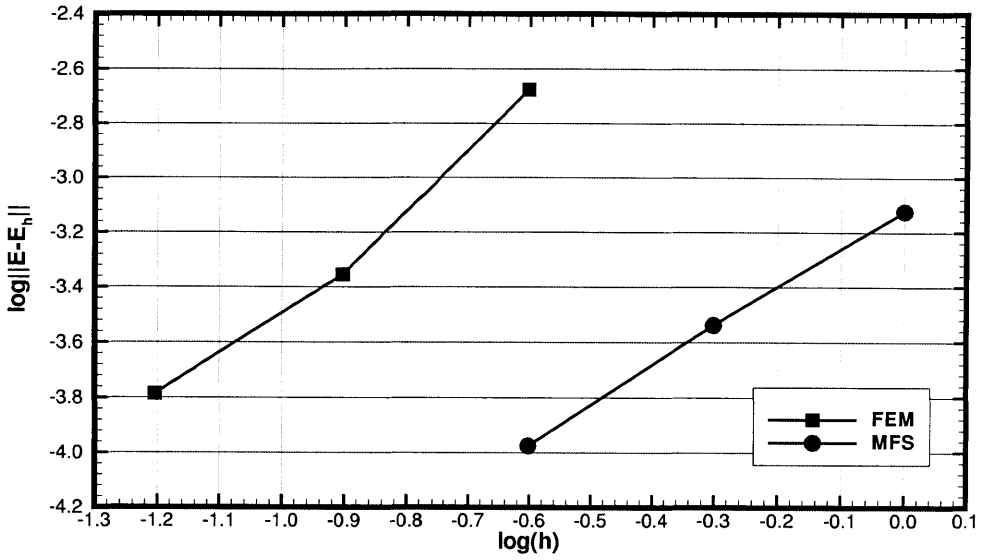

Figure 4-18: Convergence comparison of finite element method and method of finite spheres.

4.6 A numerical result

The improved formulation was used to solve some typical two dimensional linear elastic problems. Here we consider a cantilever plate in plane strain conditions, subjected to uniform pressure loading; we use Young's modulus $E = 100$, Poisson's ratio $\nu = 0.3$, $L = 1$, and $p = 1$. For the finite element solution, we use 4-node elements in 4×4, 8×8, and 16×16 element meshes, and for the method of finite spheres 1×1, 2×2, and 4×4 nodal arrangements were employed.

Figure 4-18 shows the results of convergence in strain energy. The figure shows that the method of finite spheres results in the same order of convergence (as expected), but the error is much smaller for a given number of nodal points.

Chapter 5

Coupling of Finite Elements and Finite Spheres

5.1 Introduction

For several decades, the development of the finite element method has been pursued and is now efficient for complex structures or domains. However, the finite element method is expensive in preparing the mesh and in some cases, notably in nonlinear analysis, mesh regenerations may be necessary and are costly. On the other hand, meshless techniques eliminate the mesh generation procedure in the analysis, but are confronting difficulties in numerical integration, namely, the integrands are not rational functions. Also, the essential boundary conditions are not as easily imposed as in the finite element method. To overcome these difficulties, some effort was made to couple the finite element method/boundary element method and meshless techniques [27–29]. The coupling of the finite element method and meshless techniques enables to utilize mutual advantages. The basic idea is that finite ele-

ments are employed for the domain which is easily meshed and does not need re-meshing and the meshless elements are modeling the domain which is difficult to mesh and may need remeshing in nonlinear analysis. However, the major difficulty with the coupling is to enforce the displacement compatibility on the interface boundary between the meshless domain and the finite element domain and ensure the continuity of the displacements and possibly derivatives. Although some methods for the coupling were proposed, the first order consistency in the coupled domain was not ensured. In this chapter, we propose a new coupling scheme using finite elements and finite spheres [18, 30]. We consider the 4-node finite element in the coupling with finite spheres and achieve continuity of the stress and strain fields in the domain of overlap.

We also propose another coupling scheme in case we simply want to enrich the interpolation in the finite element domain. In this method, the finite sphere bases are added to the existing finite element interpolations. This approach provides adaptability and versatility since it is possible to add or remove spheres adaptively. The spheres can be added in local areas of the entire analysis domain and the solution then depicts high order regularity in displacements, stresses, and strains fields.

The promising application area of the new coupling scheme are stress concentration analysis and crack propagation simulation. Cracks grow in arbitrary direction under mixed loading conditions. To trace the propagation of each crack, the propagation direction should be analyzed. Our new coupling schemes have great advantages since we can employ spheres at the crack tip to enrich the approximation functions. It is not required to generate a finer mesh at each step at the cracks and we can use the basic mesh for the entire analysis.

5.2 Coupling finite element discretizations with finite sphere discretizations

In the formulation to couple the finite element and finite sphere discretizations, we need to categorize regions in the domain and construct the shape functions in the entire domain. As illustrated in Figure 5-1-(a), we have originally N_{el} finite elements and $N_{spheres}$ finite spheres and they have overlapped subdomains which we call "coupled" domain. We categorize the whole domain into three different domains as shown in Figure 5-1-(b). We call Ω_{FE} the domain which does not have any overlapping with finite spheres, Ω_{FE-FS} the coupled domain which is the union of finite elements that overlaps with spheres, and Ω_{FS} the pure finite sphere domain which consists of spheres.

The domain $\{\Omega_{FE}^{(k)}, k \in \mathcal{M}\}$ denotes an individual finite element subdomain, $\{\Omega_{FE-FS}^{(k)}, k \in \mathcal{N}\}$ means a coupled element subdomain and $\{\Omega_{FS}^{(k)}, k \in \mathcal{S}\}$ is for a sphere subdomain.

The nodal coefficient vector consists of values corresponding to the degrees of freedoms of the finite elements and the finite spheres as

$$\mathbf{U}^T = [\mathbf{u}_1\ \mathbf{u}_2 \ldots \mathbf{u}_{N_{FEM}} \mid \boldsymbol{\alpha}_{10}\boldsymbol{\alpha}_{11} \ldots \boldsymbol{\alpha}_{N_{spheres}N_{pol}}] \tag{5.1}$$

where the coefficients $\mathbf{u}_I = [u_I\ v_I]$ and $\boldsymbol{\alpha}_{Im} = [u_{Im}\ v_{Im}]$. N_{FEM} is the total number of finite element nodes, $N_{spheres}$ the number of finite spheres, and $Npol$ the number of terms in the polynomials of the spheres used. For the index $0, 1, 2$ we have $N_{pol} = 3$.

For the pure finite element subdomain $\Omega_{FE}^{(k)}$, we have only the conventional shape functions $h_I^{FE}(\mathbf{x})$. In the pure finite sphere subdomain belonging to the sphere I, the shape

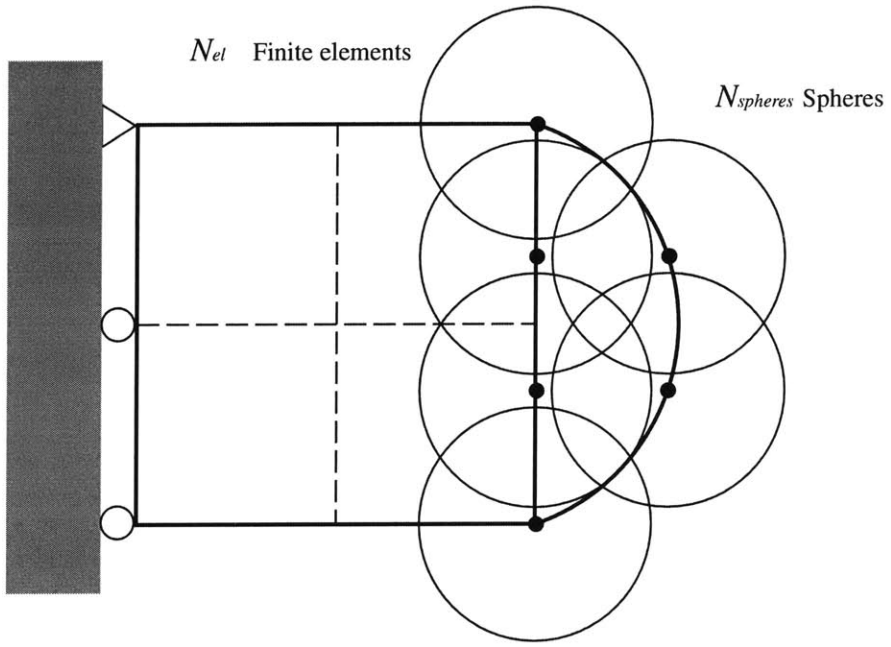

(a)

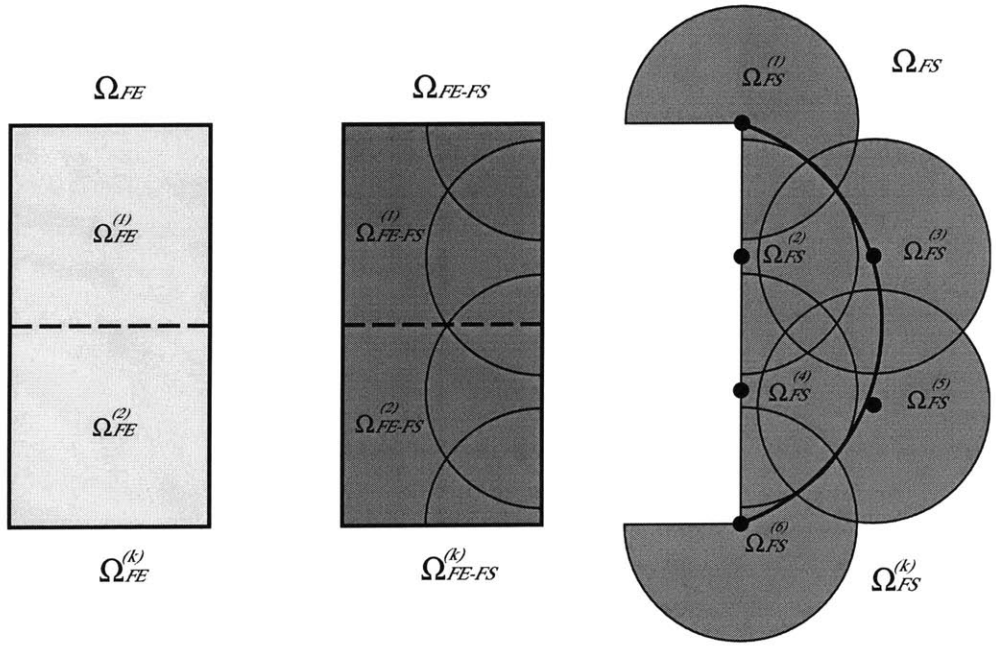

(b)

Figure 5-1: Coupling finite element discretized domains with finite spheres discretized domains: (a) Coupling scheme and (b) computational domain decomposition. We call Ω_{FE} the domain which does not have any overlapping with finite spheres, Ω_{FE-FS} the union of finite elements which have non-zero overlap with spheres, and Ω_{FS} the region which consists of spheres.

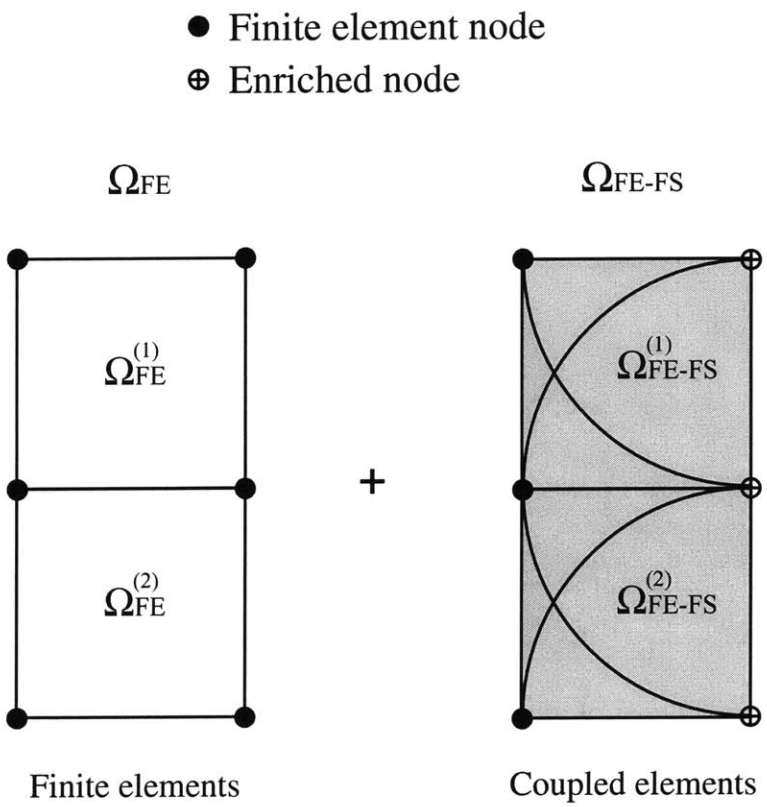

Figure 5-2: Enriching a finite element discretization with finite spheres: We call Ω_{FE} the domain which is not enriched with finite spheres, and Ω_{FE-FS}, the domain of finite elements enriched with spheres. It should be noted that there is no pure finite sphere domain.

functions are $h_{Im}^{FS}(\mathbf{x})$. The construction of shape functions can be achieved by multiplying local basis to the Shepard function with the relation of $h_{Im} = \rho_I(\mathbf{x})\, p_m(\mathbf{x})$ as in [13]. The coupling subdomains have the shape function $h_I^{FE-FS}(\mathbf{x})$ which correspond to the finite element and $h_{Im}^{FE-FS}(\mathbf{x})$ corresponding to the finite spheres.

5.2.1 Construction of shape function on coupled domain

For details of the shape functions on Ω_{FE} and Ω_{FE}, we refer to [2, 13]. Using the partition of unity, we obtain the equations for the shape functions for subdomain Ω_{FE-FS} of the form

$$h_I^{FE-FS}(\mathbf{x}) = \frac{h_I(\mathbf{x})}{W^{(k)}}, \qquad I = 1, 2, \ldots, N_{spheres}, \tag{5.2}$$

$$\rho_I^{FE-FS}(\mathbf{x}) = \frac{W_I(\mathbf{x})}{W^{(k)}}, \qquad I = 1, 2, \ldots, N_{spheres}, \tag{5.3}$$

$$h_{Im}^{FE-FS}(\mathbf{x}) = \rho_I^{FE-FS}(\mathbf{x}) p_m(\mathbf{x}). \tag{5.4}$$

where $W^{(k)}$ is the total sum of all the weighting functions which have non-zero values on the domain $\Omega_{FE-FS}^{(k)}$ written as

$$W^{(k)}(\mathbf{x}) = \sum_{K=1}^{N_{spheres}^{(k)}} W_K(\mathbf{x}) + \sum_{I=1}^{4} h_I(\mathbf{x}) \tag{5.5}$$

where K is the index set of finite spheres, I is the index set of nodes belonging to the finite elements, and $N^{(k)} = N_{spheres}^{(k)} + 4$, Here $N_{spheres}^{(k)}$ is the number of spheres which have an intersection with $\Omega_{FE-FS}^{(k)}$, and p_m is a local basis. W_K is the weighting function corresponding to the finite sphere K. It should be noted that the summation of weighing

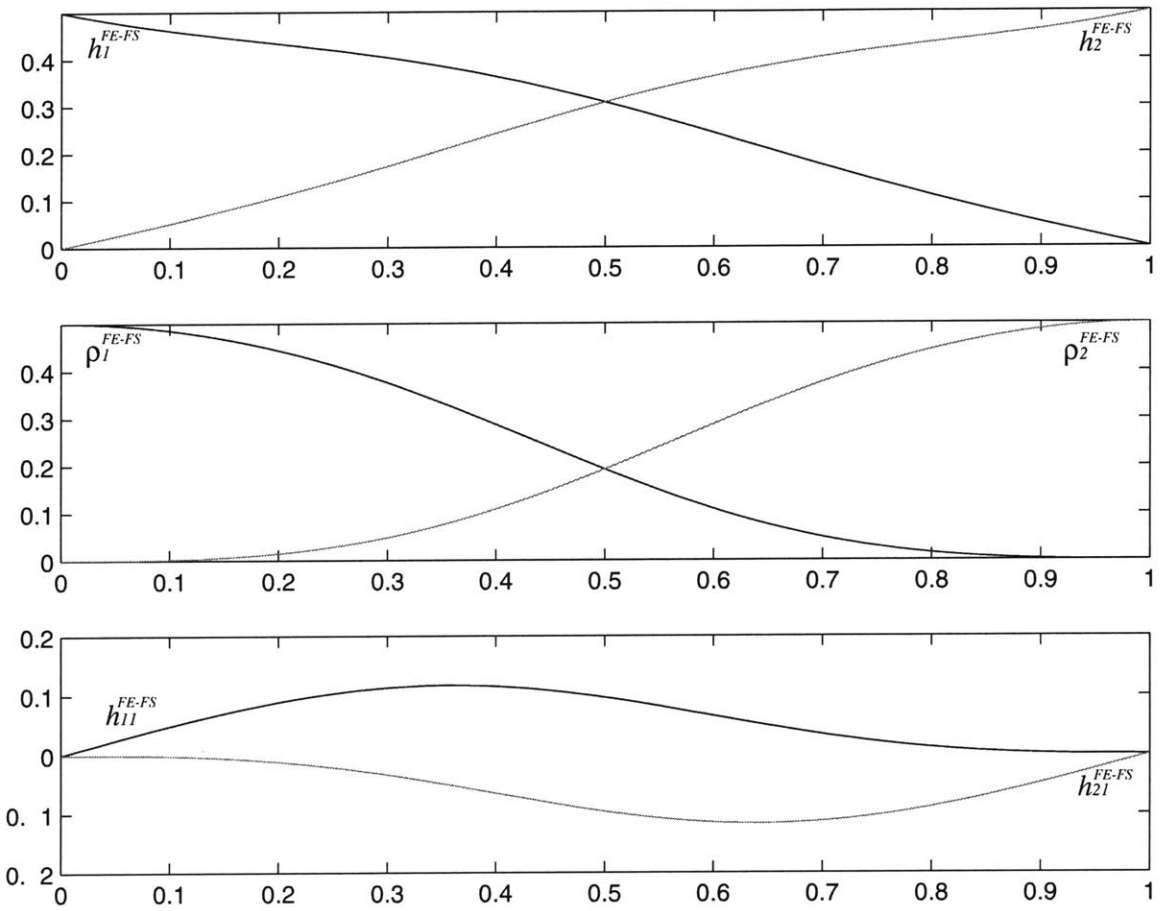

Figure 5-3: Shape functions $h_1^{FE-FS}(x)$, $h_2^{FE-FS}(x)$, $\rho_1^{FE-FS}(x)$, $\rho_2^{FE-FS}(x)$, $h_{11}^{FE-FS}(x)$, and $h_{21}^{FE-FS}(x)$ calculated by Equation (5.3) in a 1-dimensional case when the spheres are located at the both ends, where $R_1, R_2 = 1$.

functions of finite element nodes $\sum_{I=1}^{4} h_I(\mathbf{x})$ is unity in the Ω_{FE} and Ω_{FE-FS}, and the $h_I^{FE}(\mathbf{x})$ is identical with $h_I(\mathbf{x})$ only in Ω_{FE}. We keep the partition of unity characteristic, which ensures that rigid body motion is possible.

As an simple example, we illustrate $h_I^{FE-FS}(x)$ and $h_{Jn}^{FE-FS}(x)$ for the 1-D case in Figure 5-3. On a 2-node one dimensional element, two spheres are placed centered at each node of finite element. $h_1(x)$ and $h_2(x)$ are weighting functions of finite element nodes. $W_1(x)$ and $W_2(x)$ are weighting functions of the finite spheres. The radius of spheres is

assumed to be unity. Then we have weighting functions

$$h_1(x) = 1 - x,$$

$$h_2(x) = x,$$

$$W_1(x) = 1 - 6x^2 + 8x^3 - 3x^4,$$

$$W_2(x) = 1 - 6|x-1|^2 + 8|x-1|^3 - 3|x-1|^4.$$

Substituting these weighting functions into Equations (5.2) to (5.4), the shape functions $h_1(x)$, $h_2(x)$, $\rho_1(x)$, and $\rho_2(x)$ in $\Omega_{FE-FS}(\mathbf{x})$ are

$$h_1^{FE-FS}(x) = \frac{h_1(x)}{h_1(x) + h_2(x) + W_1(x) + W_2(x)},$$

$$h_2^{FE-FS}(x) = \frac{h_2(x)}{h_1(x) + h_2(x) + W_1(x) + W_2(x)},$$

$$\rho_1^{FE-FS}(x) = \frac{W_1(x)}{h_1(x) + h_2(x) + W_1(x) + W_2(x)},$$

$$\rho_2^{FE-FS}(x) = \frac{W_2(x)}{h_1(x) + h_2(x) + W_1(x) + W_2(x)}.$$

By the relation $h_{Im}^{FE-FS}(x) = \rho_I^{FE-FS}(x)p_m$, $h_{11}^{FE-FS}(x)$ and $h_{21}(x)$ are obtained as

$$h_{11}^{FE-FS}(x) = \rho_1^{FE-FS}(x)\ (x - x_1), \tag{5.6}$$

$$h_{21}^{FE-FS}(x) = \rho_2^{FE-FS}(x)\ (x - x_2). \tag{5.7}$$

As shown in Figure 5-3, the shape functions are smooth within the subdomain as expected.

5.2.2 Displacement-based method

We consider the following variational statement for linear elasticity

$$\begin{aligned} &\text{Find} \quad u \in H^1(\Omega) \quad \text{such that} \\ &\int_\Omega \boldsymbol{\epsilon}^T(\mathbf{v})\mathbf{C}\boldsymbol{\epsilon}(\mathbf{u})d\Omega - \int_{\Gamma_u} \left[\boldsymbol{\epsilon}^T(\mathbf{v})\mathbf{C}\mathbf{N}^T\mathbf{u} + \mathbf{v}^T\mathbf{N}\mathbf{C}\boldsymbol{\epsilon}(\mathbf{u})\right] d\Gamma \\ &= \int_\Omega \mathbf{v}^T\mathbf{f}^B d\Omega + \int_{\Gamma_f} \mathbf{v}^T\mathbf{f}^s d\Gamma - \int_{\Gamma_u} \boldsymbol{\epsilon}^T(\mathbf{v})\mathbf{C}\mathbf{N}^T\mathbf{u}^s d\Gamma \qquad \forall \mathbf{v} \in H^1(\Omega), \end{aligned} \tag{5.8}$$

where $\boldsymbol{\epsilon} = [\epsilon_{xx}\ \epsilon_{yy}\ \gamma_{xy}]^T$, $H^1(\Omega)$ is the first order Hilbert space, u is the displacement field, ϵ and τ are the strain and stress vectors, $\mathbf{f}^s$ is the prescribed surface traction vector on the Dirichlet boundary Γ_f, $\mathbf{u}^s$ is the prescribed displacement vector on the boundary Γ_u, $\mathbf{f}^B$ is the body force vector, and $\mathbf{N}$ is defined as

$$\mathbf{N} = \begin{bmatrix} n_x & 0 & n_y \\ 0 & n_y & n_x \end{bmatrix}. \tag{5.9}$$

Note that we use this variational statement for the complete analysis domain, but in the "pure" finite element domain (Ω_{FE}) we have $u|_{\Gamma_u} = 0$ and $u^s|_{\Gamma_u} = u|_{\Gamma_u} = 0$ so that the expression simplifies into the usual principle of virtual work [31].

5.2.3 Formulation in the "pure" finite element domain Ω_{FE}

In the domain $\{\Omega_{FE} : \bigcup \Omega^{(k)},\ \Omega^{(k)} \bigcap \Omega_{spheres} = \mathbf{0}\}$, where $\Omega^{(k)}$ is the finite element subdomain and $\Omega_{spheres}$ is the union of all spheres, the finite elements do not overlap with finite sphere, and considering $4-$node elements, the displacement field and strains are those

computed in the conventional finite element method [2]

$$\mathbf{u}_{\Omega_{FE}}(\mathbf{x}) = \sum_{I=1}^{4} \mathbf{H}_I^{FE}(\mathbf{x})\mathbf{u}_I, \tag{5.10}$$

$$\boldsymbol{\epsilon}_{\Omega_{FE}}(\mathbf{x}) = \sum_{I=1}^{4} \mathbf{B}_I^{FE}(\mathbf{x})\mathbf{u}_I, \tag{5.11}$$

where $\mathbf{u}_I^T = [u_I \ v_I]$ in which u_I and v_I are x- and y- directional nodal displacements respectively. The terms $\mathbf{H}_I^{FE}(\mathbf{x})$ and $\mathbf{B}_I^{FE}(\mathbf{x})$ are as follows:

$$\mathbf{H}_I^{FE}(\mathbf{x}) = \begin{bmatrix} h_I^{FE}(\mathbf{x}) & 0 \\ 0 & h_I^{FE}(\mathbf{x}) \end{bmatrix}, \tag{5.12}$$

$$\mathbf{B}_I^{FE}(\mathbf{x}) = \begin{bmatrix} h_{I,x}^{FE}(\mathbf{x}) & 0 \\ 0 & h_{I,y}^{FE}(\mathbf{x}) \\ h_{I,y}^{FE}(\mathbf{x}) & h_{I,x}^{FE}(\mathbf{x}) \end{bmatrix}, \tag{5.13}$$

where I denotes the index of nodes of finite elements. The force vector for the node I due to surface traction $\mathbf{f}^s$ on the kth element can be obtained as

$$\hat{\mathbf{f}}_I^{FE} = \int_{\Gamma_f \bigcap \partial\Omega_{FE}^{(k)}} \mathbf{H}_I^{FE^T} \mathbf{f}^s d\Gamma, \tag{5.14}$$

where

$$\mathbf{f}^s = \begin{bmatrix} f_x^s \\ f_y^s \end{bmatrix}. \tag{5.15}$$

5.2.4 Formulation in "pure" finite sphere domain Ω_{FS}

In the domain $\{\Omega_{FS} : \Omega \backslash (\Omega_{FE} \bigcup \Omega_{FE-FS})\}$, which we call pure finite sphere domain, the displacements and strains for the subdomain $\Omega_{FS}^{(k)}$ are [18]

$$\mathbf{u}_{\Omega_{FS}}(\mathbf{x}) = \sum_{J=1}^{N_{spheres}} \sum_{n \in \Im} \mathbf{H}_{Jn}^{FS}(\mathbf{x}) \boldsymbol{\alpha}_{Jn}, \tag{5.16}$$

$$\boldsymbol{\epsilon}_{\Omega_{FS}}(\mathbf{x}) = \sum_{J=1}^{N_{spheres}} \sum_{n \in \Im} \mathbf{B}_{Jn}^{FS}(\mathbf{x}) \boldsymbol{\alpha}_{Jn}, \tag{5.17}$$

where $N_{spheres}$ is the number of all the spheres, $\Im$ is an index set corresponding to m^{th} degree of freedom of I^{th} sphere, $\boldsymbol{\alpha}_{Jn} = [u_{Jn}\ v_{Jn}]$, $\underset{m=0,1,2}{\text{span}} \{p_m(\mathbf{x})\} = \{1, x, y\}$. Displacement interpolation matrix $\mathbf{H}_{Jn}^{FS}(\mathbf{x})$ and displacement-strain matrix $\mathbf{B}_{Jn}^{FS}(\mathbf{x})$ for finite sphere J with the degree of freedom n are

$$\mathbf{H}_{Jn}^{FS}(\mathbf{x}) = \begin{bmatrix} h_{Jn}^{FS}(\mathbf{x}) & 0 \\ 0 & h_{Jn}^{FS}(\mathbf{x}) \end{bmatrix}, \tag{5.18}$$

$$\mathbf{B}_{Jn}^{FS}(\mathbf{x}) = \begin{bmatrix} h_{Jn,x}^{FS}(\mathbf{x}) & 0 \\ 0 & h_{Jn,y}^{FS}(\mathbf{x}) \\ h_{I,y}^{FS}(\mathbf{x}) & h_{Jn,x}^{FS}(\mathbf{x}) \end{bmatrix}. \tag{5.19}$$

The force vector for the sphere I and local basis p_m due to surface traction $\mathbf{f}^s$ on the kth sphere is

$$\hat{\mathbf{f}}_{Im}^{FS} = \int_{\Gamma_f \bigcap \partial\Omega_{FS}^{(k)}} \mathbf{H}_{Im}^{FS^T} \mathbf{f}^s d\Gamma. \tag{5.20}$$

On the other hand, if the sphere corresponding to sphere I has nonzero intersection on the Dirichlet boundary, then we have

$$\hat{\mathbf{f}}_{Im}^{FS} = \sum_{J=1}^{N} \sum_{n \in \Im} \mathbf{KU}_{ImJn}^{FS} \boldsymbol{\alpha}_{Jn} - \mathbf{fU}_{Im}^{FS}, \tag{5.21}$$

where

$$\mathbf{KU}_{ImJn}^{FS} = \int_{\Gamma_u \bigcap B_I} \mathbf{H}_{Im}^{FS} \mathbf{NCB}_{Jn}^{FS} d\Gamma + \int_{\Gamma_u \bigcap B_I} \mathbf{B}_{Im}^{FS^T} \mathbf{CN}^T \mathbf{H}_{Jn}^{FS} d\Gamma \tag{5.22}$$

and

$$\mathbf{fU}_{Im}^{FS} = \int_{\Gamma_u \bigcap B_I} \mathbf{B}_{Im}^{FS^T} \mathbf{CN}^T \mathbf{u}^s d\Gamma. \tag{5.23}$$

5.2.5 Formulation in the coupled domain

In the domain of $\{\Omega_{FE-FS} : \bigcup \Omega^{(k)},\ \Omega^{(k)} \bigcap \Omega_{spheres} \neq \mathbf{0}\}$ which is the union of finite element domains, which have non-zero intersection with spheres, and we call it as Ω_{FE-FS}. The displacement field in the subdomain $\Omega_{FE-FS}^{(k)}$ consists of shape functions of $h_I^{FE-FS}(\mathbf{x})$ and $h_{Jn}^{FE-FS}(\mathbf{x})$ as

$$u_{\Omega_{FE-FS}}(\mathbf{x}) = \sum_{I=1}^{4} h_I^{FE-FS}(\mathbf{x}) u_I + \sum_{J=1}^{N_{spheres}} \sum_{n \in \Im} h_{Jn}^{FE-FS}(\mathbf{x}) u_{Jn}, \tag{5.24}$$

$$v_{\Omega_{FE-FS}}(\mathbf{x}) = \sum_{I=1}^{4} h_I^{FE-FS}(\mathbf{x}) v_I + \sum_{J=1}^{N_{spheres}} \sum_{n \in \Im} h_{Jn}^{FE-FS}(\mathbf{x}) v_{Jn}, \tag{5.25}$$

where the new shape functions are derived by Equations (5.2) and (5.3),

$$h_I^{FE-FS}(\mathbf{x}) = \frac{h_I(\mathbf{x})}{W^{(k)}}, \tag{5.26}$$

$$h_{Jn}^{FE-FS}(\mathbf{x}) = \frac{W_J(\mathbf{x})}{W^{(k)}}\, p_n(\mathbf{x}), \tag{5.27}$$

The strains in the domain $\Omega_{FE-FS}^{(k)}$ are

$$\epsilon_{xx}(\mathbf{x}) = \sum_{I=1}^{4} h_{I,x}^{FE-FS}(\mathbf{x}) u_I + \sum_{J=1}^{N_{spheres}} \sum_{n\in\Im} h_{Jn,x}^{FE-FS}(\mathbf{x}) u_{Jn} \tag{5.28}$$

$$\epsilon_{yy}(\mathbf{x}) = \sum_{I=1}^{4} h_{I,y}^{FE-FS}(\mathbf{x}) v_I + \sum_{J=1}^{N_{spheres}} \sum_{n\in\Im} h_{Jn,y}^{FE-FS}(\mathbf{x}) v_{Jn} \tag{5.29}$$

$$\begin{aligned}\gamma_{xy}(\mathbf{x}) = &\sum_{I=1}^{4} h_{I,y}^{FE-FS}(\mathbf{x}) u_I + \sum_{I=1}^{4} h_{I,x}^{FE-FS}(\mathbf{x}) v_I \\ &+ \sum_{J=1}^{N_{spheres}} \sum_{n\in\Im} h_{Jn,y}^{FE-FS}(\mathbf{x}) u_{Jn} + \sum_{J=1}^{N_{spheres}} \sum_{n\in\Im} h_{Jn,x}^{FE-FS}(\mathbf{x}) v_{Jn}\end{aligned} \tag{5.30}$$

In matrix form, this displacement and strain fields are expressed as

$$\mathbf{u}_{\Omega_{FE-FS}}(\mathbf{x}) = \sum_{I=1}^{4} \mathbf{H}_I^{FE-FS}(\mathbf{x}) \mathbf{u}_I + \sum_{J=1}^{N_{spheres}} \sum_{n\in\Im} \mathbf{H}_{Jn}^{FE-FS}(\mathbf{x}) \boldsymbol{\alpha}_{Jn} \tag{5.31}$$

$$\boldsymbol{\epsilon}_{\Omega_{FE-FS}}(\mathbf{x}) = \sum_{I=1}^{4} \mathbf{B}_I^{FE-FS}(\mathbf{x}) \mathbf{u}_I + \sum_{J=1}^{N_{spheres}} \sum_{n\in\Im} \mathbf{B}_{Jn}^{FE-FS}(\mathbf{x}) \boldsymbol{\alpha}_{Jn} \tag{5.32}$$

where the displacement matrix $\mathbf{H}_I^{FE-FS}(\mathbf{x})$ and strain-displacement matrix $\mathbf{B}_I^{FE-FS}(\mathbf{x})$ for node I are

$$\mathbf{H}_I^{FE-FS}(\mathbf{x}) = \begin{bmatrix} h_I^{FE-FS}(\mathbf{x}) & 0 \\ 0 & h_I^{FE-FS}(\mathbf{x}) \end{bmatrix}, \tag{5.33}$$

$$\mathbf{B}_I^{FE-FS}(\mathbf{x}) = \begin{bmatrix} h_{I,x}^{FE-FS}(\mathbf{x}) & 0 \\ 0 & h_{I,y}^{FE-FS}(\mathbf{x}) \\ h_{I,y}^{FE-FS}(\mathbf{x}) & h_{I,x}^{FE-FS}(\mathbf{x}) \end{bmatrix}, \tag{5.34}$$

and the displacement matrix $\mathbf{H}_{Jn}^{FE-FS}(\mathbf{x})$ and strain-displacement matrix $\mathbf{B}_{Jn}^{FE-FS}(\mathbf{x})$ for node J with degree of freedom n are

$$\mathbf{H}_{Jn}^{FE-FS}(\mathbf{x}) = \begin{bmatrix} h_{Jn}^{FE-FS}(\mathbf{x}) & 0 \\ 0 & h_{Jn}^{FE-FS}(\mathbf{x}) \end{bmatrix}, \tag{5.35}$$

$$\mathbf{B}_{Jn}^{FE-FS}(\mathbf{x}) = \begin{bmatrix} h_{Jn,x}^{FE-FS}(\mathbf{x}) & 0 \\ 0 & h_{Jn,y}^{FE-FS}(\mathbf{x}) \\ h_{Jn,y}^{FE-FS}(\mathbf{x}) & h_{Jn,x}^{FE-FS}(\mathbf{x}) \end{bmatrix}. \tag{5.36}$$

where the x- and y- derivatives of $h_I(\mathbf{x})$ are

$$h_{I,x}^{FE-FS}(\mathbf{x}) = \left[h_{I,x} - \frac{h_I}{W^{(k)}} \sum_{K=1}^{N^{(k)}} W_{K,x} \right] \frac{1}{W^{(k)}}, \tag{5.37}$$

$$h_{I,y}^{FE-FS}(\mathbf{x}) = \left[h_{I,y} - \frac{h_I}{W^{(k)}} \sum_{K=1}^{N^{(k)}} W_{K,y} \right] \frac{1}{W^{(k)}}, \tag{5.38}$$

The derivatives of $\rho_I(\mathbf{x})$ are

$$\rho_{I,x}^{FE-FS}(\mathbf{x}) = \left[W_{I,x} - \frac{W_I}{W^{(k)}} \sum_{K=1}^{N^{(k)}} W_{K,x} \right] \frac{1}{W^{(k)}}, \tag{5.39}$$

$$\rho_{I,y}^{FE-FS}(\mathbf{x}) = \left[W_{I,y} - \frac{W_I}{W^{(k)}} \sum_{K=1}^{N^{(k)}} W_{K,y} \right] \frac{1}{W^{(k)}}, \tag{5.40}$$

and

$$h_{Im,x}^{FE-FS}(\mathbf{x}) = \rho_{I,x}^{FE-FS}(\mathbf{x})p_m + \rho_I^{FE-FS}(\mathbf{x})p_{m,x}, \tag{5.41}$$

$$h_{Im,y}^{FE-FS}(\mathbf{x}) = \rho_{I,y}^{FE-FS}(\mathbf{x})p_m + \rho_I^{FE-FS}(\mathbf{x})p_{m,y}. \tag{5.42}$$

The individual stiffness values for the domain $\Omega_{FE-FS}^{(k)}$ can be obtained as

$$\mathbf{K}_{IJ}^{FE-FS} = \int_{\Omega_{FE-FS}^{(k)}} \mathbf{B}_I^{FE-FS^T}(\mathbf{x})\mathbf{C}\,\mathbf{B}_J^{FE-FS}(\mathbf{x})d\Omega, \tag{5.43}$$

$$\mathbf{K}_{IJn}^{FE-FS} = \int_{\Omega_{FE-FS}^{(k)}} \mathbf{B}_I^{FE-FS^T}(\mathbf{x})\mathbf{C}\,\mathbf{B}_{Jn}^{FE-FS}(\mathbf{x})d\Omega, \tag{5.44}$$

$$\mathbf{K}_{ImJ}^{FE-FS} = \int_{\Omega_{FE-FS}^{(k)}} \mathbf{B}_{Im}^{FE-FS^T}(\mathbf{x})\mathbf{C}\,\mathbf{B}_J^{FE-FS}(\mathbf{x})d\Omega, \tag{5.45}$$

$$\mathbf{K}_{ImJn}^{FE-FS} = \int_{\Omega_{FE-FS}^{(k)}} \mathbf{B}_{Im}^{FE-FS^T}(\mathbf{x})\mathbf{C}\,\mathbf{B}_{Jn}^{FE-FS}(\mathbf{x})d\Omega. \tag{5.46}$$

If the coupled subdomain has nonzero intersection on the Neumann boundary, The vector $\hat{\mathbf{f}}_I^{FE-FS}$ for the node I belonging to the coupled subdomain $\Omega_{FE-FS}^{(k)}$ is

$$\hat{\mathbf{f}}_I^{FE-FS} = \int_{\Gamma_f \bigcap \partial\Omega_{FE-FS}^{(k)}} \mathbf{H}_I^{FE-FS^T}(\mathbf{x})\mathbf{f}^s d\Gamma, \tag{5.47}$$

and the vector $\hat{\mathbf{f}}_{Im}^{FE-FS}$ for the m^{th} degree of freedom of node I belonging to the finite sphere on the $\Omega_{FE-FS}^{(k)}$ is

$$\hat{\mathbf{f}}_{Im}^{FE-FS} = \int_{\Gamma_f \bigcap \partial\Omega_{FE-FS}^{(k)}} \mathbf{H}_{Im}^{FE-FS^T}(\mathbf{x})\mathbf{f}^s d\Gamma. \tag{5.48}$$

On the other hand, if the sphere corresponding to sphere I has nonzero intersection on the Dirichlet boundary, then we have

$$\hat{\mathbf{f}}_{Im}^{FE-FS} = \sum_{J=1}^{N} \sum_{n \in \Im} \mathbf{KU}_{ImJn}^{FE-FS} \boldsymbol{\alpha}_{Jn} - \mathbf{fU}_{Im}^{FE-FS}, \tag{5.49}$$

where

$$\begin{aligned} \mathbf{KU}_{ImJn}^{FE-FS} = & \int_{\Gamma_u \bigcap \partial\Omega_{FE-FS}^{(k)}} \mathbf{H}_{Im}^{FE-FS} \mathbf{NCB}_{Jn}^{FE-FS} d\Gamma \\ & + \int_{\Gamma_u \bigcap \partial\Omega_{FE-FS}^{(k)}} \mathbf{B}_{Im}^{FE-FS^T} \mathbf{CN}^T \mathbf{H}_{Jn}^{FE-FS} d\Gamma \end{aligned} \tag{5.50}$$

and

$$\mathbf{fU}_{Im}^{FE-FS} = \int_{\Gamma_u \bigcap \partial\Omega_{FE-FS}^{(k)}} \mathbf{B}_{Im}^{FE-FS^T} \mathbf{CN}^T \mathbf{u}^s d\Gamma. \tag{5.51}$$

In the Equation (5.43), the index IJ means that the value represents the interaction with finite element node I and node J. The index IJn and ImJ means that the value has correlation with finite element node I and finite sphere J with nth mode. The index $ImJn$ means correlation with sphere I of mth mode and sphere J of nth mode.

It should be noted that when a finite element does not have any overlap with a sphere at an integration point, there is not any contribution from finite spheres. Therefore, in this specific case at the integration point the correlation terms ($\mathbf{K}_{ImJ}$,$\mathbf{K}_{IJn}$) between finite element nodes and finite spheres becomes zero and there is no contribution from any spheres.

5.2.6 Assemblage of stiffness matrix and force vector

The total strain energy in the first term of Equation (5.8) is the summation of strain energies in the domains of Ω_{FE}, Ω_{FS} and Ω_{FE-FS} as:

$$\int_{\Omega} \epsilon^T \mathbf{C} \epsilon d\Omega = \int_{\Omega_{FE}} \epsilon^T \mathbf{C} \epsilon d\Omega + \int_{\Omega_{FS}} \epsilon^T \mathbf{C} \epsilon d\Omega + \int_{\Omega_{FE-FS}} \epsilon^T \mathbf{C} \epsilon d\Omega. \tag{5.52}$$

By substituting Equations (5.11), (5.17) and (5.32) into Equation (5.52), we have

$$\int_{\Omega_{FE}} \epsilon^T \mathbf{C} \epsilon d\Omega = \mathbf{V} \left\{ \sum_{k \in \mathcal{M}} \int_{\Omega_{FE}} {\mathbf{B}_{FE}^{(k)}}^T \mathbf{C} \mathbf{B}_{FE}^{(k)} d\Omega^{(k)} \right\} \mathbf{U}, \tag{5.53}$$

$$\int_{\Omega_{FS}} \epsilon^T \mathbf{C} \epsilon d\Omega = \mathbf{V} \left\{ \sum_{k \in \mathcal{S}} \int_{\Omega_{FS}} {\mathbf{B}_{FS}^{(k)}}^T \mathbf{C} \mathbf{B}_{FS}^{(k)} d\Omega^{(k)} \right\} \mathbf{U}, \tag{5.54}$$

$$\int_{\Omega_{FE-FS}} \epsilon^T \mathbf{C} \epsilon d\Omega = \mathbf{V} \left\{ \sum_{k \in \mathcal{N}} \int_{\Omega_{FE-FS}} {\mathbf{B}_{FE-FS}^{(k)}}^T \mathbf{C} \mathbf{B}_{FE-FS}^{(k)} d\Omega^{(k)} \right\} \mathbf{U}, \tag{5.55}$$

where $\mathcal{M}$ is the index of the finite element subdomains, $\mathcal{N}$ is the index of the coupled subdomains, and $\mathcal{S}$ is the index of the pure finite sphere subdomains. substituting into Equation (5.52), the total stiffness matrix for the assemblage is obtained as:

$$\begin{aligned} \mathbf{K} = & \left\{ \sum_{k \in \mathcal{M}} \int_{\Omega_{FE}} {\mathbf{B}_{FE}^{(k)}}^T \mathbf{C} \mathbf{B}_{FE}^{(k)} d\Omega^{(m)} \right\} + \left\{ \sum_{k \in \mathcal{S}} \int_{\Omega_{FS}} {\mathbf{B}_{FS}^{(k)}}^T \mathbf{C} \mathbf{B}_{FS}^{(k)} d\Omega^{(k)} \right\} \\ & + \left\{ \sum_{k \in \mathcal{N}} \int_{\Omega_{FE-FS}} {\mathbf{B}_{FE-FS}^{(k)}}^T \mathbf{C} \mathbf{B}_{FE-FS}^{(k)} d\Omega^{(k)} \right\}. \end{aligned} \tag{5.56}$$

The discretized system corresponding to node $I \in \mathcal{M}$ is written as

$$\sum_{J \in \mathcal{L}} \mathbf{K}_{IJ} \mathbf{u}_J + \sum_{J \in \mathcal{K}} \sum_{n \in \Im} \mathbf{K}_{IJn} \boldsymbol{\alpha}_{Jn} = \mathbf{f}_I + \hat{\mathbf{f}}_I, \tag{5.57}$$

and the system equation corresponding to node $I \in \mathcal{N}$ with degree of freedom m is

$$\sum_{J \in \mathcal{L}} \mathbf{K}_{ImJ} \mathbf{u}_J + \sum_{J \in \mathcal{K}} \sum_{n \in \mathcal{S}} \mathbf{K}_{ImJn} \boldsymbol{\alpha}_{Jn} = \mathbf{f}_{Im} + \hat{\mathbf{f}}_{Im}, \tag{5.58}$$

where the terms of $\hat{\mathbf{f}}_I$ and $\hat{\mathbf{f}}_{Im}$ are considered when the subdomain has nonzero intersection with Γ_f as

$$\hat{\mathbf{f}}_I = \int_{\Gamma_f} \mathbf{H}_I \mathbf{f}^s d\Gamma, \tag{5.59}$$

$$\hat{\mathbf{f}}_{Im} = \int_{\Gamma_f} \mathbf{H}_{Im} \mathbf{f}^s d\Gamma. \tag{5.60}$$

On the other hand, when the coupled element has nonzero intersection with Γ_u, $\hat{\mathbf{f}}_I$ and $\hat{\mathbf{f}}_{Im}$ are

$$\hat{\mathbf{f}}_I = \sum_{J \in \mathcal{L}} \mathbf{K}\mathbf{U}_{IJ} \mathbf{u}_J + \sum_{J \in \mathcal{K}} \sum_{n \in \mathcal{S}} \mathbf{K}\mathbf{U}_{IJn} \boldsymbol{\alpha}_{Jn}, \tag{5.61}$$

$$\hat{\mathbf{f}}_{Im} = \sum_{J \in \mathcal{L}} \mathbf{K}\mathbf{U}_{ImJ} \mathbf{u}_J + \sum_{J \in \mathcal{K}} \sum_{n \in \mathcal{S}} \mathbf{K}\mathbf{U}_{ImJn} \boldsymbol{\alpha}_{Jn}. \tag{5.62}$$

It should be noted that the terms of $\hat{\mathbf{f}}_I$ and $\hat{\mathbf{f}}_{Im}$ are calculated as in Equations (5.61) and (5.62) only when the Γ_u has intersection with spheres, or the terms are ignored.

5.3 Imposing the Dirichlet boundary condition

In the finite element method, we can impose restraints on Γ_u by eliminating corresponding degrees of freedom at nodes since the shape function of the finite element formulation have

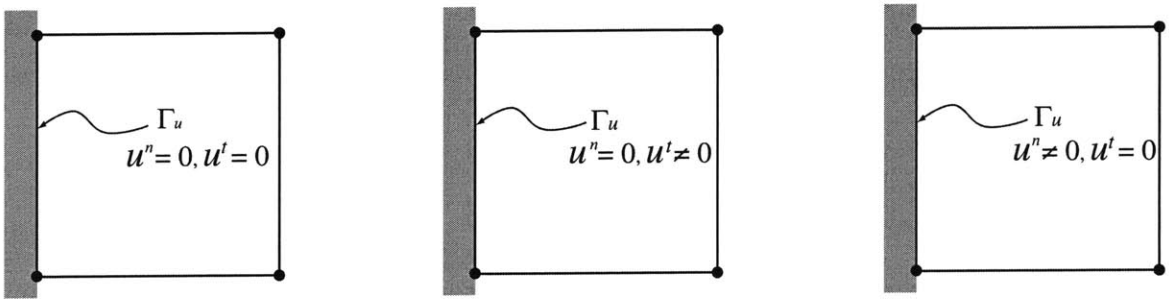

(a) (b) (c)

Figure 5-4: Various kinds of Dirichlet boundary conditions: (a) u^n and u^t are fixed, (b) u^n is fixed and u^t is free, and (c) u^n is freed and u^t is fixed.

the Kronecker delta property. However, the shape functions $h_{Im}(\mathbf{x})$ along the Dirichlet boundary of the coupling method have zero values at each nodes when m is not 0. Therefore, it is required to impose the Dirichlet boundary conditions more carefully.

We consider three cases: (a) u^n and u^t are fixed, (b) u^n is fixed and u^t is free, (c) u^n is free and u^t is fixed as illustrated in Figure 5-4. In this chapter, we describe how to impose the Dirichlet boundary condition for each case.

5.3.1 When the restraint is applied in both normal and tangential directions

We consider first the fixed displacement boundary condition $\mathbf{u} = 0$ on Γ_u.

$$\mathbf{KU}_{ImJn} = \int_{\Gamma_u} \mathbf{H}_{Im}^{FE-FS^T} \mathbf{NCB}_{Jn}^{FE-FS} d\Gamma + \int_{\Gamma_u} \mathbf{B}_{Im}^{FE-FS^T} \mathbf{CN}^T \mathbf{H}_{Jn}^{FE-FS} d\Gamma, \quad (5.63)$$

$$\mathbf{KU}_{IJn} = \int_{\Gamma_u} \mathbf{H}_{I}^{FE-FS^T} \mathbf{NCB}_{Jn}^{FE-FS} d\Gamma + \int_{\Gamma_u} \mathbf{B}_{I}^{FE-FS^T} \mathbf{CN}^T \mathbf{H}_{Jn}^{FE-FS} d\Gamma, \quad (5.64)$$

$$\mathbf{KU}_{IJ} = \int_{\Gamma_u} \mathbf{H}_{I}^{FE-FS^T} \mathbf{NCB}_{J}^{FE-FS} d\Gamma + \int_{\Gamma_u} \mathbf{B}_{I}^{FE-FS^T} \mathbf{CN}^T \mathbf{H}_{J}^{FE-FS} d\Gamma. \quad (5.65)$$

In the Equation (5.63), I and J are in $\mathcal{N}$. In Equation (5.64), I is in $\mathcal{N}$ and J is in $\mathcal{M}$. In Equation (5.65), both I and J are in $\mathcal{M}$ In the explicit form of Equation (5.63) to (5.65) we have

$$\begin{aligned}\mathbf{KU}_{ImJn}(1,1) &= h_{Im}^{FE-FS}\left\{C_{11}n_x h_{Jn,x}^{FE-FS} + C_{33}n_y h_{Jn,y}^{FE-FS}\right\} \\ &+ h_{Jn}^{FE-FS}\left\{C_{11}n_x h_{Im,x}^{FE-FS} + C_{33}n_y h_{Im,y}^{FE-FS}\right\},\end{aligned} \tag{5.66}$$

$$\begin{aligned}\mathbf{KU}_{ImJn}(2,1) &= h_{Im}^{FE-FS}\left\{C_{21}n_y h_{Jn,x}^{FE-FS} + C_{33}n_x h_{Jn,y}^{FE-FS}\right\} \\ &+ h_{Jn}^{FE-FS}\left\{C_{21}n_x h_{Im,y}^{FE-FS} + C_{33}n_y h_{Im,x}^{FE-FS}\right\},\end{aligned} \tag{5.67}$$

$$\begin{aligned}\mathbf{KU}_{ImJn}(1,2) &= h_{Im}^{FE-FS}\left\{C_{12}n_x h_{Jn,y}^{FE-FS} + C_{33}n_y h_{Jn,x}^{FE-FS}\right\} \\ &+ h_{Jn}^{FE-FS}\left\{C_{12}n_y h_{Im,x}^{FE-FS} + C_{33}n_x h_{Im,y}^{FE-FS}\right\},\end{aligned} \tag{5.68}$$

$$\begin{aligned}\mathbf{KU}_{ImJn}(2,2) &= h_{Im}^{FE-FS}\left\{C_{22}n_y h_{Jn,y}^{FE-FS} + C_{33}n_y h_{Jn,x}^{FE-FS}\right\} \\ &+ h_{Jn}^{FE-FS}\left\{C_{22}n_y h_{Im,y}^{FE-FS} + C_{33}n_x h_{Im,x}^{FE-FS}\right\}.\end{aligned} \tag{5.69}$$

Similarly, $\mathbf{KU}_{IJn}$ can be derived as

$$\begin{aligned}\mathbf{KU}_{IJn}(1,1) = h_I^{FE-FS}\left\{C_{11}n_x h_{Jn,x}^{FE-FS} + C_{33}n_y h_{Jn,y}^{FE-FS}\right\} \\ + h_{Jn}^{FE-FS}\left\{C_{11}n_x h_{I,x}^{FE-FS} + C_{33}n_y h_{I,y}^{FE-FS}\right\},\end{aligned} \tag{5.70}$$

$$\begin{aligned}\mathbf{KU}_{IJn}(2,1) = h_I^{FE-FS}\left\{C_{21}n_y h_{Jn,x}^{FE-FS} + C_{33}n_x h_{Jn,y}^{FE-FS}\right\} \\ + h_{Jn}^{FE-FS}\left\{C_{21}n_x h_{I,y}^{FE-FS} + C_{33}n_y h_{I,x}^{FE-FS}\right\},\end{aligned} \tag{5.71}$$

$$\begin{aligned}\mathbf{KU}_{IJn}(1,2) = h_I^{FE-FS}\left\{C_{12}n_x h_{Jn,y}^{FE-FS} + C_{33}n_y h_{Jn,x}^{FE-FS}\right\} \\ + h_{Jn}^{FE-FS}\left\{C_{12}n_y h_{I,x}^{FE-FS} + C_{33}n_x h_{I,y}^{FE-FS}\right\},\end{aligned} \tag{5.72}$$

$$\begin{aligned}\mathbf{KU}_{IJn}(2,2) = h_I^{FE-FS}\left\{C_{22}n_y h_{Jn,y}^{FE-FS} + C_{33}n_y h_{Jn,x}^{FE-FS}\right\} \\ + h_{Jn}^{FE-FS}\left\{C_{22}n_y h_{I,y}^{FE-FS} + C_{33}n_x h_{I,x}^{FE-FS}\right\}.\end{aligned} \tag{5.73}$$

Also,

$$\begin{aligned}\mathbf{KU}_{IJ}(1,1) = h_I^{FE-FS}\left\{C_{11}n_x h_{J,x}^{FE-FS} + C_{33}n_y h_{J,y}^{FE-FS}\right\} \\ + h_J^{FE-FS}\left\{C_{11}n_x h_{I,x}^{FE-FS} + C_{33}n_y h_{I,y}^{FE-FS}\right\},\end{aligned} \tag{5.74}$$

$$\begin{aligned}\mathbf{KU}_{IJ}(2,1) = h_I^{FE-FS}\left\{C_{21}n_y h_{J,x}^{FE-FS} + C_{33}n_x h_{J,y}^{FE-FS}\right\} \\ + h_J^{FE-FS}\left\{C_{21}n_x h_{I,y}^{FE-FS} + C_{33}n_y h_{I,x}^{FE-FS}\right\},\end{aligned} \tag{5.75}$$

$$\begin{aligned}\mathbf{KU}_{IJ}(1,2) = h_I^{FE-FS}\left\{C_{12}n_x h_{J,y}^{FE-FS} + C_{33}n_y h_{J,x}^{FE-FS}\right\} \\ + h_J^{FE-FS}\left\{C_{12}n_y h_{I,x}^{FE-FS} + C_{33}n_x h_{I,y}^{FE-FS}\right\},\end{aligned} \tag{5.76}$$

$$\begin{aligned}\mathbf{KU}_{IJ}(2,2) = h_I^{FE-FS}\left\{C_{22}n_y h_{J,y}^{FE-FS} + C_{33}n_y h_{J,x}^{FE-FS}\right\} \\ + h_J^{FE-FS}\left\{C_{22}n_y h_{I,y}^{FE-FS} + C_{33}n_x h_{I,x}^{FE-FS}\right\}.\end{aligned} \tag{5.77}$$

5.3.2 When the restraint is applied only in the normal direction or the tangential direction

When the restraint condition is a roller support as shown in Figure 5-4 (b) and (c), only the normal or the tangential direction movement is suppressed. Therefore, we need to consider special handling for the imposition of these boundary conditions.

We can rewrite the second term of Equation (5.8) as

$$\int_{\Gamma_u} \left[\boldsymbol{\epsilon}^T(\mathbf{v})\mathbf{C}\mathbf{N}^T\mathbf{u} + \mathbf{v}^T\mathbf{N}\mathbf{C}\boldsymbol{\epsilon}(\mathbf{u})\right] d\Gamma = \int_{\Gamma_u} \mathbf{f}^u(\mathbf{v})\mathbf{u} + \mathbf{f}^u(\mathbf{u})\mathbf{v} d\Gamma. \tag{5.78}$$

Using force and displacement terms, we can decompose the force term into normal and tangential components. The surface traction term $\mathbf{f}^u$ due to the Dirichlet boundary condition can be decomposed into normal and tangential components as

$$\mathbf{f}^u = f_n^u\mathbf{n} + f_t^u\mathbf{t}, \tag{5.79}$$

where f_n^u is the normal traction and f_t^u is tangential traction, normal directional vector $\mathbf{n} = [n_x \; n_y]^T$ and tangential directional vector $\mathbf{t} = [-n_y \; n_x]^T$. Here we can calculate f_n^u and f_n^t as

$$\mathbf{f}^u = \boldsymbol{\sigma} \cdot \mathbf{n} \tag{5.80}$$

$$f_n^u = (\boldsymbol{\sigma} \cdot \mathbf{n}) \cdot \mathbf{n} \tag{5.81}$$

$$f_t^u = (\boldsymbol{\sigma} \cdot \mathbf{n}) \cdot \mathbf{t} \tag{5.82}$$

where Cauchy stress tensor matrix is

$$\boldsymbol{\sigma} = \begin{bmatrix} \sigma_{11} & \sigma_{12} \\ \sigma_{21} & \sigma_{22} \end{bmatrix}. \tag{5.83}$$

The displacement field also can be decomposed into normal directional displacement u_n and tangential directional displacement u_t as

$$\mathbf{u}^u = u_n \mathbf{n} + u_t \mathbf{t}. \tag{5.84}$$

Substituting Equations (5.81) and (5.82) into Equation (5.78), we obtain

$$\begin{aligned} \int_{\Gamma_u} \boldsymbol{\epsilon}^T(\mathbf{v}) \mathbf{C} \mathbf{N}^T \mathbf{u} + \mathbf{v}^T \mathbf{N} \mathbf{C} \boldsymbol{\epsilon}(\mathbf{u}) d\Gamma = & \int_{\Gamma_u} f_n^u(v) u_n + f_t^u(v) u_t d\Gamma \\ & + \int_{\Gamma_u} f_n^u(u) v_n + f_t^u(u) v_t d\Gamma \end{aligned} \tag{5.85}$$

The integrand terms in the Equation (5.85) can be classified into normal and tangential direction terms. The first two terms on the right hand side are transformed as

$$f_n^u(v) u_n = \mathbf{V}^T \mathbf{B}^T \mathbf{C} \mathbf{N}^T \mathbf{n} \mathbf{n}^T \mathbf{H} \mathbf{U} \tag{5.86}$$

$$f_t^u(v) u_t = \mathbf{V}^T \mathbf{B}^T \mathbf{C} \mathbf{N}^T \mathbf{t} \mathbf{t}^T \mathbf{H} \mathbf{U} \tag{5.87}$$

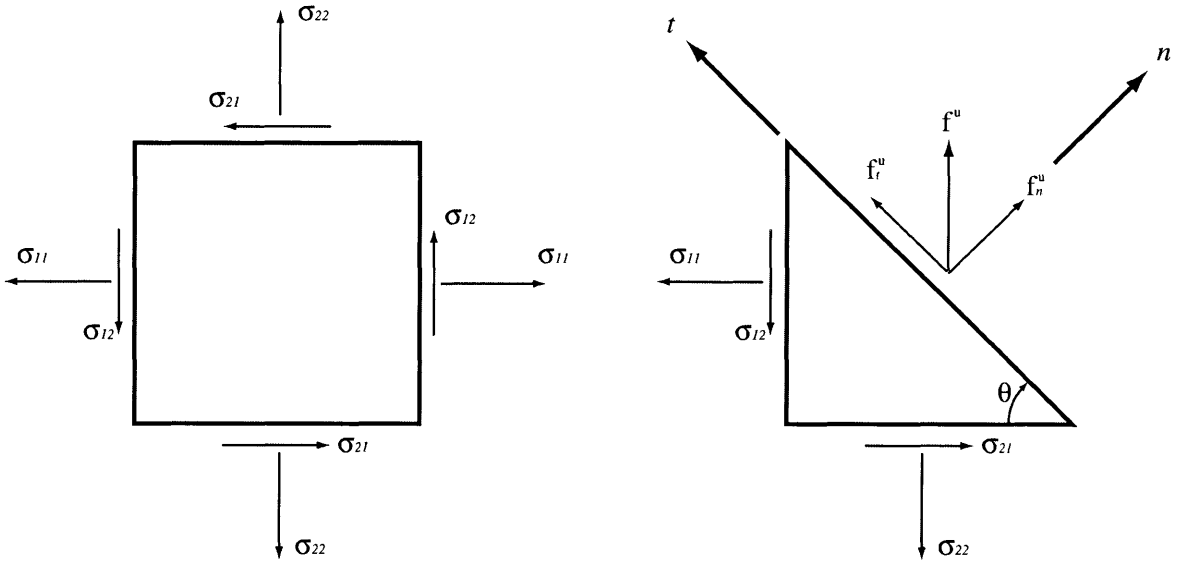

Figure 5-5: Stresses on the inclined surface. n is normal vector to the inclined surface and t is tangential direction vector.

The last two terms on the right hand side are

$$f_n^u(u)v_n = \mathbf{V}^T\mathbf{H}\mathbf{n}\mathbf{n}^T\mathbf{N}\mathbf{C}\mathbf{B}\mathbf{U}, \tag{5.88}$$

$$f_t^u(u)v_t = \mathbf{V}^T\mathbf{H}\mathbf{t}\mathbf{t}^T\mathbf{N}\mathbf{C}\mathbf{B}\mathbf{U}, \tag{5.89}$$

where $\mathbf{B}$ can be either $\mathbf{B}_I$ or $\mathbf{B}_{Im}$, and also $\mathbf{H}$ can be $\mathbf{H}_I$ or $\mathbf{H}_{Im}$ according to the corresponding degree of freedom.

In matrix form, Equation (5.85) can be rewritten as

$$\mathbf{K}\mathbf{U} = \mathbf{K}\mathbf{U}^n + \mathbf{K}\mathbf{U}^t, \tag{5.90}$$

where $\mathbf{K}\mathbf{U}^n$ is contributed by the normal directional displacement on Γ_u and $\mathbf{K}\mathbf{U}^t$ by the

tangential directional displacement.

$$\mathbf{KU}_{ImJn} = \mathbf{KU}^n_{ImJn} + \mathbf{KU}^t_{ImJn}. \tag{5.91}$$

For the sphere I and sphere J corresponding to the degree of freedom m and n, we have

$$\mathbf{KU}_{ImJn} = \mathbf{KU}^n_{ImJn} + \mathbf{KU}^t_{ImJn}, \tag{5.92}$$

where

$$\mathbf{KU}^n_{ImJn} = \int_{\Gamma_u} \mathbf{B}^T_{Im}\mathbf{C}\mathbf{n}\mathbf{n}^T\mathbf{H}_{Jn}d\Gamma + \int_{\Gamma_u} \mathbf{H}^T_{Im}\mathbf{n}\mathbf{n}^T\mathbf{C}\mathbf{B}_{Jn}d\Gamma, \tag{5.93}$$

$$\mathbf{KU}^t_{ImJn} = \int_{\Gamma_u} \mathbf{B}^T_{Im}\mathbf{C}\mathbf{t}\mathbf{t}^T\mathbf{H}_{Jn}d\Gamma + \int_{\Gamma_u} \mathbf{H}^T_{Im}\mathbf{t}\mathbf{t}^T\mathbf{C}\mathbf{B}_{Jn}d\Gamma. \tag{5.94}$$

5.4 Enriching the finite element functions

When we do not have a pure finite sphere domain as illustrated in Figure 5-2, we can simply use the scheme to enrich the finite element functions. Since finite element shape functions satisfy the partition of unity principle already, it is possible to add spheres adaptively. Then the equations for the shape functions in Ω_{FE-FS} are of the forms

$$h^{FE-FS}_I(\mathbf{x}) = h_I, \qquad I = 1, 2, \ldots, N, \tag{5.95}$$

$$\rho^{FE-FS}_I(\mathbf{x}) = W_I, \qquad I = 1, 2, \ldots, N, \tag{5.96}$$

$$h^{FE-FS}_{Im}(\mathbf{x}) = \rho^{FE-FS}_I(\mathbf{x})p_m(\mathbf{x}). \tag{5.97}$$

And the displacement fields in the coupled subdomains can be approximate by the equations of

$$u^{(k)}_{\Omega_{FE-FS}}(\mathbf{x}) = \sum_{I=1}^{4} h_I^{FE-FS}(\mathbf{x}) u_I + \sum_{J=1}^{N^{(k)}_{spheres}} \sum_{n \in \Im} h_{Jn}^{FE-FS}(\mathbf{x}) u_{Jn}, \tag{5.98}$$

$$v^{(k)}_{\Omega_{FE-FS}}(\mathbf{x}) = \sum_{I=1}^{4} h_I^{FE-FS}(\mathbf{x}) v_I + \sum_{J=1}^{N^{(k)}_{spheres}} \sum_{n \in \Im} h_{Jn}^{FE-FS}(\mathbf{x}) v_{Jn}. \tag{5.99}$$

Since $\sum_{I=1}^{4} h_I(\mathbf{x}) = 1$ even without h_{Jn} term, the partition of unity is satisfied and the approximation is complete. We add more shape function h_{Jn} on top of these bases. The shape functions of spheres simply enrich the functions of the classical finite elements. The total stiffness matrix consists of coupled domain integration and finite element domain integrations as

$$\begin{aligned} \mathbf{K} = & \left\{ \sum_{k \in \mathcal{M}} \int_{\Omega_{FE}} {\mathbf{B}^{(k)}_{FE}}^T \mathbf{C} \mathbf{B}^{(k)}_{FE} d\Omega^{(m)} \right\} \\ & + \left\{ \sum_{k \in \mathcal{N}} \int_{\Omega_{FE-FS}} {\mathbf{B}^{(k)}_{FE-FS}}^T \mathbf{C} \mathbf{B}^{(k)}_{FE-FS} d\Omega^{(k)} \right\}, \end{aligned} \tag{5.100}$$

where $\mathcal{M}$ is the index of the finite element subdomains, $\mathcal{N}$ is the index of the coupled subdomains.

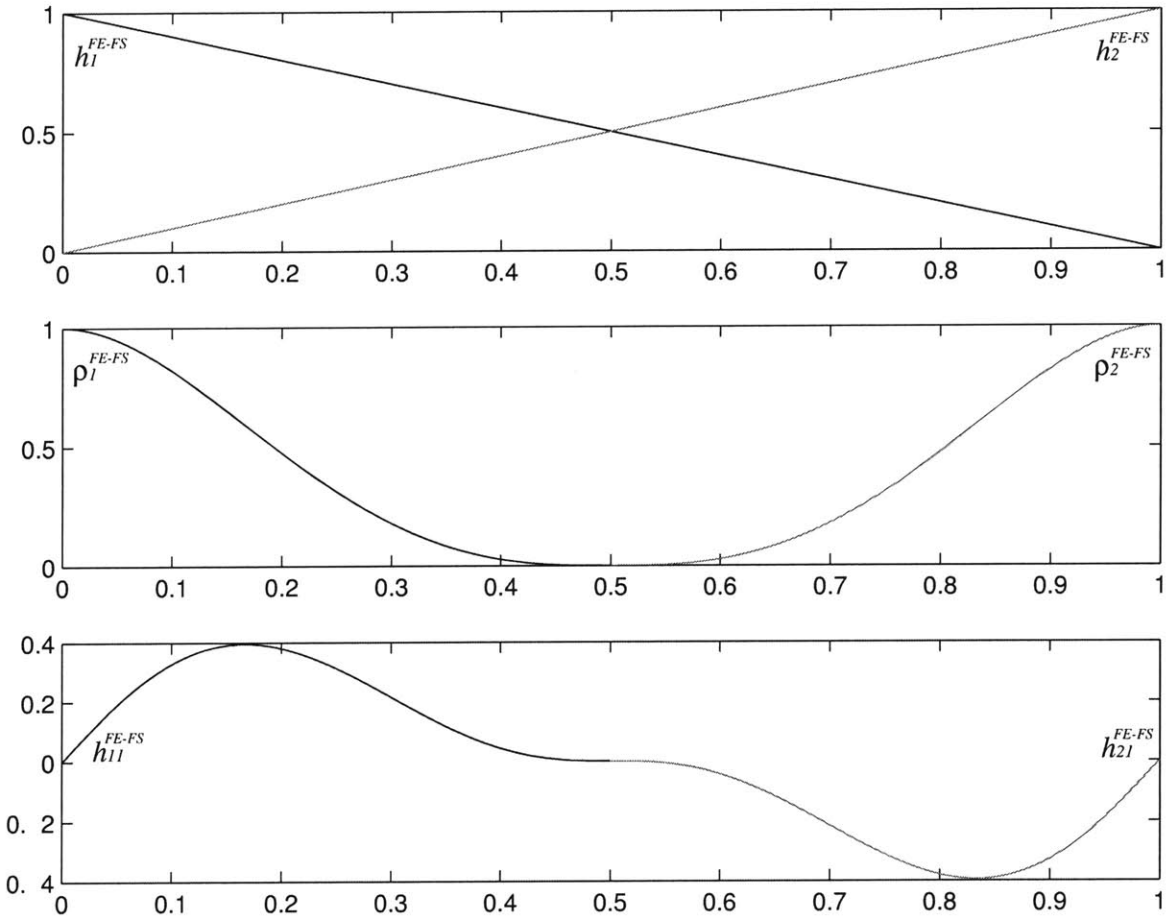

Figure 5-6: Shape functions $h_1^{FE-FS}(x)$, $h_2^{FE-FS}(x)$, $\rho_1^{FE-FS}(x)$, $\rho_2^{FE-FS}(x)$, $h_{11}^{FE-FS}(x)$, and $h_{21}^{FE-FS}(x)$ in a 1-dimensional case when the spheres are located at the both ends, where $R_1, R_2 = 0.5$.

Chapter 6

Examples of Coupling Methods

6.1 Tension and bending test of coupled elements.

6.1.1 Test geometry and loading conditions

A simple plate was modelled by coupling scheme. We consider the various loading cases such as tension and moment shown in Figure 6-1. Restraints are applied to eliminate all rigid body displacements at the left end of the plate, and simple tension and moment are applied respectively. Two scenarios for the arrangement of spheres were introduced as in Figure 6-2. In the Figure 6-2 (a) two spheres are located on the right of the each element and in Figure 6-2 (b) four spheres are arranged on the nodes of the each element.

To simulate mesh refinement, we divided the element into half at each case as illustrated in Figure 6-3, one FEM element is used in (a) and half of the plate of the original shape is considered having load applied on the right side of the model in (b). Similarly, more refinements are implemented in Figure 6-3 (c) to (e). For the calculation of strain energy,

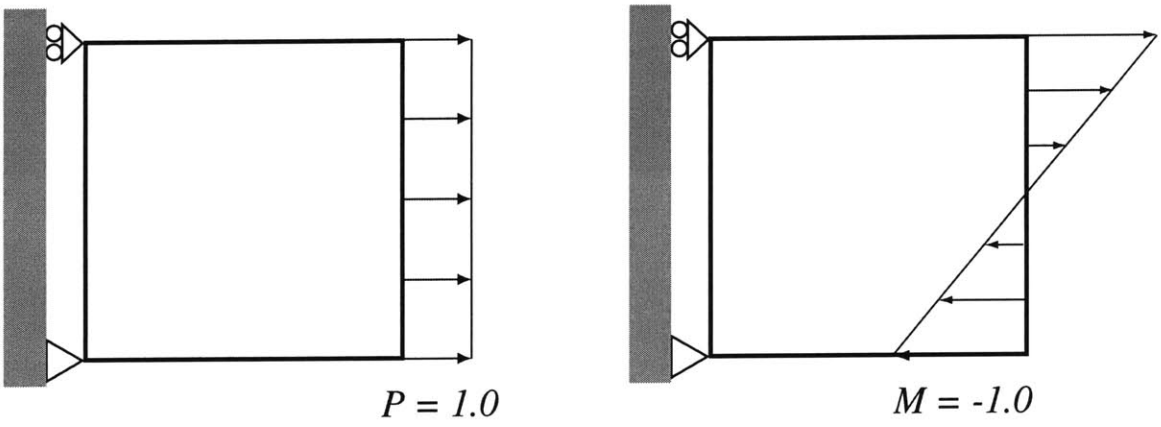

(a) Tension (b) Moment

Figure 6-1: Loading conditions for patch test of the coupling scheme. (a) unit tensile stress and (b) linear pressure distribution resulting in unit moment load are applied on the right end of the plate. For the material properties, $E = 100$ and $\nu = 0.3$. Element is under the plane strain condition

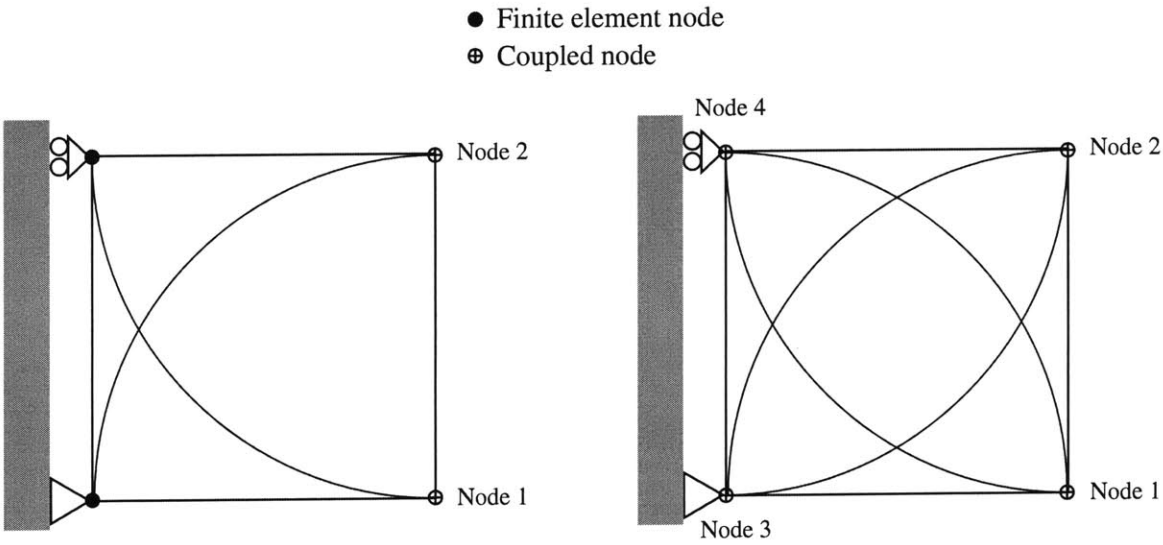

(a) (b)

Figure 6-2: Sphere arrangements on a 4-node element. (a) Two spheres are located on the right side of 4-node element and (b) four spheres are placed on each node of4-node element. The coupled node means that it contains finite element node and finite sphere node simultaneously.

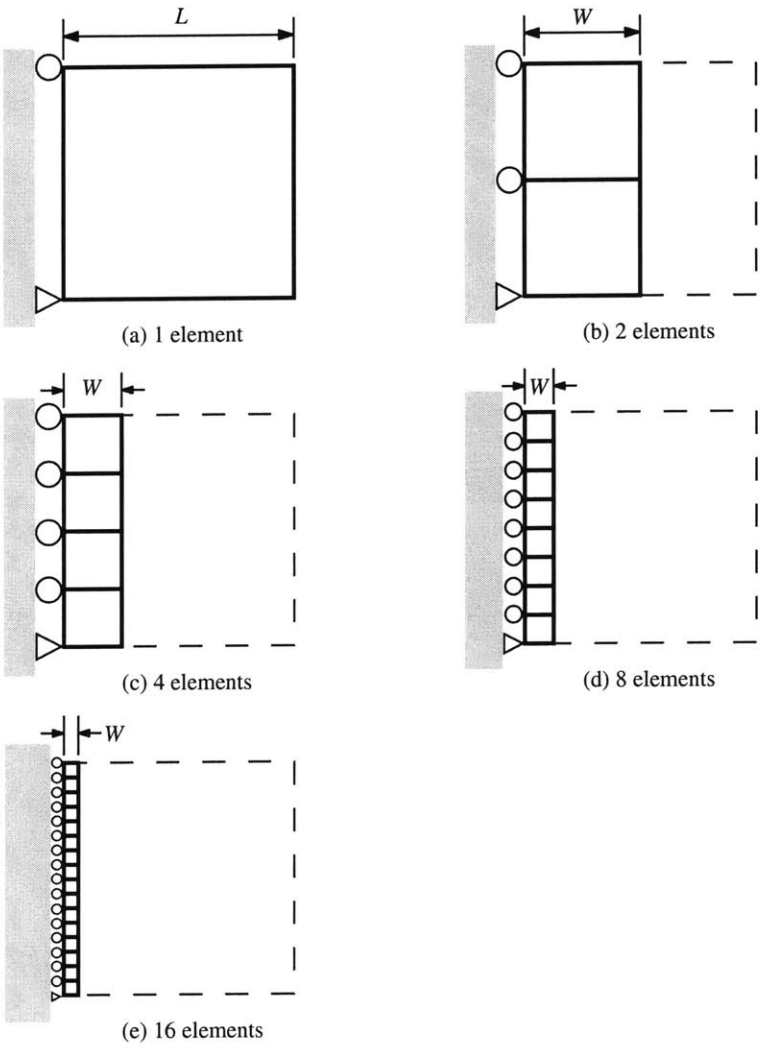

Figure 6-3: Element refinements. (a) 1 element, (b) 2 elements, (c) 4 elements, (d) 8 elements, and (e) 16 elements are employed. L is the original length of the plate. W is the width of the plate with refinements.

we use the factor (L/W) to make the equivalent strain energy corresponding the case (a). The radius of sphere is same with the length of a side of the plate (W).

6.1.2 Tension and bending test result of a simple plate

The results with the given geometry and loading condition for the coupled element are summarized in Table 6.1, and the convergence curve is in Figure 6-4. As expected, with more coupled elements, the strain energy increases and approaches to the exact value when the moment is applied to the plate. For the tensional loading, even with one element, the strain energy is close to the exact value because the 4-node element has capability to describe the constant strain and stress completely.

Comparing the strain energy in the 2-sphere case-scheme (a) and the 4-sphere case-scheme (b) in Figure 6-2, when we employ sphere on each node, the strain energy is closer to the exact value in the 4-sphere case with the same distribution of FEM elements. This result matches the theoretical principles. In the test, the result shows that the coupling scheme is better than using only 4-node elements to simulate the physical problems more accurately.

6.2 Specialized examples

Abrupt changes in cross section give rise to great irregularities in stress distributions. These irregularities are of particular importance in the design of machine parts subjected to external forces and pressures. Irregularity of stress distributions at such regions means that at certain points the stress is far above the average value and cracks are likely to start. The

1 Element					
Scheme (a)			Scheme (b)		
Load	**SE**	**EQUIV SE**	**Load**	**SE**	**EQUIV SE**
T	0.0045500611	0.0045500611	T	0.0045503951	0.0045503951
M	0.0457473490	0.0457473490	B	0.0508169452	0.0508169452
2 Element					
Scheme (a)			Scheme (b)		
Load	**SE**	**EQUIV SE**	**Load**	**SE**	**EQUIV SE**
T	0.0022750284	0.0045500568	T	0.0022751804	0.0045503608
M	0.0260481890	0.0520963780	B	0.0267831226	0.0535662450
4 Element					
Scheme (a)			Scheme (b)		
Load	**SE**	**EQUIV SE**	**Load**	**SE**	**EQUIV SE**
T	0.0011375132	0.0045500526	T	0.0011375758	0.0045502994
M	0.0134871536	0.0539486144	B	0.0135776276	0.0543105104
8 Element					
Scheme (a)			Scheme (b)		
Load	**SE**	**EQUIV SE**	**Load**	**SE**	**EQUIV SE**
T	0.0005687563	0.0045500504	T	0.0005687833	0.0045502664
M	0.0068043401	0.0544347208	B	0.0068161832	0.0545294656
16 Element					
Scheme (a)			Scheme (b)		
Load	**SE**	**EQUIV SE**	**Load**	**SE**	**EQUIV SE**
T	0.0002843781	0.0045500496	T	0.0002843910	0.0045502560
M	0.0034099232	0.0545587712	B	0.0034115350	0.0545845603

Table 6.1: Strain energy of coupled elements in tension and moment. Scheme (a) represents two sphere allocation on the right side and scheme (b) means four sphere allocation on each node of 4-node element as shown in Figure 6-2. **T** means tension and **M** means moment. We consider the plane strain condition, $E = 100$ and $\nu = 0.3$. The equivalent strain energy is calculated by multiplying number of elements. The exact strain energy for tensional loading is 0.00455 and for bending is 0.0546.

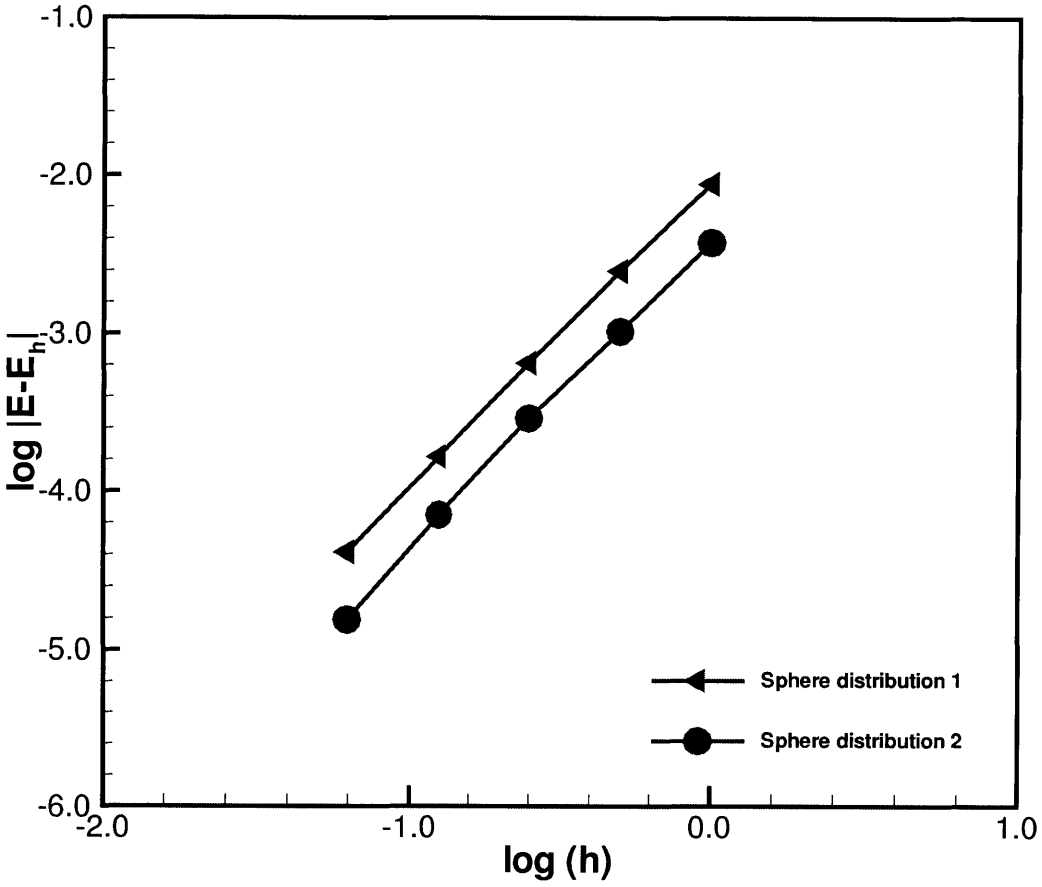

Figure 6-4: Convergence curves with different sphere allocations shown in Figure 6-2.

coupling scheme has advantage to depict these kinds of local irregularities since the finite sphere shape functions are added locally. In this section, we show some example related to stress concentrations such as plate with a hole and plate with a sharp crack. In the traditional finite element method, a spatially nonisotropic elements are employed in fracture mechanics fields. Since it is known that specific stress singularities exist at crack tips, the use of finite elements that contain the required stress singularities can be effective [2]. Various elements have been designed and developed, but very simple and attractive elements can be obtained by distorting the higher-order isoparametric elements.

6.2.1 Plate with a hole

If there is a small circular hole [1] subjected to a uniform pressure as shown in Figure 6-5, a high stress concentration occurs. The theory shows that the stress concentration is of very localized characteristic and is confined to the immediate vicinity of the hole. For the case of $5 < b/a < 8$ the results of the approximate calculation agree closely with the exact solution. However, for the case of $b/a < 5$ the hole cannot be considered very small and the basic assumption for the analytical calculation is not satisfied sufficiently [32]. To explain the stress concentration phenomenon more systematically, we need to understand the stress concentration factors. The stress concentration factor is defined as the ratio of the peak stress in the body to a reference stress. Usually the stress concentration factor is K_{tg}, for which the reference stress is based on the gross cross-sectional area, or K_{tn}, for which the reference stress is based on the net cross-sectional area. For a two-dimensional element

[1] The diameter of the hole is less than one-fifth of the width of the plate.

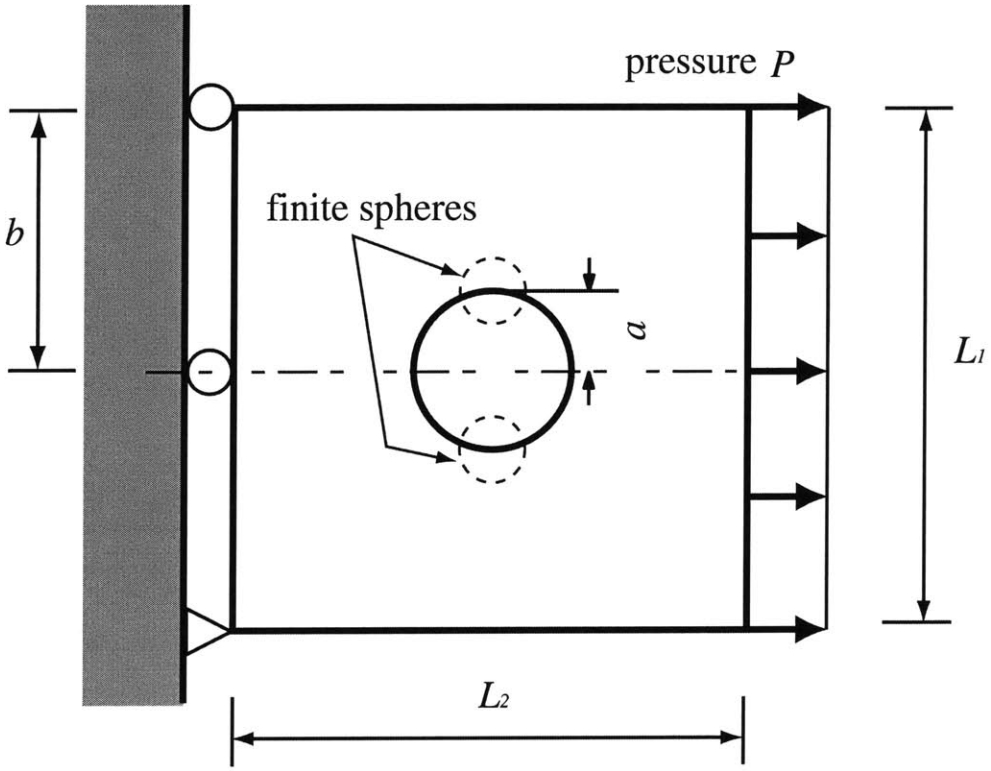

Figure 6-5: Geometry of a plate with a hole in the middle of the plate. a is the radius of the hole, b is the half of the width (L_1) of the plate L_2 is the length of the plate and $d = 2a$ is the diameter of the hole. The plate is subjected to lateral tensile pressure P under the plane stress condition.

with a single hole, the formula for these stress concentration factors is

$$\sigma_{max} = K_{tg} \times \sigma \tag{6.1}$$

where K_{tg} is the stress concentration factor based on gross stress, σ_{max} is the maximum stress, at the edge of the hole, σ is the stress on gross section far from the hole. The stress concentration factor K_{tg} can be obtained by the equation

$$K_{tg} = 0.284 + \frac{2}{1 - \frac{d}{H}} - 0.600\left(1 - \frac{d}{H}\right) + 1.32\left(1 - \frac{d}{H}\right)^2 \tag{6.2}$$

The relation with σ_{max} and σ is

$$\sigma_{max} = K_{tn} \times \sigma_n \tag{6.3}$$

where K_{tn} is the stress concentration factor based on net (nominal) stress and σ_n is the net stress $\sigma/(1 - d/H)$ [33]. The equation to calculate K_{tn} is

$$K_{tn} = 2 + \frac{2}{1 - \frac{d}{H}} - 0.284\left(1 - \frac{d}{H}\right) - 0.600\left(1 - \frac{d}{H}\right)^2 + 1.32\left(1 - \frac{d}{H}\right)^3 \tag{6.4}$$

We consider a plate with a hole which has $b = 3.0$, $a = 0.3$, $L_1 = 6$, and $L_2 = 6$. By applying the Equations (6.2) to calculate the stress concentration factor shown in Figure 6-6, the value of K_{tg} is 3.0354. When we analyze with very fine mesh refinement as shown in Figure 6-7, 4096 9-node elements were employed for the finite element analysis and the maximum stress value σ_{xx} is 3.008. This result is reasonably close to the analytical value

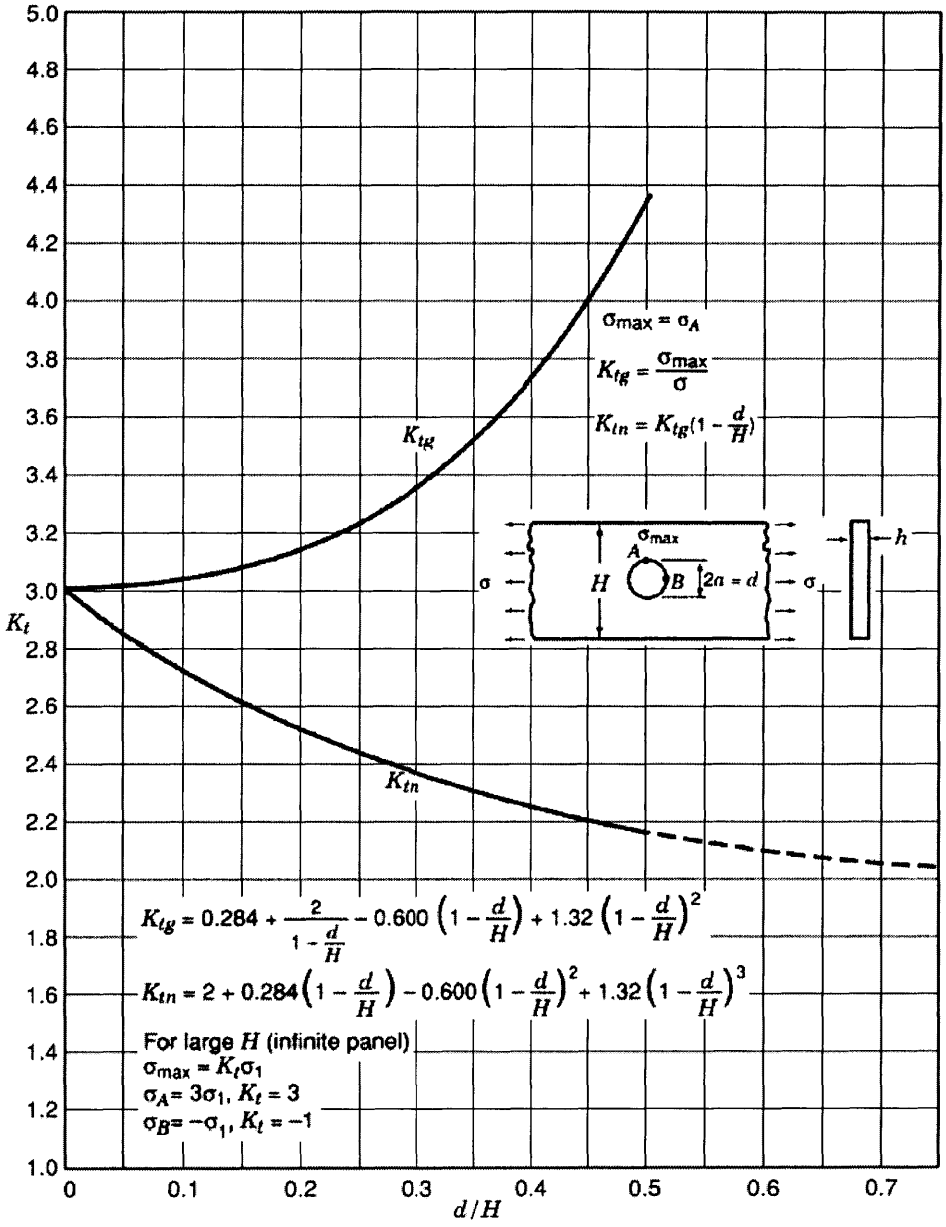

Figure 6-6: Stress concentration factors K_{tg} and K_{tn} for the tension of a finite-width thin plate with a circular hole (Rowland 1929-30).

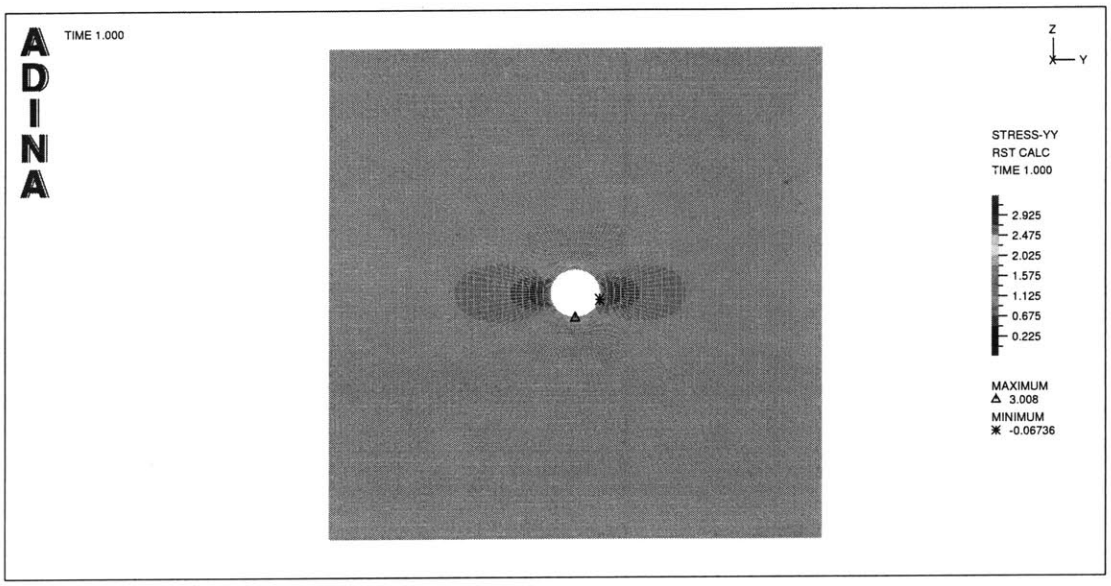

Figure 6-7: ADINA result: 4096 9-node elements are used. Stress (σ_{xx}) concentration at the vicinity of the hole can be observed. The plate has the geometry, boundary condition and loading condition in Figure 6-5. The Young's modulus is 100 and Poisson ratio is 0.3. in the plane strain condition. The maximum stress in horizontal direction is 3.008.

of maximum stress σ_{xx}. Therefore, we assume that the FEM solution is the exact value and compare the results.

With 16, 64 and 256 elements respectively, we implemented the enriching scheme. As listed in Table6.2, finite element method using $4-$node elements yields the smallest values, and the enriching scheme gives us better results than $9-$node elements.

For the implementation of the enriching scheme, we placed two spheres on the top and bottom of the hole respectively since it is expected to have stress concentration at those points. The comparison of the maximum stress value is summarized in Table 6.2.

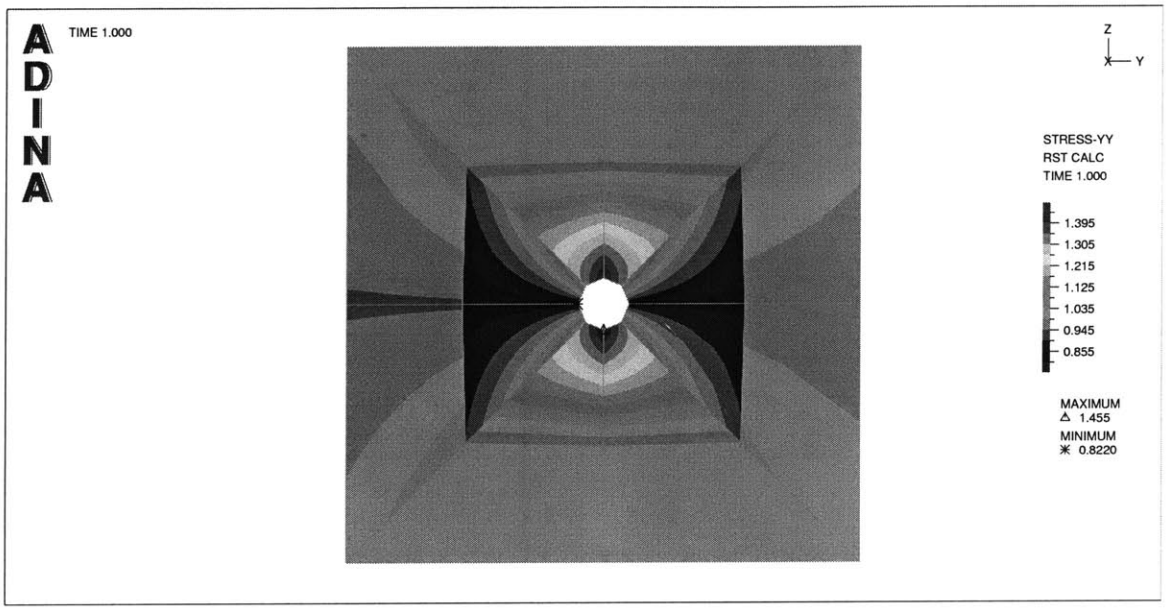

Figure 6-8: Stress (σ_{xx}) concentration at the vicinity of the hole. The plate has the geometry, boundary condition and loading condition in Figure 6-5. The Young's modulus is 100 and Poisson ratio is 0.3 under the plane stress condition. 16 elements (4-nodes) are used.

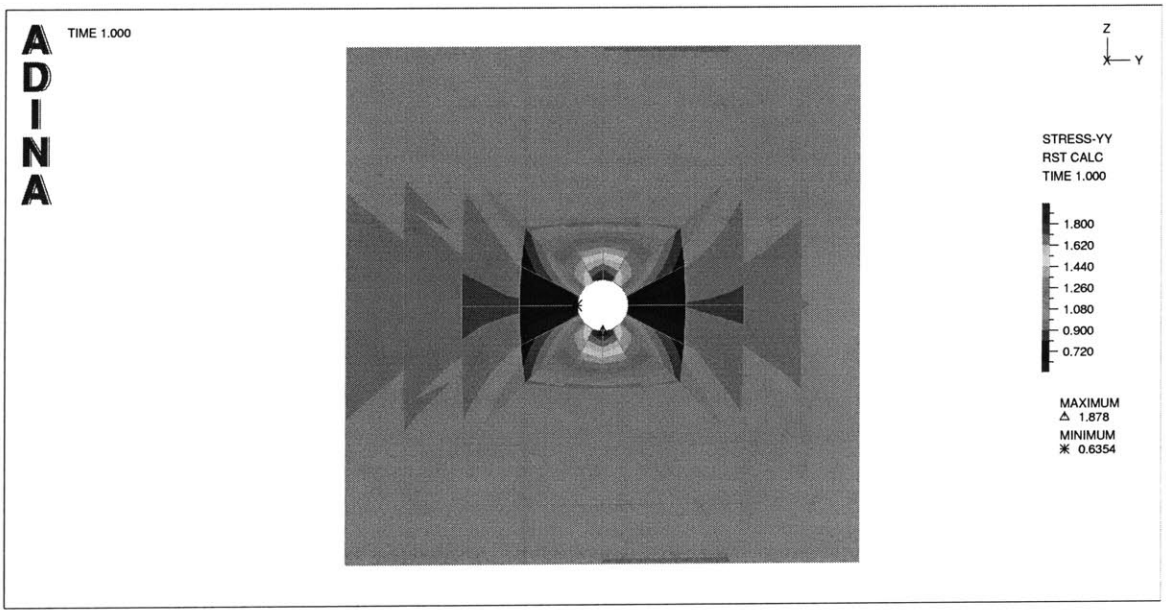

Figure 6-9: Stress (σ_{xx}) concentration at the vicinity of the hole. The plate has the geometry, boundary condition and loading condition in Figure 6-5. The Young's modulus is 100 and Poisson ratio is 0.3 under the plane stress condition. 64 elements (4-nodes) are used.

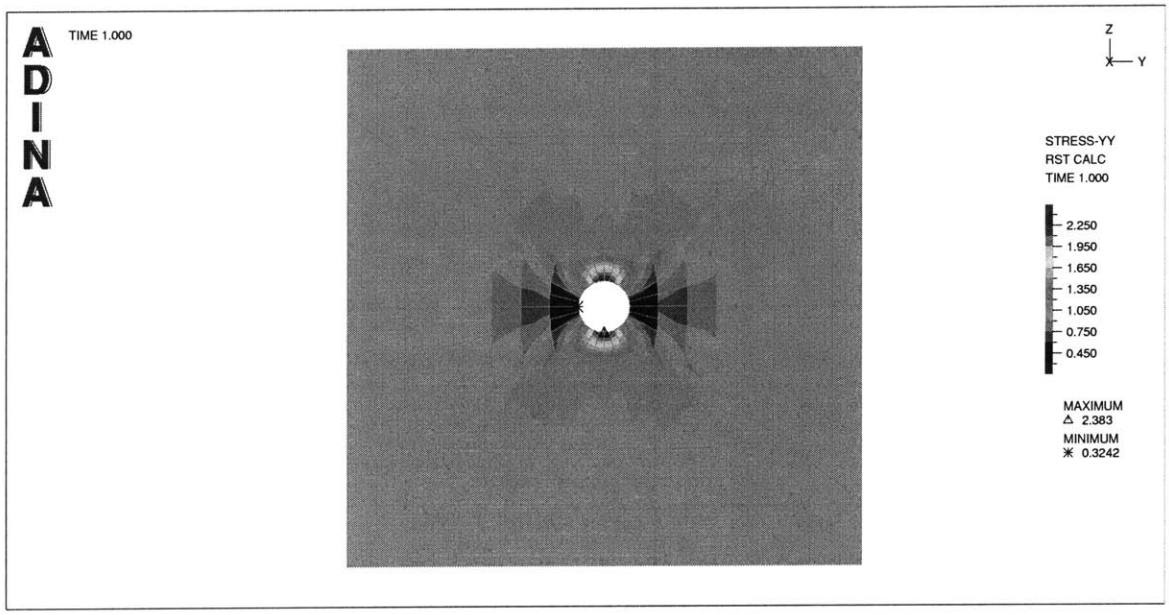

Figure 6-10: Stress (σ_{xx}) concentration at the vicinity of the hole. The plate has the geometry, boundary condition and loading condition in Figure 6-5. The Young's modulus is 100 and Poisson ratio is 0.3 under the plane stress condition. 256 elements (4-nodes) are used.

No. of elements	FEM (4-nodes)	FEM (9-nodes)	Enriching scheme	Error $\left[\frac{\sigma-\sigma_{exact}}{\sigma_{exact}}\right]$ (%)
16	1.455	1.937	2.464	18.1
64	1.878	2.388	2.649	11.9
256	2.383	2.785	2.957	1.7

Table 6.2: Comparison of maximum stress value (σ_{xx}) in the plate with a hole shown in Figure 6-5. The exact value is assumed as 3.008.

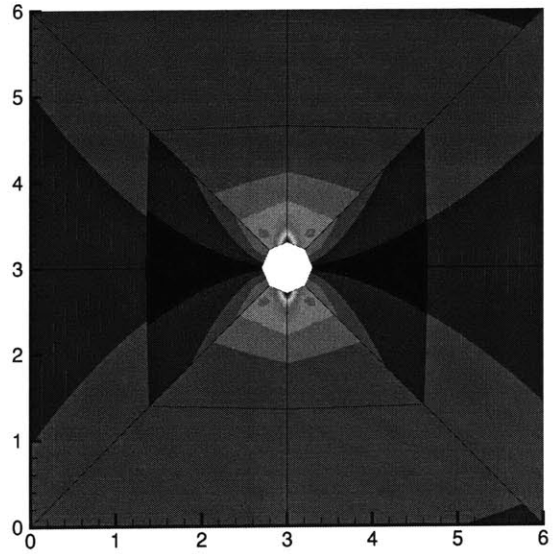

Figure 6-11: Stress (σ_{xx}) concentration at the vicinity of the hole. The plate has the geometry, boundary condition and loading condition in Figure 6-5. The Young's modulus is 100 and Poisson ratio is 0.3 under the plane stress condition. 16 elements (4−nodes) are used and the radius of each sphere added on the finite elements is 0.4.

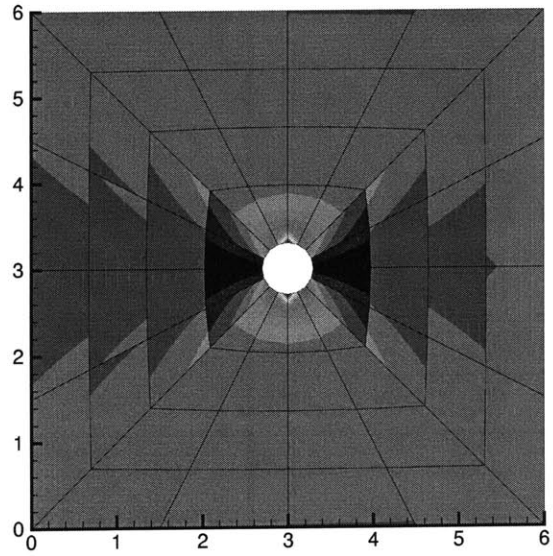

Figure 6-12: Stress (σ_{xx}) concentration at the vicinity of the hole. The Young's modulus is 100 and Poisson ratio is 0.3 under the plane stress condition. 64 elements (4−nodes) are used and the radius of each sphere added on the finite elements is 0.2.

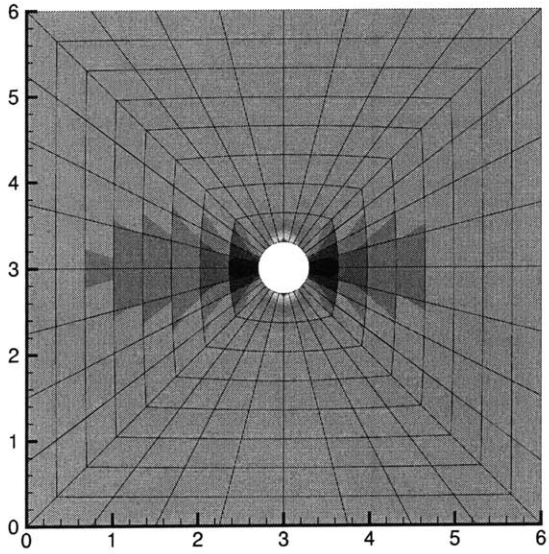

Figure 6-13: Stress (σ_{xx}) concentration at the vicinity of the hole. The Young's modulus is 100 and Poisson ratio is 0.3 under the plane stress condition. 256 elements (4−nodes) are used and the radius of each sphere added on the finite elements is 0.1.

6.2.2 Plate with a crack

In various applications, such as crack propagation, stress concentration, and etc, we have local concerning subregion for the analysis. We consider the plate which has a sharp crack in the middle as shown in Figure 6-14-(a). The plate has fixed boundary at the left ends, and unit lateral pressure loading is applied to the right at the right side. In the example, a sphere was located at the tip of the crack. The linear elastic solution for the stress field around a crack shows that the stress component are always of the same form in terms of the polar coordinates (r, θ) from the tip.

Near the crack tip, if the point is sufficiently close to the tip, i.e. $r \ll$ (crack length) , displacement fields are [34]

$$u(\mathbf{x}) = \frac{k_1}{2G}\sqrt{\frac{r}{2\pi}}\sin\frac{\theta}{2}\left[\mathcal{K}+1-2\cos^2\left(\frac{\theta}{2}\right)\right], \tag{6.5}$$

$$v(\mathbf{x}) = \frac{k_1}{2G}\sqrt{\frac{r}{2\pi}}\cos\frac{\theta}{2}\left[\mathcal{K}-1+2\cos^2\left(\frac{\theta}{2}\right)\right], \tag{6.6}$$

where r is the distance from the crack tip, k_1 is the stress intensity factor which is a measure of the magnitude of the stress occurring in the highly stressed region at the tip of a crack in an elastic solid, θ is the angle as shown in Figure 6-14-(b), G is shear modulus, and $\mathcal{K}$ is the Kolosov constant defined as

$$\mathcal{K} = \begin{cases} 3-4\nu & \text{plane strain,} \\ (3-\nu)/(1+\nu) & \text{plane stress.} \end{cases} \tag{6.7}$$

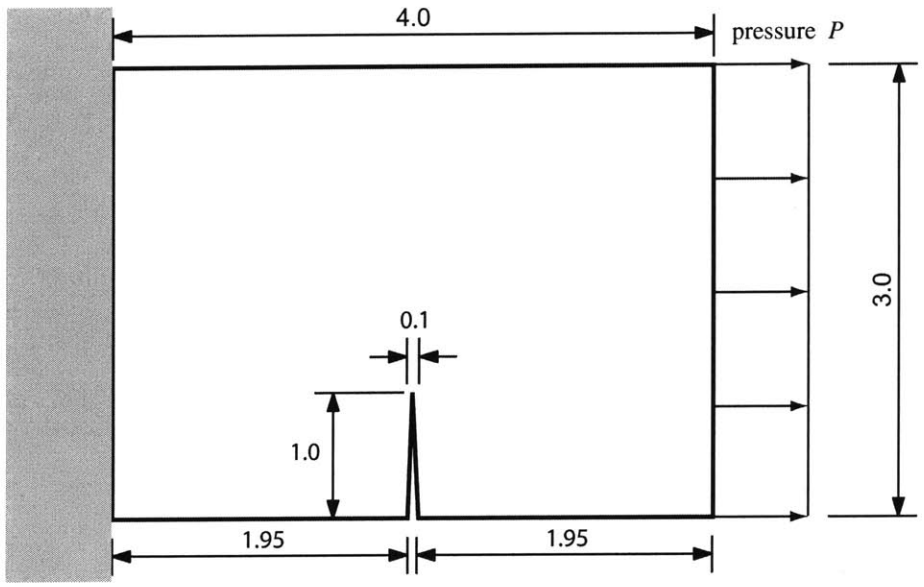

(a)

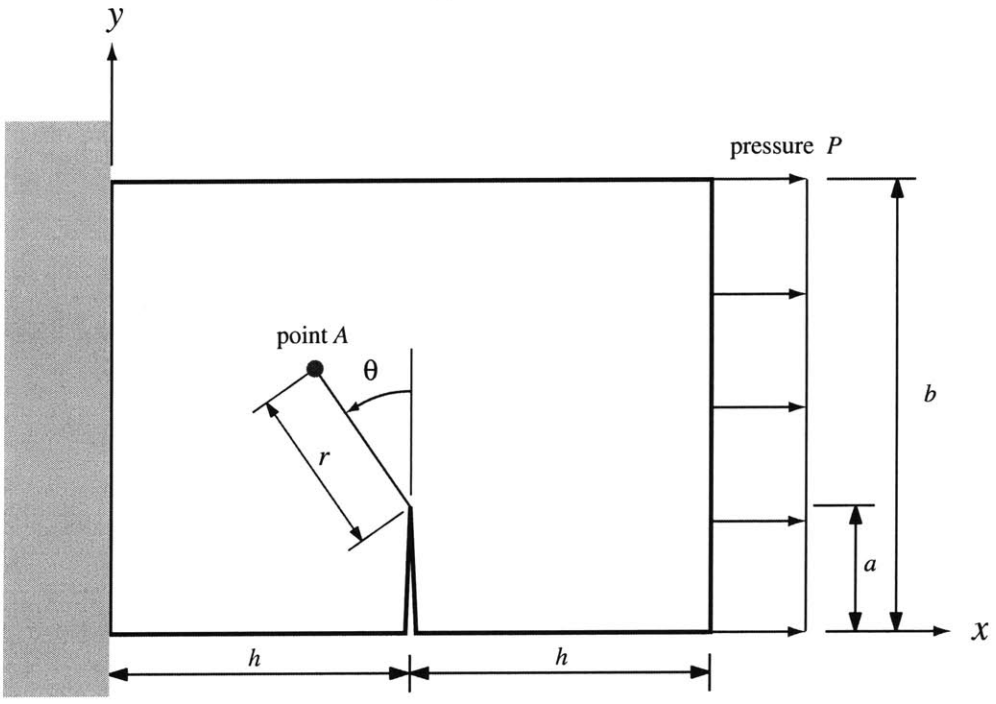

(b)

Figure 6-14: (a) geometry of a plate which has a sharp crack in the middle. The Young's modulus is 100 and the poisson ratio is 0.3. The plate is under the plane strain condition. (b) local coordinate system.

The stress fields are approximated by the equations

$$\sigma_{xx}(\mathbf{x}) = \frac{k_1}{\sqrt{2\pi r}} \cos\left(\frac{\theta}{2}\right)\left[1 + \sin\left(\frac{\theta}{2}\right)\sin\left(\frac{3\theta}{2}\right)\right], \tag{6.8}$$

$$\sigma_{yy}(\mathbf{x}) = \frac{k_1}{\sqrt{2\pi r}} \cos\left(\frac{\theta}{2}\right)\left[1 - \sin\left(\frac{\theta}{2}\right)\sin\left(\frac{3\theta}{2}\right)\right]. \tag{6.9}$$

where stress intensity factor k_1 is a function of the loading on the cracked configuration and of the size and shape of the crack and other geometrical boundaries. It has the dimensions of $(\text{stress} \times \sqrt{\text{length}})$. The factor k_0 is the normalizing parameter which has the dimensions of a stress intensity factor.

$$k_0 = \sigma\sqrt{\pi a} \tag{6.10}$$

where a is the length of crack, σ is the external pressure load. Since we have $a/b = 1/3 = 0.333$, $h/b = 2/3 = 0.666$, the equations by Brown and Srawley [35] is used as

$$\frac{k_1}{k_0} = 1.12 - 0.23\left(\frac{a}{b}\right) + 10.6\left(\frac{a}{b}\right)^2 - 21.7\left(\frac{a}{b}\right)^3 + 30.4\left(\frac{a}{b}\right)^4 \tag{6.11}$$

Substituting $a/b = 0.333$, we have stress value 4.004 at 0.1 from the crack tip.

The elastic solution predicts infinite stresses at the crack tip ($r = 0$) which cannot occur in practice since there is plastic flow in the highly stressed region near the tip. However, if the region of plastic flow is small, it may be assumed that the behavior of the crack is determined by the elastic stress intensity factor.

With the refinement the concentration is depicted in the elements around the crack tip. However, the shape is still blunt and it means we need to refine the element near the crack tip tremendously to have reasonable shape. The comparison of the maximum σ_{xx} is listed

No. of elements	FEM (4-nodes)	Enriching scheme
16	2.330	3.390
64	3.518	5.188
256	5.203	7.710

Table 6.3: Comparison of maximum value of stress σ_{xx} on the crack tip.

in Table. 6.3.

By the enriching coupling scheme, we can depict the concentration of strain more precisely with reasonable shape. The stress distribution along vertical direction from the crack tip is as shown in Figure 6-15. When finer mesh is used and spheres are superposed, the peak stress value is close to the exact analytical value.

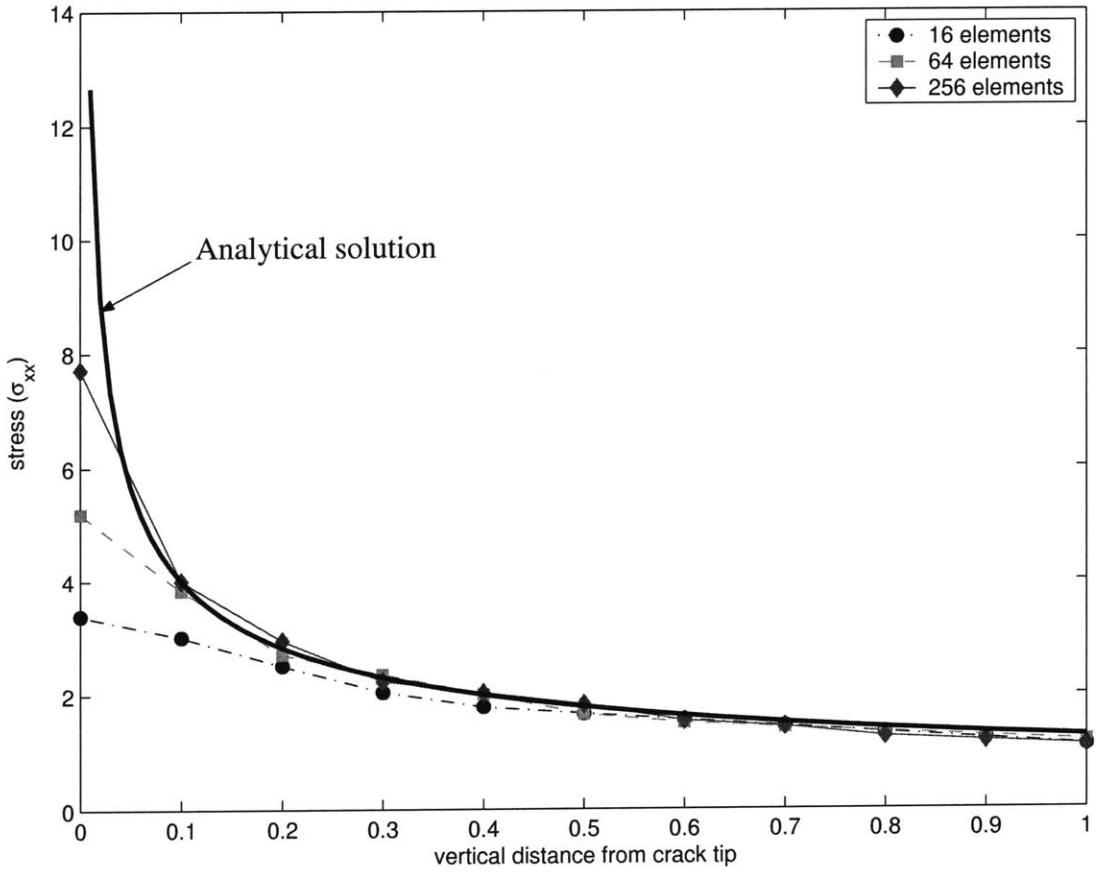

Figure 6-15: Enriching scheme: Stress (σ_{xx}) distribution along the vertical direction from the crack tip.

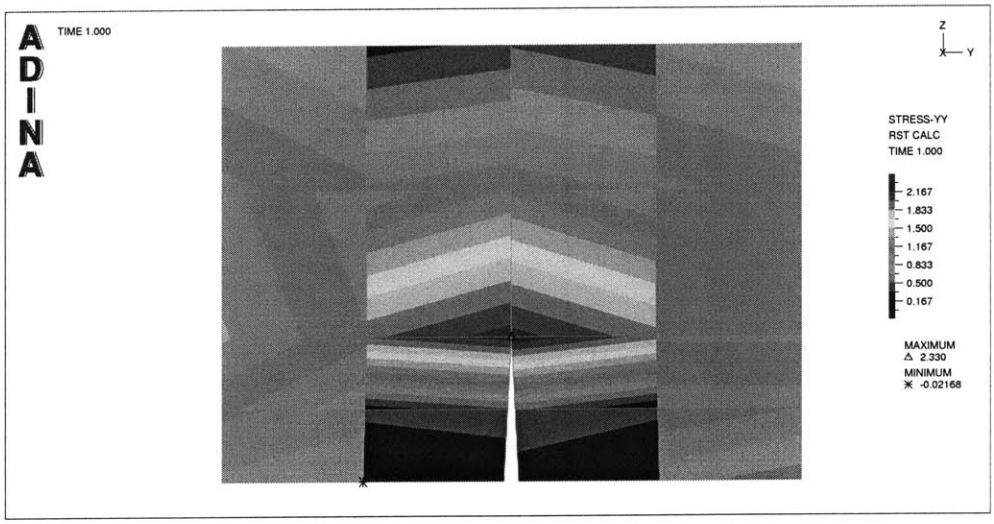

Figure 6-16: Stress (σ_{xx}) concentration at the crack tip. The plate has the geometry, boundary condition and loading condition in Figure 6-14. The Young's modulus is 100 and Poisson ratio is 0.3 under the plane strain condition. 16 elements (4-nodes) are used.

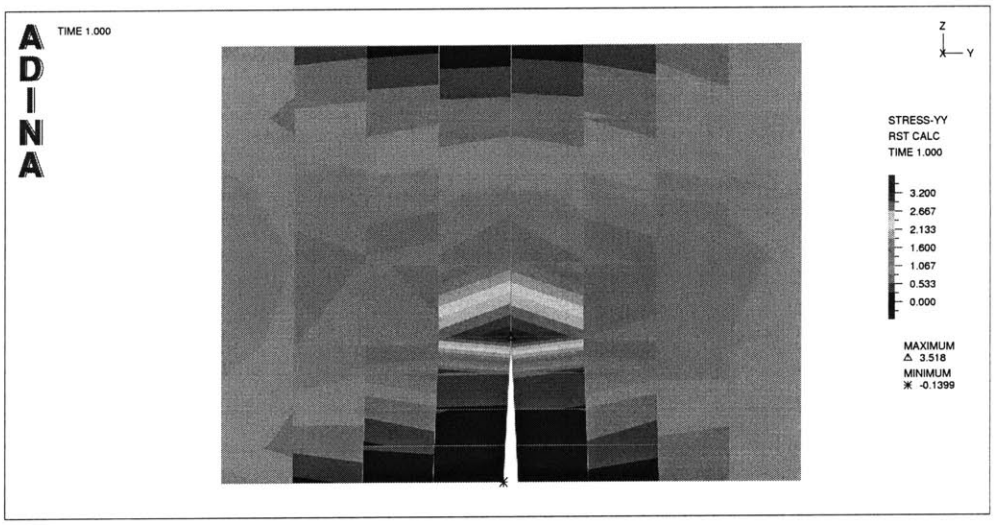

Figure 6-17: Stress (σ_{xx}) concentration at the crack tip. The plate has the geometry, boundary condition and loading condition in Figure 6-14. The Young's modulus is 100 and Poisson ratio is 0.3 under the plane strain condition. 64 elements (4-nodes) are used.

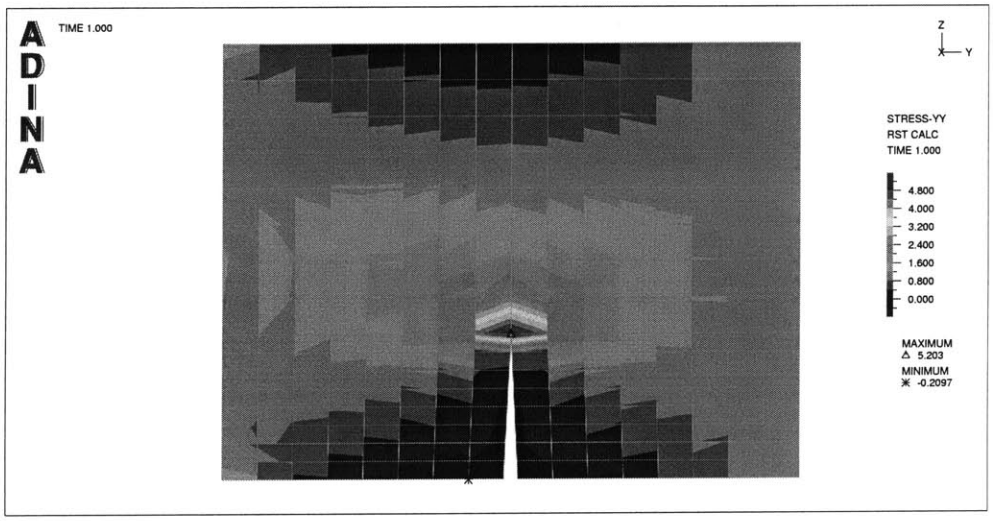

Figure 6-18: Stress (σ_{xx}) concentration at the crack tip. The plate has the geometry, boundary condition and loading condition in Figure 6-14. The Young's modulus is 100 and Poisson ratio is 0.3 under the plane strain condition. 256 elements (4-nodes) are used.

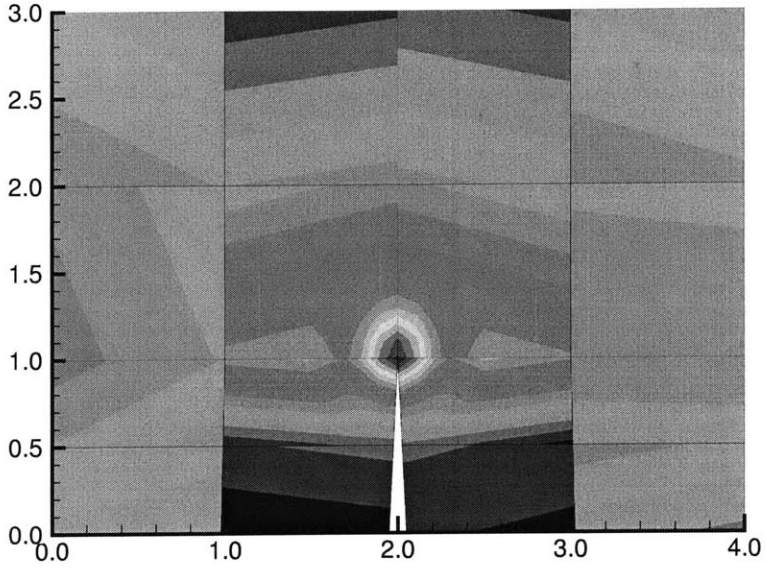

Figure 6-19: Enriching scheme: Stress (σ_{xx}) concentration at the crack tip. The plate has the geometry, boundary condition and loading condition in Figure 6-14. The Young's modulus is 100 and Poisson ratio is 0.3 under the plane strain condition. 16 elements (4-nodes) are used and the radius of each sphere added on the finite elements is 0.5.

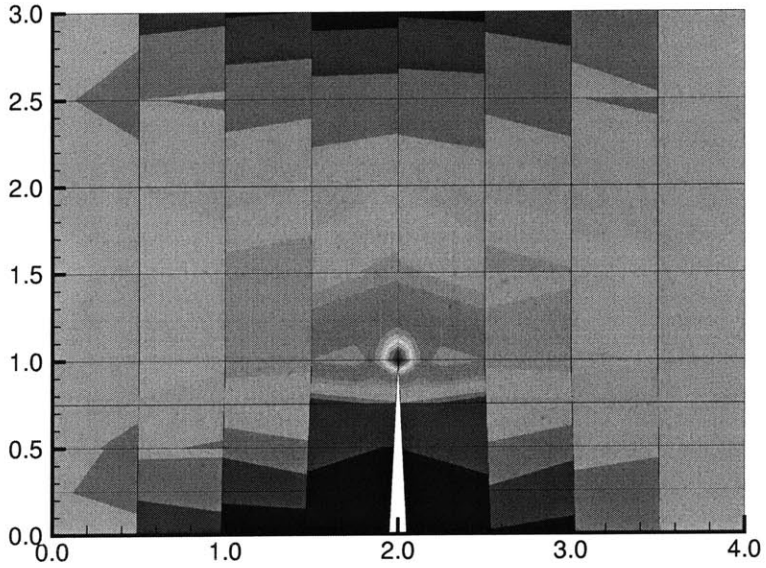

Figure 6-20: Enriching scheme: Stress (σ_{xx}) concentration at the crack tip. The plate has the geometry, boundary condition and loading condition in Figure 6-14. The Young's modulus is 100 and Poisson ratio is 0.3 under the plane strain condition. 64 elements (4-nodes) are used and the radius of each sphere added on the finite elements is 0.25.

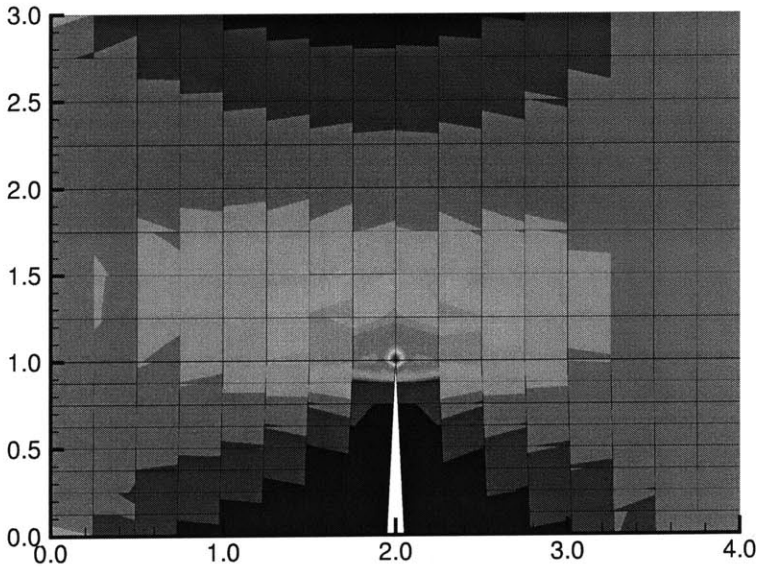

Figure 6-21: Enriching scheme: Stress (σ_{xx}) concentration at the crack tip. The plate has the geometry, boundary condition and loading condition in Figure 6-14. The Young's modulus is 100 and Poisson ratio is 0.3 under the plane strain condition. 256 elements (4-nodes) are used and the radius of each sphere added on the finite elements is 0.125.

Chapter 7

Conclusions and Remarks

The main goal of this thesis was to improve a computational scheme, namely the method of finite spheres, and develop a coupling scheme and enriching scheme which enable to use finite elements and finite spheres simultaneously. In the method of finite spheres, the domain is discretized with spheres which have nodes and radii without a mesh. The approximation functions are compactly supported and this results into banded stiffness matrices. The fact that no mesh is used may reduce numerical calculation cost and time in analyzing a variety of problems which require re-meshing at each step.

In this thesis, we concentrate on the improvement of efficiency of the method of finite spheres. The method of finite spheres eliminates mesh generation, but a more complicated numerical integration is needed in each sphere domain. Computational efficiency was pursued by the appropriate choice of effective approximation functions, incorporation of boundary conditions and numerical integration schemes [18]. However, to compete with the traditional finite element methods, the method of finite spheres should still be equipped with more efficient numerical integration schemes.

For this numerical integration issue, our approach has two aspects. One is the transformation of the original integral equations into more efficient expressions. Since we consider two-dimensional problems, we need to evaluate surface integrations for each spheres. Using the compact supportness and applying the divergence theorem, it is possible to reduce the dimensions of the integrations for most terms. This improvement significantly eliminates unnecessary numerical cost and numerical error. For the numerical scheme, we propose an adaptive composite rule. Considering the local basis and the characteristic of the approximation functions, an optimization of integration is achieved.

For the more general application of the method of finite spheres, we developed an auto-sphere generation scheme. Our program can directly import the data file of the commercial FEM package (ADINA) without any modification and our scheme detects the boundary of the domain. We classify the kinds of finite spheres into inner spheres, contact spheres and boundary spheres, and our scheme generates spheres to cover the entire analysis domain.

We propose a new coupling scheme which enables to use the traditional finite element and finite spheres at the same time on the domain. Our scheme is different from other existing schemes; and our scheme satisfies the partition of unity. A tension and bending test is implemented and the convergence of strain energy is verified.

We also propose an enriching scheme by finite spheres on finite element discretizations. For practical purpose, we use $4-$node finite elements and add spheres. The enriching scheme is effective to simulate local behavior and is very adaptable since we can add or remove spheres on any local domain. We used the enriching scheme to solve stress concentration problems, namely a plate with a hole and plate with a crack. The results show that the enriching scheme can be effective to analyze stress concentration phenomena.

In this work, we worked on the solution of linear elasticity and static problems. Still the numerical integration in the method of finite spheres is expensive when compared with the traditional finite element method. However, further improvement in efficiency should be possible and our meshless and coupling schemes have great potential to become effective numerical solution techniques for many problems in mechanics.

The method of finite spheres, coupling scheme, and enriching scheme can be extended to three-dimensional analysis. Our efficient integral transformation then reduces the volume integration into surface integration and the concept of auto-sphere generation is also applicable to three-dimensional domains.

Appendix A

Fundamentals of Functional Analysis

In this appendix we summarize some essential concepts of spaces, norms and functionals. These terminologies and definitions are widely used for various areas in numerical methods [36, 37].

A.1 Vector spaces

Let X be a general vector space [37]. We have the essential property of a vector space that any linear combination of elements of the space belongs to the same space.

Definition A.1.1 (Vector space) *A norm on X is a function*

$$v \in X \rightarrow ||v|| \in \mathbb{R}^{+} \tag{A.1}$$

such that

$$||v|| = 0 \Rightarrow v = 0, \tag{A.2}$$

$$||\lambda v|| = |\lambda|||v||, \forall \lambda \in \mathbb{R}, \tag{A.3}$$

$$||v + w|| \leq ||v|| + ||w|| \quad \forall (v, w) \in X \times X. \tag{A.4}$$

where $\mathbb{R}^+$ is a set of positive real numbers.

A.2 Hilbert space

Hilbert space is normed linear spaces, where word *normed* means that the space is equipped with a certain norm. We can start with the definition of *inner product* [37].

Definition A.2.1 (Inner product) *Let X be a complex linear space. An* inner product *on X is a mapping that associates to each ordered pair of vectors, x, y a scalar denoted (x, y) that satisfies the following:*

$$(x + y, z) = (x, z) + (y, z) \qquad \textit{Additivity} \tag{A.5}$$

$$(\alpha x, y) = \alpha(x, y) \qquad \textit{Homogeneity} \tag{A.6}$$

$$(x, y) = \overline{(y, x)} \qquad \textit{Symmetry} \tag{A.7}$$

$$(x, x) > 0, \ \textit{when } x \neq 0 \qquad \textit{Positive Definiteness} \tag{A.8}$$

where bar denotes the complex conjugate.

Definition A.2.2 (Inner product space) *An inner product space is defined to be a linear*

space equipped with an inner product defined on the linear space X. for example, we can define the norm on X,

$$||x|| = (x, x)_X^{1/2}, \tag{A.9}$$

By using the definition we can infer the Schwarz inequality as $|(x, y)| \leq ||x||\ ||y||$, where $||\cdot||$ is defined in Equation (A.9). A Hilbert space is a linear space X with which we associate an inner product $(\cdot, \cdot)_X$ and this is a symmetric positive definite bilinear form, which induces a norm, $||w||_X = (w, w)^{1/2}$. A Hilbert space is a *complete inner product space*, and also a special case of a Banach space Z, which is a normed linear space. The completeness means that any Cauchy sequence converges to a member of X. Although the Banach norm is not necessarily associated with a bilinear form, it must satisfy the conditions of norms.

We may express the spaces $H^1(\Omega)$ to $H^m(\Omega)$ for any non-negative integer m. For example, in $1-D$ case, say $\Omega = (0, 1)$, we have

$$H^m(\Omega) = \left\{ v | \int_0^1 v^2 dx < \infty, \int_0^1 v_x^2 dx < \infty, \int_0^1 \left(\frac{d^m v}{dx^m} \right) dx < \infty \right\} \tag{A.10}$$

which is equipped with inner product

$$(w, v)_{H^m(\Omega)} = \sum_{j=0}^{m} \int_0^1 \frac{d^j w}{dx^j} \frac{d^j v}{dx^j} dx. \tag{A.11}$$

The Hilbert norm is

$$||w||_{H^m(\Omega)} = \left[\sum_{j=0}^{m} \int_0^1 \left(\frac{d^j w}{dx^j} \right)^2 dx \right]^{1/2} \tag{A.12}$$

A.3 Lebesgue spaces, $L^p(\Omega)$

The Lebesgue spaces play a important role in the functional analysis. Lebesgue spaces, $L^p(\Omega), p > 1$ are not Hilbert spaces except in the special case $p = 2$. When $p = 2$, $L^2(\Omega) \equiv H^0(\Omega)$. The inner product is

$$(w, v)_{L^2(\Omega)} = \int_\Omega wv d\Omega. \tag{A.13}$$

and the norm is defined by

$$||v||_{L^2(\Omega)} = \left(\int_\Omega v^2 d\Omega \right)^{1/2} \tag{A.14}$$

The generalized form of the Lebesgue space L^p is

$$L^p(\Omega) = \left\{ v | \int_\Omega |v|^p d\Omega < \infty \right\} \tag{A.15}$$

The norm is

$$||v||_{L^p(\Omega)} = \left(\int_\Omega |v|^p d\Omega \right)^{1/p} \tag{A.16}$$

As $p \to \infty$, the norm picks up the largest value of v, so the relation can be rewritten as

$$||v||_{L^\infty(\Omega)} = \sup_{x \in \Omega} |v|. \tag{A.17}$$

Theorem A.3.1 *Let $\{f_n\}$ be a sequence in $L_p(\Omega)$, $1 \leq p < \infty$ with the property that*

$$\lim_{m,n \to \infty} \int_\Omega |f_m - f_n|^p dt = 0. \tag{A.18}$$

Then there is a subsequence $\{f_{n_k}\}$ *and an* $f \in L_p(\Omega)$ *that satisfies* $f = \lim f_{n_k}$ *and*

$$\lim_{k\to\infty} \int_\Omega |f - f_{n_k}|^p d\Omega = 0 \tag{A.19}$$

A.4 Sobolev spaces

For the simple case of $\Omega = (0,1) \in \mathbb{R}$, the Sobolev space is defined as

$$W^{m,p}(\Omega) = \left\{ v | \frac{d^j v}{dx^j} \in L^p(\Omega), \quad j = 0, 1, \ldots, m \right\}, \tag{A.20}$$

and the norm is

$$||w||_{W^{m,p}(\Omega)} = \left(\sum_{j=0}^{m} \int_0^1 |\frac{d^j w}{dx^j}|^p dx \right)^{1/p} \tag{A.21}$$

It should be noted that $W^{m,2}(\Omega) = H^m(\Omega)$, and $W^{0,p}(\Omega) = L^p(\Omega)$.

A.5 $C^m(\Omega)$ spaces

For the simple case of $\Omega = (0,1) \in \mathbb{R}$,

$$C^m(\Omega) = \left\{ v | v, \frac{dv}{dx}, \ldots, \frac{d^m v}{dx^m} = \text{continuous in the domain } \Omega \right\} \tag{A.22}$$

where m can be any integer. For example, $C^1(\Omega)$ has continuous derivatives, but the second derivatives are not continuous any more. Therefore, $C^m(\Omega)$ denotes the collection of all functions defined on Ω with the property that all partial derivatives up to order m are continuous. Also $C^\infty(\Omega) = \bigcap_{n=1}^{\infty} C^n(\Omega)$.

Definition A.5.1 (Riesz Representation Theorem) *Let H be a Hilbert space and let l be a bounded linear functional on H. Then there is one and only one vector $y \in H$ such that*

$$l(x) = (x, y), \quad \textit{for all } x \in H \tag{A.23}$$

The vector y is called the representation of l.

Definition A.5.2 (Sesquilinear functional) *A mapping $q(x, y) : X \times X \to C$ is said to be sesquilinear functional if*

$$q(x_1 + x_2, y) = q(x_1, y) + q(x_2, y) \tag{A.24}$$

$$q(\alpha x, y) = \alpha q(x, y) \tag{A.25}$$

$$q(x, y_1 + y_2) = q(x, y_1) + q(x, y_2) \tag{A.26}$$

$$q(x, \alpha y) = \bar{q}(x, y) \tag{A.27}$$

Definition A.5.3 (Lax-Milgram Theorem) *Let $B[u, v]$ be a sesquiliner functional on a Hilbert space H and assume that there are positive constants a and b such that*

$$B[u, v] \leq a||u|| \cdot ||v|| \tag{A.28}$$

$$b||u||^2 \leq |B[u, v]| \tag{A.29}$$

for all u,v in H. Let l be any bounded linear functional on H. Then there exist unique points u_0 and v_0 in H such that

$$l(x) = B[x, v_0] = \overline{B[u_0, x]} \tag{A.30}$$

A.6 Dual spaces

A linear form is a continuous linear real-valued function defined on X. We recall that a linear real-valued function l is continuous if and only if there exists C such that

$$|l(v)| \leq C||v||, \quad \forall v \in X \tag{A.31}$$

Continuity is a direct consequence of Equation (A.31) since, due to the linearity, it implies

$$|l(v) - l(w)| \leq C||v - w||, \quad \forall (v, w) \in X \times X. \tag{A.32}$$

The space of all linear forms on X is a vector space, called the *dual space* [37] of X and denoted by X'. It is equipped with the norm

$$||l||_{X'} = \sup_{v \in X, v \neq 0} \frac{l(v)}{||v||} \tag{A.33}$$

This definition implies

$$|l(v)| \leq ||l||_{X'}||v||, \quad \forall v \in X, \tag{A.34}$$

and that $||l||_{X'}$ is indeed the smallest constant C such that the Equation (A.31) holds.

Appendix B

Cubature rules

B.1 Midpoint rule

By subdividing the disk with concentric circles and radial lines, we have integration subdomain as shown in Figure B-1. The centroid of each annular segment can be obtained as

$$
\begin{aligned}
r_{cg} &= \frac{\int_{-\theta/2}^{\theta/2}\int_{r_1}^{r_2} r^2 dr d\theta}{\int_{-\theta/2}^{\theta/2}\int_{r_1}^{r_2} r dr d\theta} \\
&= \frac{1/3(r_2^3 - r_1^3)}{1/2(r_2^2 - r_1^2)} \\
&= \frac{2}{3}\frac{(r_2^2 + r_2 r_1 + r_1^2)}{(r_2 + r_1)} \\
&= \frac{2}{3}\frac{(j^2\Delta r^2 + j(j-1)\Delta r^2 + (j-1)^2\Delta r^2)}{(j\Delta r - \Delta r + j\Delta r)} \\
&= \frac{j^2 - j + 1/3}{j - 1/2}\Delta r
\end{aligned}
\tag{B.1}
$$

$$
\theta_i = (i - 1/2)\Delta\theta \tag{B.2}
$$

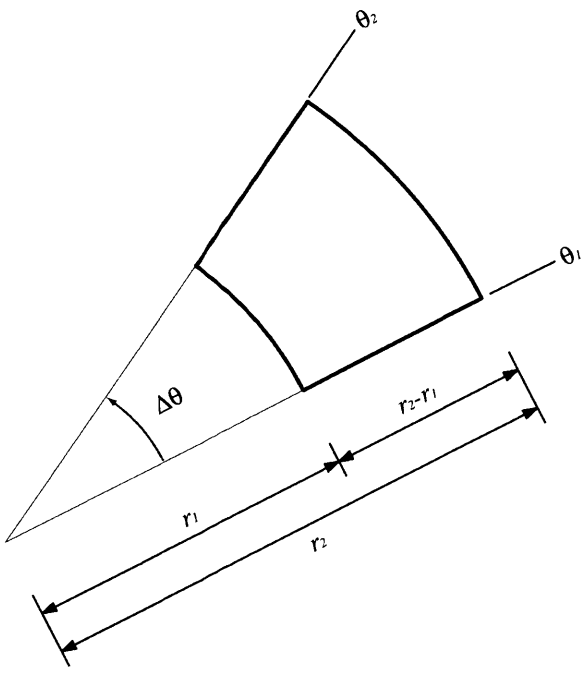

Figure B-1: Midpoint rule integration.

where $r_1 = (j-1)\Delta r$, $r_2 = (j\Delta r)$, $j = 1, 2, \ldots, n$, $\Delta r = R_I/n_r$, and $\Delta\theta = \frac{2\pi}{n_\theta}$.

The weighting coefficient corresponding to a segment is calculated as

$$\begin{aligned} D_{ij} &= \frac{1}{2}\left(r_1^2 - r_0^2\right)\Delta\theta \\ &= \frac{1}{2}\left[j^2\Delta r^2 - (j-1)^2\Delta r^2\right]\Delta\theta \\ &= \frac{1}{2}\left(2j-1\right)\Delta\theta\Delta r^2 \\ &= \left(j - \frac{1}{2}\right)\Delta\theta\Delta r^2 \end{aligned} \tag{B.3}$$

B.2 Gauss integration on a segment

Gauss integration can be applied by transforming the original coordinate system (r, θ) to natural coordinate system (s, t) via isoparametric formulation as illustrated in Figure B-2.

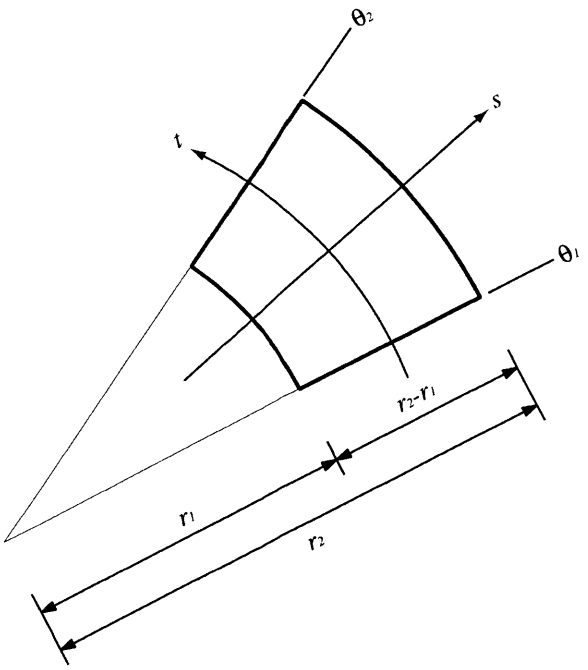

Figure B-2: Gauss integration on a segment.

The center of local (s,t) coordinate system can be expressed as

$$r_m = \frac{1}{2}(r_1 + r_2) \tag{B.4}$$

$$\theta_m = \frac{1}{2}(\theta_1 + \theta_2). \tag{B.5}$$

The isoparametric variables are

$$s = \frac{2\,(r - r_m)}{r_2 - r_1} = \frac{\left(r - \dfrac{r_1 + r_2}{2}\right)}{r_2 - r_1}, \tag{B.6}$$

$$t = \frac{2\,(\theta - \theta_m)}{\theta_2 - \theta_1} = \frac{\left(\theta - \dfrac{\theta_1 + \theta_2}{2}\right)}{\theta_2 - \theta_1}. \tag{B.7}$$

The Jacobian matrix becomes

$$|J| = \begin{vmatrix} \frac{\partial r}{\partial s} & \frac{\partial \theta}{\partial s} \\ \frac{\partial r}{\partial t} & \frac{\partial \theta}{\partial t} \end{vmatrix} = \begin{vmatrix} \frac{r_2 - r_1}{2} & 0 \\ 0 & \frac{\theta_2 - \theta_1}{2} \end{vmatrix} = \frac{1}{4}(r_2 - r_1)(\theta_2 - \theta_1). \tag{B.8}$$

The original equation is transformed into isoparametric form as

$$\begin{aligned} &\int_{\theta_1}^{\theta_2} \int_{r_1}^{r_2} \mathbf{B}(r,\theta)\mathbf{CB}(r,\theta) dr d\theta \\ &\qquad = \int_{-1}^{+1} \int_{-1}^{+1} \mathbf{B}(s,t)\mathbf{CB}(s,t) \frac{1}{4}(r_2 - r_1)(\theta_2 - \theta_1)\, ds dt. \end{aligned} \tag{B.9}$$

Therefore, the numerical integration is

$$\begin{aligned} &\int_{\theta_1}^{\theta_2} \int_{r_1}^{r_2} \mathbf{B}(r,\theta)\mathbf{CB}(r,\theta) dr d\theta \\ &\qquad = \sum_{i}^{N_R} \sum_{j}^{N_\theta} c_{ij} \mathbf{B}(s_i,t_j)\mathbf{CB}(s_i,t_j) \frac{1}{4}(r_2 - r_1)(\theta_2 - \theta_1). \end{aligned} \tag{B.10}$$

Bibliography

[1] R. W. Hamming. *Numerical methods for scientists and engineers*. Dover Publications, Inc., 31 East 2nd Street, Mineola, N.Y. 11501, 1973.

[2] K. J. Bathe. *Finite Element Procedures*. Prentice Hall, Upper Saddle River, New Jersey 07458, 1996.

[3] J. J. Monaghan. An introduction to SPH. *Computer Physics Communications*, 48:89–96, 1988.

[4] B. Nayroles, G. Touzot, and P. Villon. Generalizing the FEM: diffuse approximation and diffuse elements. *Computational Mechanics*, 10:307–318, 1992.

[5] T. Belytschko, Y.Y. Lu, and L. Gu. Element free Galerkin methods. *International Journal for Numerical Methods in Engineering*, 37:229–256, 1994.

[6] W. K. Liu. Reproducing kernel particle methods for elastic and plastic problems. In B. J. Benson and R. A. Asaro, editors, *Advanced Computational Methods for Material Modeling*, volume 180 of *AMD*, pages 175–190. ASME, 1993.

[7] J. M. Melenk and I. Babuška. The partition of unity finite element method: basic theory and applications. *Computer Methods in Applied Mechanics and Engineering*, 139:289–314, 1996.

[8] C. A. Duart and J. T. Oden. H-p clouds - an -h-p meshless method. *Numerical Methods for Partial Differential Equations*, 12:673–705, 1996.

[9] C. A. Duart and J. T. Oden. An h-p adaptive method using clouds. *Computer Methods in Applied Mechanics and Engineering*, 139:237–262, 1996.

[10] T. Zhu, J. D. Zhang, and S. N. Atluri. A local boundary integral equation (LBIE) method in computational mechanics and a meshless discretization approach. *Computational Mechanics*, 21:223–235, 1998.

[11] S. N. Atluri and T. Zhu. A new meshless local petrov-galerkin (MLPG) approach in computational mechanics. *Computational Mechanics*, 22:117–127, 1998.

[12] M. Griebel and M. A. Schweitzer. A particle-partition of unity method for the solution of elliptic, parabolic, and hyperbolic pdes. *SIAM Journal on Scientific Computing*, 22(3):853–890, 2000.

[13] S. De and K. J. Bathe. The method of finite spheres. *Computational Mechanics*, 25:329–345, 2000.

[14] E. Oñate, S. Idelsohn, O. C. Zienkiewicz, and R. L. Taylor. A finite point method in computational mechanics. applications to convective transport and fluid flow. *International Journal for Numerical Methods in Engineering*, 39:3839–3866, 1996.

[15] G. R. Liu. *Mesh free methods: moving beyond the finite element method.* CRC Press LLC, 2000 N.W. Corporate Blvd., BocaRaton, Florida 33431, 2003.

[16] K. Yosida. *Functional analysis.* Springer, Berlin Heidelberg, 1995.

[17] P. Duchateau and D. W. Zachmann. *Partial Differential Equations.* McGraw-Hill, Inc., 1986.

[18] S. De and K. J. Bathe. The method of finite spheres with improved numerical integration. *Computers and Structures*, 79:2183–2196, 2001.

[19] F. B. Hildebrand. *Introduction to numerical analysis.* Dover Publications, Inc, 31 East 2nd Street, Mineola, N.Y. 11501, 1987.

[20] E. Isaacson and H. B. Keller. *Analysis of numerical methods.* Wiley, New York, 1966.

[21] P. J. Davis and P. Rabinowitz. *Methods of numerical integration.* Academic Press, New York, 1984.

[22] G. A. Evans. *Practical numerical integration.* Wiley, Chichester, 1993.

[23] A. H. Stroud. *Approximate calculation of multiple integrals.* Prentice Hall, Upper Saddle River, New Jersey 07458, 1971.

[24] A. Krommer and C. Ueberhuber. *Computational Integration.* SIAM, Society for Industrial and Applied Mathematics, 3600 University City Science Center, Philadelphia, PA 19104-2688, 1998.

[25] S. De, J. W. Hong, and K. J. Bathe. On the method of finite spheres in applications: Towards the use with ADINA and in a surgical simulator. *Computational Mechanics*, 31:27–37, 2003.

[26] S. De and K. J. Bathe. Towards an efficient meshless computational technique: the method of finite spheres. *Engineering Computations*, 18:170–192, 2001.

[27] G. R. Liu and Y. T. Gu. Coupling of elment free galerkin and hybrid boundary element methods using modified variational formulation. *Computational Mechanics*, 26:166–173, 2000.

[28] G. R. Liu and Y. T. Gu. Meshless local petrov-galerkin (MLPG) method in combination with finite element and boundary element approaches. *Computational Mechanics*, 26:536–546, 2000.

[29] H. Karutz, R. Chudoba, and W. B. Krätzig. Automatic adaptive generation of a coupled finite element/element-free galerkin discretization. *Finite Elements in Analysis and Design*, 38:1075–1091, 2002.

[30] J. W. Hong and K. J. Bathe. On analytical transformations for efficiency improvements in the method of finite spheres. In K. J. Bathe, editor, *Computational fluid and solid mechanics*, volume 1, pages 1990–1994. M. I. T. Conference, Elsevier, June 2003.

[31] I. Babuška and J. M. Melenk. The partition of unity finite element method. *International Journal for Numerical Methods in Engineering*, 40:727–758, 1997.

[32] S. Timoshenko. *Strength of materials.* Van Nostrand Reinhold Company, 450 West 33rd Street, New York, N. Y. 10001, 1958.

[33] W. D. Pilkey. *Peterson's stress concentration factors.* John Wiley & Sons, Inc., 605 Third Avenue, New York, N. Y. 10158-0012, 1997.

[34] T. L. Anderson. *Fracture mechanics: Fundamentals and applications.* CRC Press, Boca Raton, FL, 1991.

[35] D. P. Rooke and D. J. Cartwright. *Compendium of stress intensity factors.* Her Majesty's Stationary Office, London, 1976.

[36] Arch W. Naylor and George R. Sell. *Linear operator theory in engineering and science.* Springer-Verlag, 31 East 2nd Street, Mineola, N.Y. 11501, 1982.

[37] D. Chapelle and K. J. Bathe. *The finite element analysis of shells - fundamentals.* Springer, Germany, 2003.